Open Access Dissertations

Theses and Dissertations

Fall 2014

Investigation of optical near field using near field scanning optical microscopy

Yan Li
Purdue University

PURDUE UNIVERSITY
GRADUATE SCHOOL
Thesis/Dissertation Acceptance

This is to certify that the thesis/dissertation prepared

By Yan Li

Entitled
INVESTIGATION OF OPTICAL NEAR FIELD USING NEAR FIELD SCANNING OPTICAL MICROSCOPY

For the degree of   Doctor of Philosophy

Is approved by the final examining committee:

Xianfan Xu

Vladimir Shalaev

Arvind Raman

Minghao Qi

To the best of my knowledge and as understood by the student in the Thesis/Dissertation Agreement, Publication Delay, and Certification/Disclaimer (Graduate School Form 32), this thesis/dissertation adheres to the provisions of Purdue University's "Policy on Integrity in Research" and the use of copyrighted material.

Xianfan Xu

Approved by Major Professor(s): _____

Approved by: Ganesh Subbarayan   10/15/2014

Head of the Department Graduate Program   Date

INVESTIGATION OF OPTICAL NEAR FIELD USING NEAR FIELD SCANNING

OPTICAL MICROSCOPY

A Dissertation

Submitted to the Faculty

of

Purdue University

by

Yan Li

In Partial Fulfillment of the

Requirements for the Degree

of

Doctor of Philosophy

December 2014

Purdue University

West Lafayette, Indiana

ACKNOWLEDGEMENTS

TABLE OF CONTENTS

LIST OF FIGURES

ABSTRACT

Li, Yan. Ph.D., Purdue University, December 2014. Investigation of Optical Near Field Using Near Field Scanning Optical Microscope. Major Professor: Xianfan Xu, School of Mechanical Engineering.

Conventional optical imaging techniques have a fundamental resolution limit due to the diffraction limit of light. The advances of science and technology on the nanoscale demand a new tool for characterization. The Near Field Scanning Optical Microscopy (NSOM) has been developed to tackle certain aspects of this problem. The work presented here applies different types of NSOM to explore the near field distribution of metal plasmonic nanostructures.

Ridge apertures with shapes like bowtie and C can be used to focus light into sub-diffraction limit spot with enhancement. This localization of the field near the exit of a bowtie aperture is investigated with a home built aperture NSOM. The experiment results confirm the confinement of focused light spot and the fast decay nature of optical near fields. To further increase the transmission efficiency, a concentric grating structure is added to the bowtie aperture. Near field examination of the transmitted energy with NSOM shows a factor of 15 augment in the transmission.

To achieve a better resolution, an alternative method is also investigated. The scattering (apertureless) NSOM is demonstrated to have optical resolution only limited by the radius of its tip apex. The physics behind scattering NSOM is explained and the difficulty

 of its implementation investigated. Among the different proposed methods, the pseudo-heterodyne interferometric method is chosen and applied in this work.

A scattering NSOM has been built based on a commercial AFM. With the home-built s-NSOM setup, the optical responses of several different plasmonic structures have been studied. The examination of a sample with a circular aperture array shows that the interferometric pseudo-heterodyne method is indeed effective in suppressing the background noise. The s-NSOM has also been used to investigate the formation mechanism of interferometric patterns observed during the measurement of a single nanoslit. In the end, a revisit of the 3-D optical field distribution of the bowtie aperture has been conducted, with a focus on the E_z field. For s-NSOM measurements, both the amplitude and phase information are obtained, enabling vector analysis of the optical fields.

CHAPTER 1. INTRODUCTION

As science and technology enter the micro realm, researchers have shown a keen interest in the fabrication and characterization of structures at the nanometer scale. Referring to the definition by the National Nanotechnology Initiative, these nanometer structures usually have a length scale of less than 100 nm in more than one dimension. When an object becomes this small in size, macroscopic rules lose their authority and new physical effects emerge. While many techniques have been developed to study these nanometer phenomena, the conventional optical techniques have their fundamental resolution limit due to the diffraction limit of light. In this context, near-field optics and Near-field Scanning Optical Microscopy (NSOM) have been developed.

1.1   The Diffraction Limit

Optical techniques of investigation objects at high magnification have been widely employed in science and technology over the years. They have some distinguished advantages like easy to operate, noninvasive measurement, etc. As technology advances to the Nano era, it demands a novel characterization mechanism with higher spatial resolution. The conventional optical techniques have a spatial resolution of approximately half of the wavelength of light source, which is known as the diffraction limit.

For the conventional optical microscopy, a light source is used to illuminate the object. The transmitted or reflected light is collected by an objective to form the image. Thus the resolving power of a microscope mainly relies on the ability of an objective lens focusing light into a small spot. The objective focused light will form a pattern of concentric rings at its focal plane, which is known as Airy disk (Born and Wolf, 1999). According to E. Abbe, for light with wavelength λ, the smallest spot size could be focused into by an objective is

$$d = \frac{\lambda}{2n\,sin\theta},$$
(1.1)

where d is the radius of the center spot of the Airy disk, n is the refractive index of medium light travelling in, θ is the collection angle of the objective. The denominator $n\,sin\theta$ is called numerical aperture (NA). To better define the resolution, L. Rayleigh developed a criterion That the separation between maximums of two Airy disks should be at least equal to d while they still be considered as resolved under optical microscope. Modern high resolution objectives have very high numerical aperture like 1.5. Considering aberrations and experimental conditions, the achievable resolution of the objective lens is usually estimated as $\lambda/2$. For example, oil immersion objective with a numerical aperture of 1.45, using 400 nm visible wavelength as light source, the achievable resolution will be about 200nm. This causes a great obstruction to the development of nanotechnology.

To better understand the origin of diffraction limit, consider the situation of light passing through a periodic grating (**Error! Not a valid bookmark self-reference.**). The wavefronts of light are diffracted according to the Huygens' Principle, forming

constructive and destructive interferences. The constructive interference is given by (Pedrotti and Pedrotti, 1987).

$$dsin\theta_m = m\lambda, \tag{1.2}$$

where θ is the interference angle, λ is the wavelength, d is grating slit spacing, and m is an integer termed diffraction order.
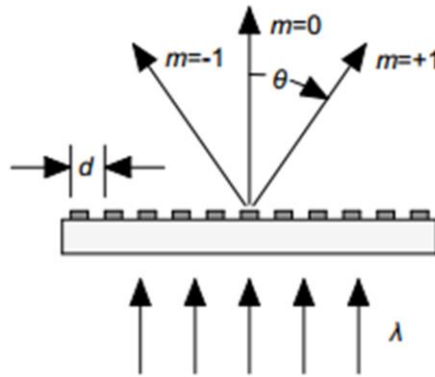
Figure 1.1. Diffraction of light from a grating (Kinzel, 2010).

According to Abbe's theory, the objective must collect the zeroth order and at least one of higher order diffracted lights or two adjacent orders to resolve the grating. This leads to the following criterion

$$sin\theta \geq \kappa \cdot sin\theta_1 = \frac{\lambda}{n \cdot d} \tag{1.3}$$

$$d \geq \kappa \cdot \frac{\lambda}{n \cdot sin\theta} = \kappa \cdot \frac{\lambda}{NA}, \tag{1.4}$$

where θ is the collection angle of the objective, θ_1 is the angle of first order interference, d is the periodicity of grating, n is the refractive index of medium between grating and objective, NA is the numerical aperture of objective, and κ is a constant expressing quality of imaging system, which is 0.5 according to Abbe's criterion.

This result is similar to the diffraction limit proposed by E. Abbe. Besides, from knowledge of Fourier optics, any waves with finite cross section contain non-propagating components. In this case, even if the objective is able to collect wave vectors in all angles, it is only collecting the free propagation waves due to the macroscopic spacing between sample and objective. In this consideration, the diffraction limit could be further improved if these non-propagating components can also be collected, without violation of Heisenberg's uncertainty principle. This brings up the topic of near-field optics.

1.2   The Concept of Near Field Optics

In the effort of developing optical techniques with spatial resolution beyond the diffraction limit, the field of near-field optics has developed. As discussed before, the non-propagating field components, which are sometimes called evanescent waves, have subwavelength lateral variations and attenuate exponentially with distance away from the boundaries where they were formed. A straightforward solution for defeating diffraction limit could be to detect these strongly localized evanescent waves.

E. Synge is considered to be the first one who proposed a scheme for detecting the evanescent waves. In 1928, he wrote a letter to A. Einstein describing a new microscopic method (Novotny, 2007). The method utilizes a tiny particle deposited on top of quartz slide. Through the total internal reflection at quartz surface, this particle can scatter light and acts like a tiny light source. Through scanning the sample over the scatter at a close distance, an image with subwavelength resolution could be obtained.

Later on this method was revised into using a small aperture in an opaque screen (Synge, 1928). Light passing through a tiny aperture can be confined by the dimension of aperture,

providing a tiny light source. Over the years, both of Synge's ideas are experimentally verified and have been developed into two distinct implementations of NSOM, the aperture NSOM and apertureless NSOM.

Besides the efforts to defeat diffraction limit, near-field optics also covers the study of a few other topics: surface plasmon polaritons; surface enhanced Raman scattering; Rayleigh/Mie scattering, etc. Surface plasmon polaritons refer to the plasma oscillation on thin metal film excited by optical beam (Barnes, et al., 2003; Otto, 1968). Surface enhanced Raman scattering (SERS) is phenomenon of high intensity Raman scattering from absorbates on rough metal surfaces (Fleischmann, et al., 1974). Many experimental and theoretical works have been done to understand these phenomena, which also greatly benefit the development of theories for near-field interactions. These studies also provide foundations for the realization of Synge's proposal for near field detection.

In a nutshell, near-field optics is the study of non-propagating inhomogeneous fields and their interaction with matter (Novotny, 2007). By localizing optical energy in subwavelength volume, optical near fields provide the ability for high resolution imaging and help to understand the nature of light matter interactions.

1.3   The Development of NSOM

The method Synge proposed, using subwavelength aperture to achieve high spatial resolution beyond the diffraction limit, had great challenges in technical difficulties. The difficulties of its implementation include maintaining stable subwavelength spacing between aperture source and measured sample; providing accurate lateral scanning of the

sample or aperture relative to the other with subwavelength resolution movements and the fabrication of miniature apertures.

Until the development of the scanning probe microscopy techniques, which made the regulation of subwavelength tip sample distance possible, the exploration of near-field microscopy at optical frequencies started (Novotny, 2007). In the 1980s, two groups firstly realized the near field measurement at visible wavelength separately, achieving a spatial resolution better than $\lambda/10$ (Pohl, et al., 1984; Lewis, et al., 1984).
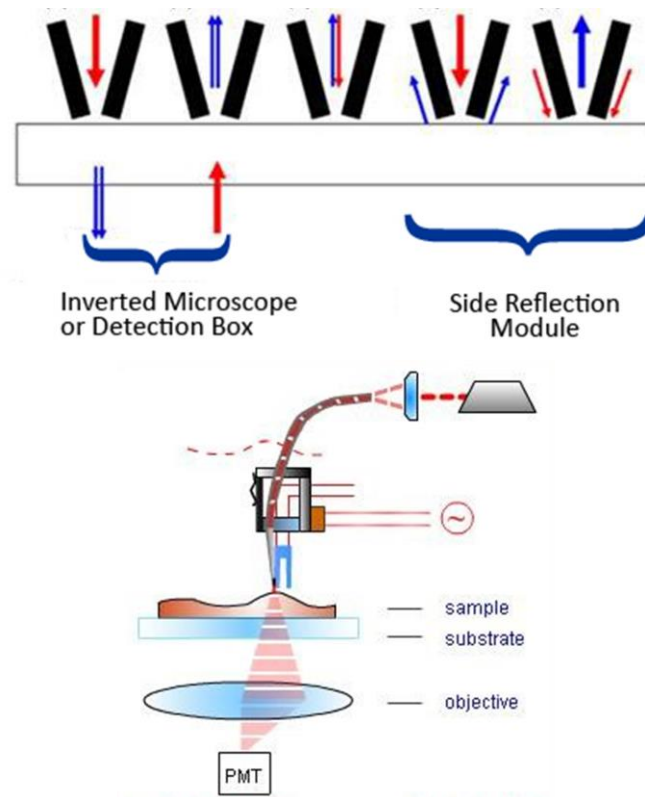
Figure 1.2. A diagram showing tuning fork type aperture NSOM setup (www.ntmdt.com).

After that, the development of technology for near-field optical microscope has been advanced steadily (Figure 1.3). The milestones involve the invention of new NSOM probes. In 1991, a new type of NSOM probe by forming the aperture at end of a metal

coated, tapered single mode optical fiber was invented (Betzig, et al., 1991). Then the tuning fork method of controlling probe sample distance was proposed (Karrai and Grober, 1995). This tuning fork method becomes the most standard mechanism for optical fiber type NSOM (Figure 1.2).

Another variation of NSOM is the photon scanning tunneling microscopy (PSTM) or scanning tunneling optical microscopy (STOM) (Courjon, et al., 1989). This technique uses sharp optical fiber to detect the evanescent field excited by total internal reflection. It finds many applications in the field of optical waveguides and propagation of surface plasmon polaritons.
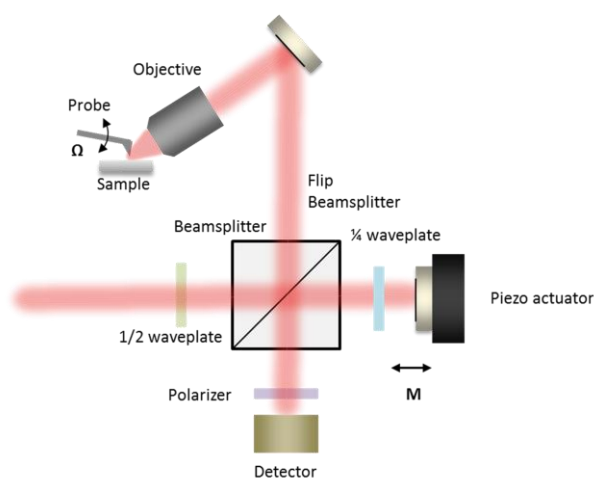
Figure 1.4. A schematic of s-NSOM setup

While aperture NSOM receiving its continuous improvements, Synge's initial idea, using light scattered by a small particle as light source, has also been developed into the apertureless NSOM or scattering NSOM (s-NSOM) (Figure 1.4). The first demonstration was conducted in 1989 (Fischer and Pohl, 1989). In apertureless NSOM, the aperture probe is replaced by the tip of an AFM probe. The tip and sample interaction region is illuminated with a diffraction limited light source which is usually focused by a

conventional lens. The tip enhanced field forms a subwavelength region of optical interaction. The desired near field signals come from scattering from this region, indicating the spatial resolution is only limited by the tip radius, which is generally below 15 nm (Gerton, et al., 2004). Because light scattering happens on both the tip and sample surface, the produced image contains not only the near field information but also the undesired far field background.

The hassle of the overwhelming far field background leads to the development of techniques to suppress the background. Along the way, a method to extract near field signals by dithering tip in vertical direction with frequency Ω and demodulation at higher harmonics $n\Omega$ was proposed (Knoll and Keilmann, 2000; Wurtz, et al., 1998). The homodyne, heterodyne and pseudo-heterodyne interferometry methods were also applied to extract the signal and obtain pure optical amplitude and phase information (Zenhausern, et al., 1994; Hillenbrand, et al., 2001; Ocelic, et al., 2006). Another scheme of cross polarization detection was recently proposed, by applying orthogonal polarization of excitation and scattered radiation the near field information can be obtained with minimum perturbation (Esteban, et al., 2008).

During the progress, it is also realized that the laser irradiated metal tip has so strong enhanced optical intensity than it could be used as an excitation source, especially when incident field is polarized along the probe shaft. This strong scattering scheme receives its further development in spectroscopy, having applications like tip-enhanced fluorescence microscopy and tip-enhanced Raman spectroscopy.

1.4   Outline of this Report

The purpose of this work is to develop an optical imaging technique which could circumvent the diffraction limit and study the optical near field of plasmonic structures especially the bowtie ridge apertures.

Chapter 2 introduces the working principle for aperture NSOM imaging. A home-built aperture NSOM is used to characterize the 3-D optical near field of the bowtie ridge aperture. The light spot produced by a bowtie aperture is demonstrated to have properties of subwavelength dimension and high localization. A transmission enhancement effect resulted from a concentric grating structure is also investigated. The enhancement mechanism is considered to be a combination effect by the grating diffraction and SPP phenomenon.

Chapter 3 introduces a different type of NSOM – the scattering NSOM (or s-NSOM). The mechanism of how does scattering NSOM achieve high resolution is explained. The factors determining the resolution of a s-NSOM are discussed. To deal with background noises in the implementation of s-NSOM, different detection schemes are presented. These detection schemes are firstly evaluated by mathematical derivations. The mathematical derivations show the disadvantages and advantages between the different methods. The pseudo-heterodyne method stands out and is adopted for this work.

Chapter 4 introduces the home-built s-NSOM. This setup implements the pseudo-heterodyne interferometric method. The procedures for s-NSOM operations are described in detail. The importance of achieving a stable and uniform interference is also emphasized. This setup has been used to measure the near field distribution of a circular aperture array. The obtained result is compared with results obtained using non-

interference scheme and homodyne scheme. The measurement of the optical near field around a single slit is also conducted. The formation mechanism of the experimental observed fringes is also explored.

Chapter 5 introduces the transmission type s-NSOM. The details of the setup and operation procedures are described. With this setup, the optical field distribution of a bowtie aperture is further investigated. The influence of the high harmonic demodulation method is investigated for both interferometric and non-interferometric measurements. Then the 3-D mapping of the field formed by a bowtie aperture is conducted. For the measurements with a transmission type s-NSOM, both optical amplitude and phase information can be simultaneously obtained.

Chapter 6 presents the summary of this report and recommendations for future work. It introduces some potential work to improve the understanding of signals obtained from s-NSOM. It then discusses the measurement of optical vector fields. At the end, a few suggestions on the sample fabrication process are provided.

CHAPTER 2.   APERTURE TYPE NSOM

In this chapter, the mechanism of aperture near-field optical microscope is explained. The details and capability of a home-built NSOM are illustrated. With this home-built aperture NSOM, the near-field characteristics of a bowtie ridge aperture are explored. To further investigate the nano-focusing mechanism, an extraordinary transmission antenna structure is also designed and experimentally verified with this home-built NSOM.

2.1   The Principle for Aperture NSOM

Optical fields can be described as a superposition of propagating waves and evanescent waves. The propagating waves contain most significant information of the object, while evanescent waves are related to the fine details. In a conventional optical microscope, only the propagating waves can be collected, which sets a limit to the imaging resolution. To achieve high spatial resolution, an obvious method is to also capture the evanescent component of optical fields. In aperture NSOM, a subwavelength aperture of AFM probe in close vicinity of sample surface can be used to collect the evanescent waves and convert them into propagating mode. With the additional non-propagating information, the NSOM technique can achieve a resolution beyond the diffraction limit.

The mechanism of converting evanescent waves into propagating mode is explained here. For simplicity, an analytic two dimensional case will be used to illustrate the principle of

imaging in NSOM. This method was initially applied by Massey, and extended by a few researchers (Novotny and Hecht, 2006; Vigoureux, et al., 1992; Massey, 1984). Consider a small slit on a screen with a width of 2L. The far field detector is placed at a large distance of $z = Z$ from the sample surface. A simplified aperture probe, which is represented by another small slit on a screen is placed at a distance of ϵ. The distance ϵ is much smaller than the wavelength. Figure 2.1 shows a schematic of the simplified model of aperture near-field optical microscope. The first screen represents the sample surface, while the slit in it represents a nanometer size feature.
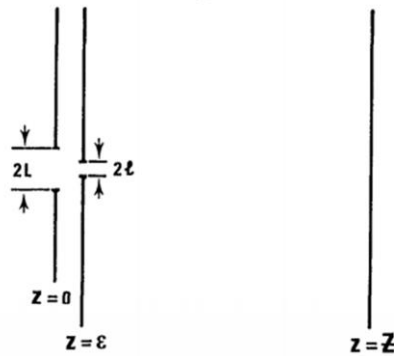
Figure 2.1. A simplified model of aperture NSOM (Vigoureux, et al., 1992).

A monochromatic field $E_0=(x, z)$ propagates along z direction. Using the angular spectrum representation (Novotny and Hecht, 2006), this source field could be expressed in terms of its spatial spectrum as (Novotny and Hecht, 2006; Vigoureux, et al., 1992)

$$E_0(x,z) = \int_{-\infty}^{+\infty} E_0(k_x,z)\exp(ik_x x)dk_x. \qquad (2.1)$$

The field just behind the slit (at z=0) could be approximately expressed as

$$E_1(x,z=0) = E_0(x,z=0) \cdot rect(\frac{x}{2L}) \qquad (2.2)$$

$$rect\left(\frac{x}{2L}\right) = \begin{cases} 0 \text{ if } |x| > L \\ 1 \text{ if } |x| < L \end{cases}. \tag{2.3}$$

If there's no aperture probe, the field detected at the distance Z will be

$$E_d(x, z = Z) = \int_{-\infty}^{+\infty} E_1(k_x, z = 0)e^{-i\sqrt{k^2-k_x^2}Z}e^{ik_xx}dk_x, \tag{2.4}$$

where k is the wave number. For two dimensional problems, $k_z = \sqrt{k^2 - k_x^2}$, where k_z could be positive or negative. Although Equation (2.4) integrates from $-\infty$ to $+\infty$, the fields captured by the far field detector will only be the propagating components, which has a wave number of $|k| \leq \frac{\omega}{c}$. Thus, for conventional optical microscope, the measured field will be

$$E_d(x, z = Z) = \int_{-\frac{\omega}{c}}^{+\frac{\omega}{c}} E_1(k_x, z = 0)e^{-i\sqrt{k^2-k_x^2}Z}e^{ik_xx}dk_x. \tag{2.5}$$

Now consider the model of Figure 2.1, with a small slit in close vicinity to the sample. By similar approximation, the field captured by the detector after radiating from second slit could be written as

$$\begin{aligned} E_d(x, z = Z) &= \int_{-\frac{\omega}{c}}^{+\frac{\omega}{c}} dk_x e^{-i\sqrt{k^2-k_x^2}(Z-\epsilon)}e^{ik_xx} \\ &\cdot \int_{-\infty}^{+\infty} E_1(k_x', z = \epsilon)e^{-i\sqrt{k^2-k_x^2}\epsilon}rect\left(\frac{k_x - k_x'}{2l}\right)dk_x'. \end{aligned} \tag{2.6}$$

The term $rect\left(\frac{k_x-k_x'}{2L}\right)$ is the Fourier transform of rectangular function that could be written as $2\frac{\sin(k_x-k_x')l}{(k_x-k_x')}$.

Equation (2.5) and (2.6) show the results by far field and near field detection respectively. Consider a random spatial frequency K

$$E_1(k_x, z = 0) = E_1 \delta(k_x - K). \tag{2.7}$$

The far field measurement Equation (2.5) becomes

$$E_d(x, z = Z) \begin{cases} = E_1 e^{-i\sqrt{k^2 - K^2} Z} e^{ik_x x} & when \ K < \dfrac{\omega}{c} \\ = 0 & when \ K > \dfrac{\omega}{c} \end{cases} \tag{2.8}$$

This confirms that in far field measurement, all information of the high spatial frequencies is lost.

Conduct the same calculation for Equation (2.6), the following result could be obtained

$$E_d(x, z = Z) = E_1 e^{-i\sqrt{k^2 - K^2} \epsilon}$$

$$\times \int_{-\frac{\omega}{c}}^{+\frac{\omega}{c}} dk_x e^{-i\sqrt{k^2 - k_x^2}(Z - \epsilon)} e^{ik_x x} \cdot 2 \frac{\sin(k_x - K) l}{(k_x - K)}. \tag{2.9}$$

In this case, the spatial frequency $K > \dfrac{\omega}{c}$ will be partially collected and contributes to the imaging process, providing the subwavelength details of the object. This could also
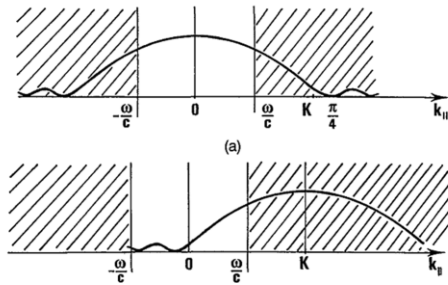
Figure 2.2. Convolution of source field and collecting slit (Vigoureux, et al., 1992).

explained by the convolution process between source field and slit transmission. Convolution shifts the higher spatial frequency components into the detection region, thus improves the resolution. Figure 2.2 gives an intuitive illustration.

2.2   Home-built Aperture NSOM System

The work presented here is done on a home-built aperture NSOM. This NSOM is based

on two commercial control modules from RHK Technology, the AFM100 module and

SPM100 module. The NSOM was initially built for collection mode (Wang, 2008). Now

there are two configurations, which can be easily switched between each other. This

NSOM is based on common Atomic Force Microscope technique. The commonly used

optical lever feedback mechanism is applied for its high sensitivity and easy to
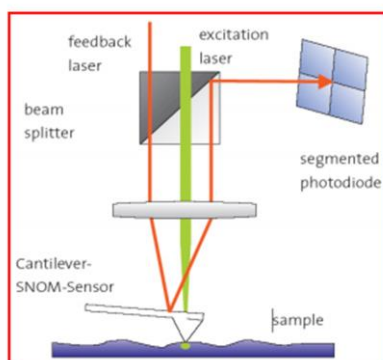
Figure 2.3. Illustration of optical lever feedback mechanism
(http://www.olympusmicro.com).

implement. A cantilever type probe is used for collecting the near field signals, which has

a tiny aperture at its apex. A laser beam from a diode laser is focused onto the back

reflective surface of cantilever by a convex lens. The reflected light shoots on a four

quadrant position sensitive detector (PSD) for monitoring the deflection change of the

cantilever. For a rectangular shape cantilever, the reflected light will be a spot; for a

triangular shape cantilever, an interference pattern will be formed upon reflection, which

can be used for feedback. When tip scans the sample, the sample's surface features will

cause a change in the deflection of the cantilever. As a result, the reflected laser spot will

be projected to different location on PSD. The surface of PSD is divided into four segments. Generally the signal difference between the upper part and the lower part will be used to provide feedback, which is called normal force signal. Figure 2.3 illustrates the optical lever mechanism.
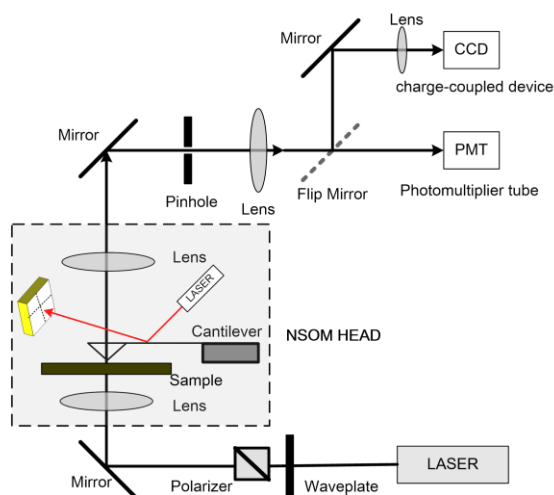
Figure 2.4. Schematic of home built NSOM setup (Guo, et al., 2010).

Near the PSD, a preamplifier is placed as close to it as possible. This is to minimize the environmental noise to provide a high signal to noise ratio. The PSD voltage signal is amplified by the preamplifier and sent to the AFM100 module. The AFM100 module can process the signals from PSD, and generate different signals for feedback and mapping, such as the normal force signal, lateral force signal, error signal, total signal, etc. These processed signals are provided as inputs for the SPM100 module. The SPM100 module is a versatile control system which can be used for different scanning probe technologies. The diode laser, PSD, and cantilever are all built into the scanner head, which is supported by three Picomotors. The Picomotors are also used for coarse approaching to sample. The sample is placed on a three axis piezo stage. During the approach, the

SPM100 activates the Picomotors to bring tip towards the sample. After deflection of the cantilever is detected and achieves a set point, the Picomotors will stop moving and hold their position. The SPM100 will activate the feedback loop and drive the piezo stage to respond to error signal from PSD. In this way, a constant set point is maintained. With the feedback loop functioning, the topography and other sample surface information are mapped.
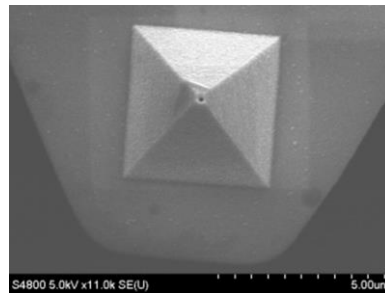
Figure 2.5. An example NSOM probe with aperture on its tip.

A description of the optical configurations of NSOM is explained here. Figure 2.4 illustrates the configuration for collection mode NSOM. The sample is illuminated from the bottom by a linearly polarized laser source. A 10X objective is placed at the bottom of sample to focus the laser to interested region on the sample. The optical fields on sample surface are collected through the aperture of NSOM probe. NSOM probe is made from commercially available silicon nitride AFM probes (Figure 2.5). The optical signals that go through the NSOM probe are detected by far field optics. A 50X long working distance objective on top of scanner head is used to collect the photons from probe aperture. The photomultiplier tube (PMT) is used to detect the weak signals. The SPM100 has built-in photon counting circuits, which gives the measured result in the form of photon counts instead of light intensity. In the optical path, an optical laser line

filter is used to filter out environmental lights, especially the diffracted light of the feedback laser from the cantilever and sample surface. A small pinhole is also used to ensure the detected signal only comes from probe aperture. The optical path can be directed by a flip mirror to a CCD camera, for easy alignment and adjustment.

The main frame of illumination mode aperture NSOM is the same as in collection mode. In illumination mode, the laser source is focused by the top 50X objective onto the back side of the cantilever. The light going through the probe aperture acts as a tiny light source. The optical response of sample surface transmits through the sample substrate, and is collected by another 50X objective placed at bottom of the sample. The collected photons are directed through similar optical components as in collection mode, and then detected by the PMT.

2.3   Three Dimensional Measurement of Optical Near Field

2.3.1   Transmission through Subwavelength Ridge Aperture

Nanoscale aperture has the characteristic of forming a subwavelength light spot, providing the basis for direct write nanolithography system, NSOM, and many other applications. A simple case will be a light source illuminating an aperture defined in a thin opaque metal film. The investigation of the diffracted fields near the aperture in metal screen has been analytically performed by H. Bethe (Bethe, 1944) and generalized by C. J. Bouwkamp (Bouwkamp, 1950). Bethe assumed the metal film is infinitely thin and metal is perfect conductor. He derived a simple expression for the normalized transmission efficiency

$$\eta_B = \frac{64(kr)^4}{27\pi^2},$$

(2.6)

where $k = 2\pi/\lambda$ is the wave number of incident light, r is the radius of the aperture. This equation predicts that the transmission will be very weak for a tiny aperture because of the inverse relationship of aperture size. For example, A laser source with wavelength of 488 nm, incidents on an aperture with 50nm diameter, the transmission efficiency will be about 2.7×10^{-3}. This low transmission efficiency sets the main limit for practical applications. For real aperture, the film has certain thickness. Thus the aperture will have waveguide properties, which complicates the problem (Roberts, 1987). Later experimental results show that there are resonances at specific wavelengths or surface modes and evanescent waves involved, which could greatly enhance the transmission through subwavelength apertures. This phenomenon attracts many interests and leads to the topic of extraordinary transmission because of the variety potential applications.

Many efforts have been made to design a subwavelength structure that could improve the transmission efficiency while maintain the desired confinement. It is demonstrated that the bowtie type ridge aperture has the capability of providing both high transmission enhancement and high spatial confinement of light spot (Oesterschulze, et al., 2001; Sendur and Challener, 2003). Many experiments and numerical simulations have been conducted to demonstrate the enhancement in transmission. The near field optical intensity distribution of bowtie aperture has been characterized by many groups using the method of NSOM (Wang and Xu, 2007). However, a full three dimensional investigation of the optical fields was not performed. The following section gives a measurement of the optical fields at different gaps between probe and sample, thus provides an idea of the

three dimensional distributions of optical field after the bowtie aperture (Guo, et al., 2010).

<div align="center">2.3.2   Experiment Details</div>

The measurement is performed on the home-built aperture NSOM, working in the collection mode. The sample is a 150 nm thick aluminum film, which is thermally evaporated onto the optical flat quartz substrate. The nanoscale bowtie apertures are milled by focused ion beam (FIB) technology. The fabricated bowtie (illustrated in Figure 2.6) has an outline dimension of 260 nm × 260 nm. The center gap has a width of 62 nm. A silicon nitride probe from Veeco is coated with 100 nm aluminum film on the tip side and subsequently milled a 150 nm diameter aperture at its apex by FIB. The cantilever has a nominal stiffness of 0.58 N/m and operates in contact mode. To measure the three dimensional optical fields, the feedback loop is disabled after initial measurements in contact with the sample surface (tip sample distance is 0). Then measurements at different tip sample distances are performed by manually adjust the piezo position in Z direction. The laser source for excitation is 488 nm Argon ion laser.
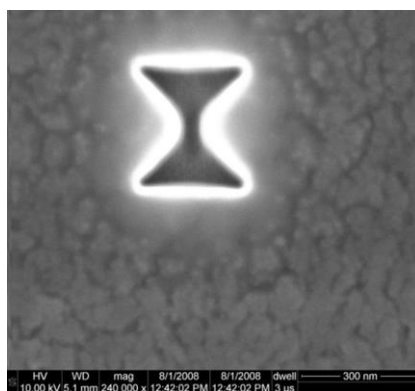
Figure 2.6. SEM image of the measured bowtie aperture (Guo, et al., 2010).

Bowtie aperture has a strong polarization dependence. A measurement is carried out in contact mode to verify the dependence, by varying the incident polarization direction. For the measurement, the scanning speed is 1.95 μm/s. A region of 1 μm by 1 μm is scanned, with a resolution of 64 × 64 pixels. The measured results are shown in Figure 2.7. The illumination polarization affects not only the field intensity, but also the shape of the focused light spot. For polarization in x direction, a circular focused spot is obtained. The full width at half maximum (FWHM) of the light spot is about 157 nm. The peak intensity is 160 kHz photon counts. For polarization in y direction, multiple spots at corners of bowtie aperture are obtained. This corresponds to undesired waveguide propagating modes. The peak intensity is also much lower, which is 30 kHz photon counts. After subtraction of the 5 kHz counts noise, there is more than 6 times difference in peak intensity.
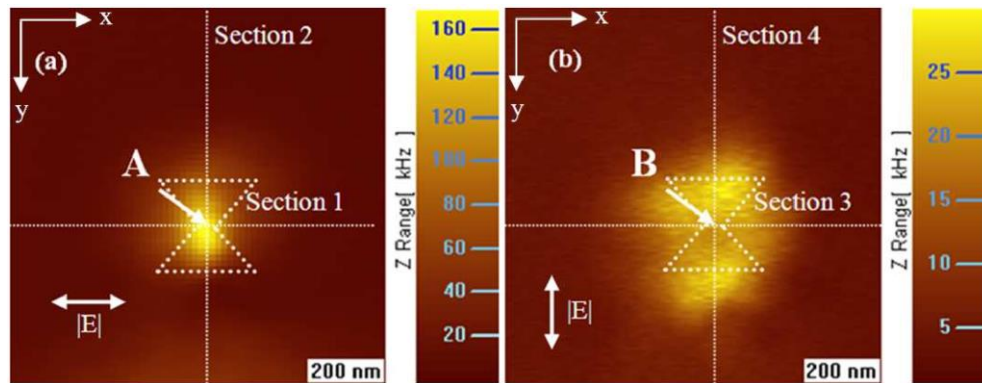
Figure 2.7. Near field images of bowtie aperture acquired in contact mode. The scan size is 1 μm × 1 μm. The excitation laser is polarized along the x-direction (a) and y-direction (b). The intensity color scales are different in the two figures (Guo, et al., 2010).

To better understand the effects of different polarization directions, a simulation is carried out by a commercial software (HFSS from Ansoft) (Guo, et al., 2010). This software implements the frequency domain finite element method. The simulation model

is built according to the real experimental conditions. The simulation results are shown in Figure 2.8. There are two perpendicular section views for both x and y polarizations. Under x polarization, the energy is mainly coupled in the gap region. A single confined spot is formed within the gap. While under y polarization, there's no hot spot in the gap region. Higher propagation modes are excited. Multiple hot spots are formed at bowtie edges.
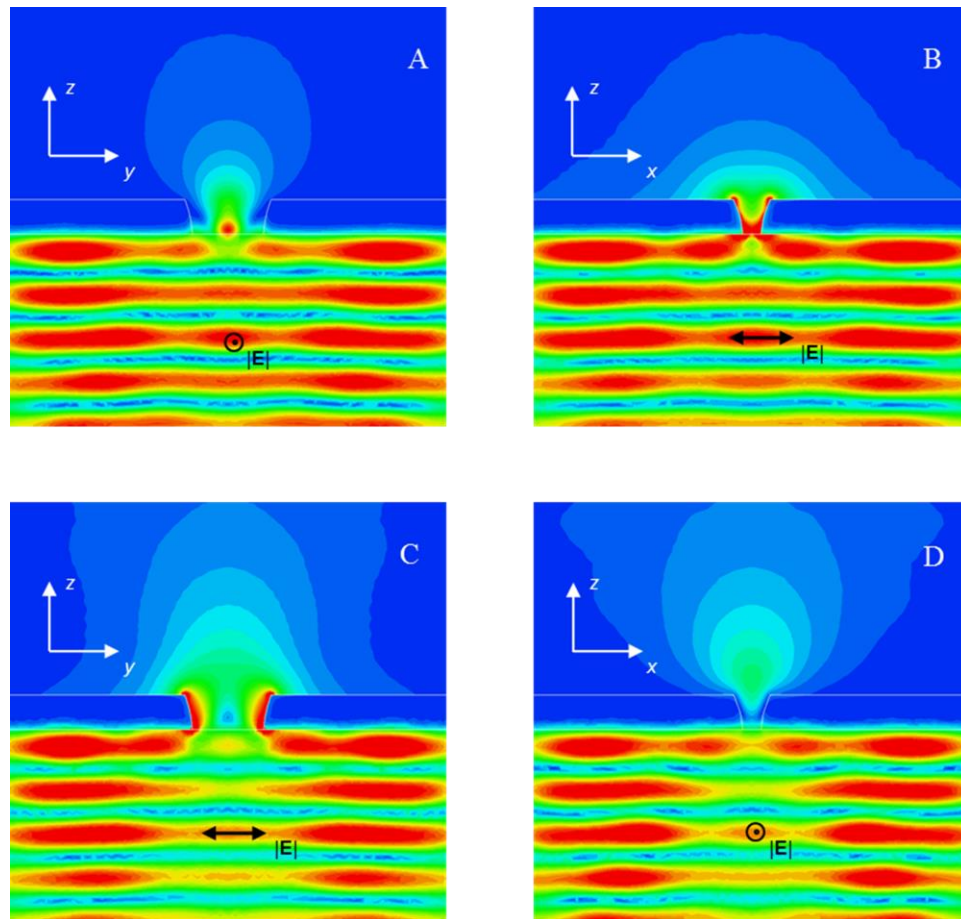
Figure 2.8. Electric field distribution of bowtie aperture with x-polarized excitation (A, B) and y-polarized excitation (C, D) (Guo, et al., 2010).
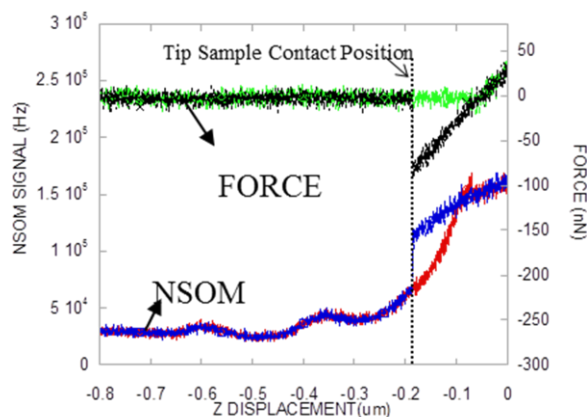
Figure 2.9. NSOM signals and force displacement curve at center in Figure 2.7 (a). Tip approach direction: green and red; tip retraction direction: black and blue (Guo, et al., 2010).

As mentioned above, the three dimensional measurements can be performed with the feedback loop disabled and manually set the tip sample distance. The tip sample distance is calibrated by measuring the force displacement curve (F-z curve). Figure 2.9 shows the measured force displacement curve with NSOM signal simultaneously collected. The green curve is the approach curve, while the red curve is the simultaneously collected NSOM signal. The black curve and blue curve are the retraction curve and NSOM signal respectively. The sudden signal drop in approach curve is the tip jumping into contact point. The intersection of zero force line and repulsive section of approach curve is considered as the position of z=0. The simultaneously measured longitude NSOM signal also provides rich information about the field distribution close to the bowtie aperture. The photon counts in the red curve decay rapidly into a level close to background noise when tip-sample distance becomes larger than 200 nm. This shows the evanescent characteristic of the near field subwavelength light spot. It's also observed that there are

some periodical peaks in the curve when the distance becomes larger than 200 nm. This should be caused by the interference from reflection lights by the sample and cantilever.
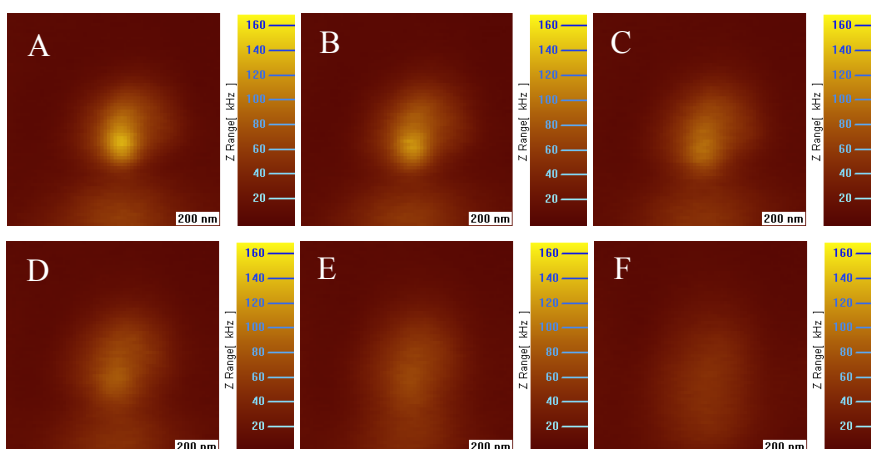
Figure 2.10. Constant height NSOM images at different tip-sample distances: 50 nm, 75 nm, 100 nm, 125 nm, 150 nm, and 200 nm in A - F, respectively. The laser polarization is in x-direction (Guo, et al., 2010).
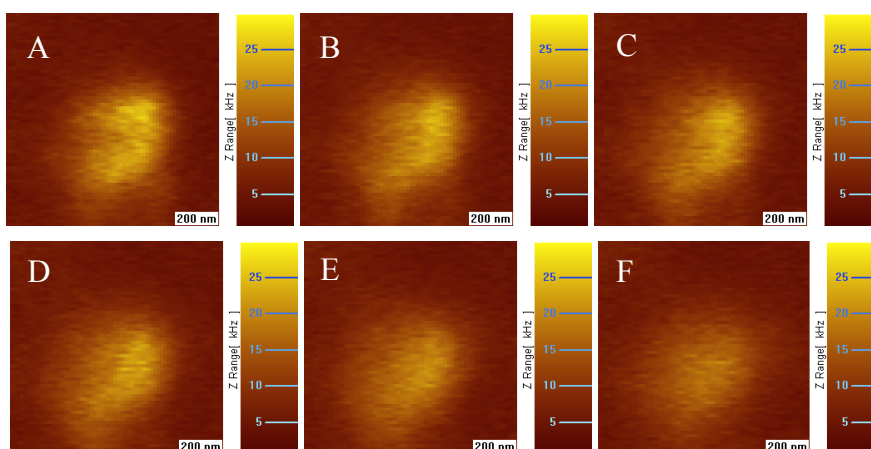
Figure 2.11. Constant height NSOM images at different tip sample distances: 50 nm, 75 nm, 125 nm, 125 nm, 150 nm, and 200 nm in A - F, respectively. The laser polarization is in y-direction (Guo, et al., 2010).

With the help of F-z curve, a series of NSOM images can be collected at different longitude tip sample distance. The distances are selected as 50 nm, 75 nm, 100 nm, 150 nm, and 200 nm. The scan size is chosen to be 1 um × 1 um, 64 × 64 pixels. The NSOM results at different heights could be combined to give an idea of the 3D field distribution of bowtie aperture. Figure 2.10 shows the NSOM signals at six different heights, with

incident laser polarization in the x direction. Figure 2.11 shows the similar results, with
the incident laser polarization in the y direction. The rapid divergence trend of near field
light spot can be seen easily from the images.
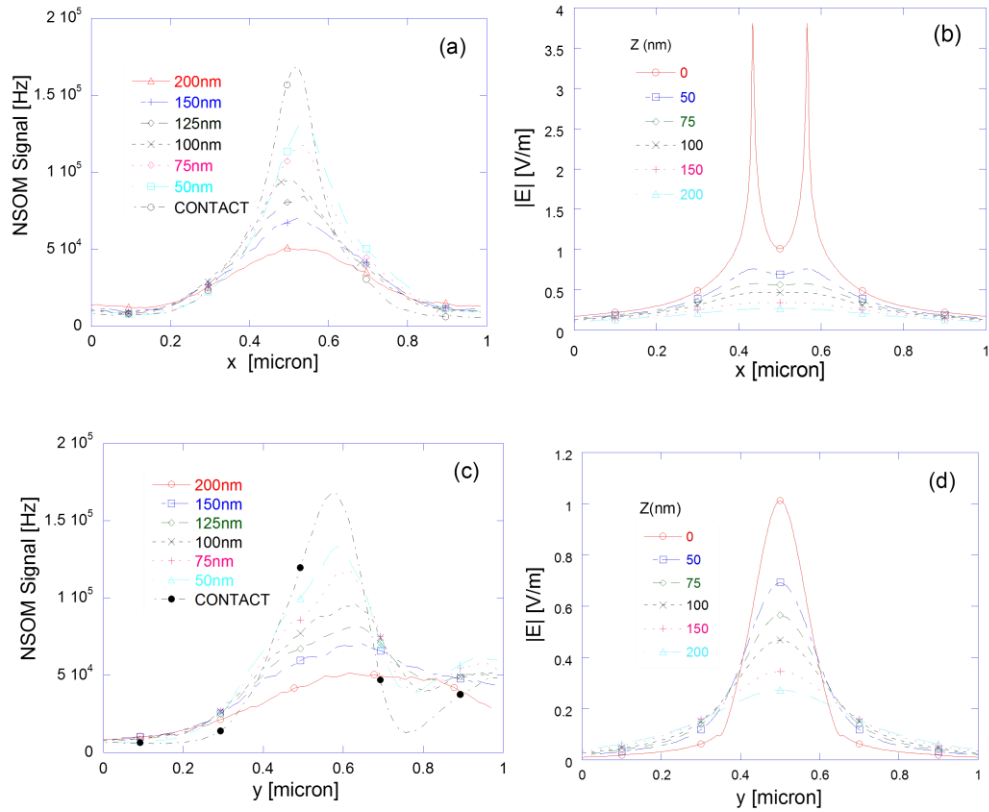
Figure 2.12. Experimental and theoretical intensity distribution along sections 1(a) (b)
and section 2(c) (d) of Figure 2.7 (a) at different heights for laser polarization in the x-
direction (Guo, et al., 2010).

To further understand the three dimensional optical field distribution, the cross sections at
different heights are plotted and compared with simulation results. Figure 2.12 shows the
cross sections for polarizations in x direction along x and y directions. For the cross
section of 50nm distance in x direction, the peak count is 132 kHz. The peak drops to 49
kHz at the cross section of 200 nm distance. This gives a factor of 2.7 in difference. The
corresponding simulation results give peak intensities of 0.76 and 0.27, which give a

factor of 2.8 in difference. The simulation result also shows that there're double peaks in the cross section of x direction, which have a separation of 62 nm. This feature is not resolvable because of the relative large probe aperture of 150 nm diameter.
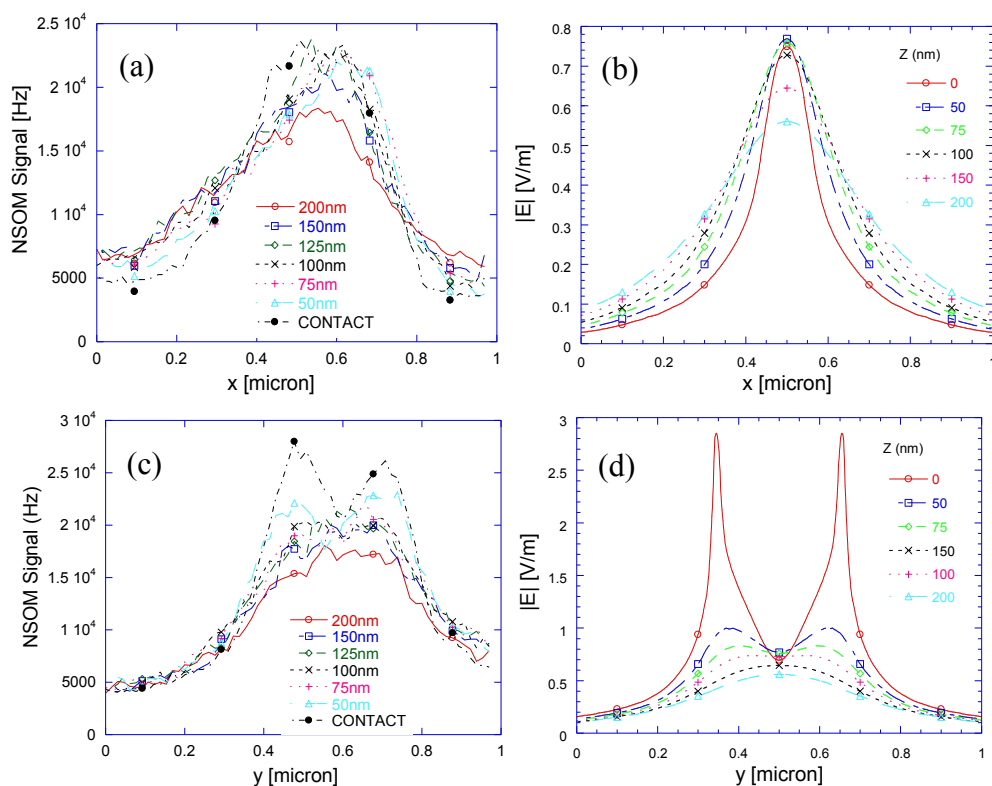
Figure 2.13. Experimental and computed intensity distribution along sections 3(a) (b) and 4(c) (d) in Figure 2.7 (b) at different heights for laser polarization in the y-direction (Guo, et al., 2010).
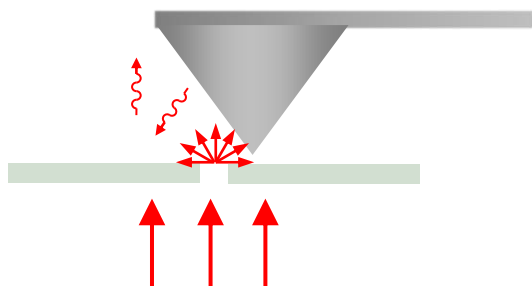
Figure 2.14. Illustration of how undesired light comes to detector.

In the cross section of experiment result in y direction, there is a raise in background noise. This is mainly due to the photon leaking from the edge of probe cantilever. Because of the shape of the cantilever, when it scans the upper part of the chosen region, the reflections between sample and cantilever could be blocked by cantilever. However, when the tip scans the lower part of the region, because of the bowtie aperture will be close to the edge of cantilever, the leaking will easily come into the detection region (shown in Figure 2.14). Figure 2.13 shows the results of cross sections for laser polarization in y direction.

2.4   Extraordinary Transmission of Bowtie Aperture with Corrugations

As discussed earlier, while subwavelength apertures provide near-field confinement, the transmission efficiency of these apertures hardly fulfill the requirements of applications like near field imaging, nanolithography, and data storage, etc. Two main approaches are proposed to improve the strength of subwavelength spot: modifying the shape of the aperture and increasing the amount of light coupled into the aperture. Simulations and experiments show that replacing circular aperture with ridge aperture will boost the transmission efficiency to well above unity, which is about $1000\times$ enhancements (Jin, 2006). Meanwhile, the effect of light interacting with structured metal has been found to have extraordinary transmission. The light transmitted through holes arrays and holes surrounded by corrugations (Lezec, et al., 2002) shows orders of magnitude larger than expected. The total transmitted power thus far exceeds the radiation incident on the open area of the aperture.

To investigate how the effect of extraordinary transmission could improve the light transmission through a bowtie aperture, a concentric grating structure is sculpted around a single bowtie aperture. This grating structure functions similarly to a Fresnel zone plate with zero working distance, focusing light at its center. The focus confines light to a $\lambda/10$ size spot. Simulation and experimental examination are performed to understand the transmission process (Kinzel, et al., 2010).
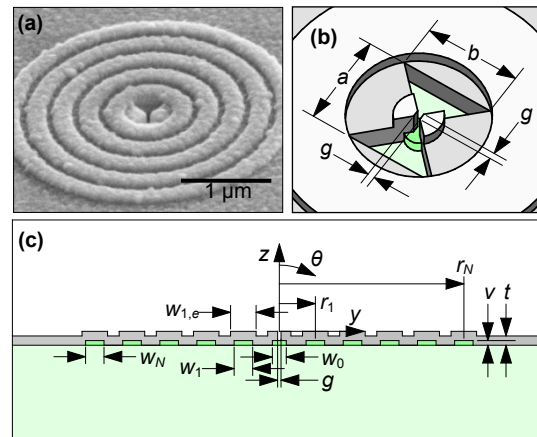
Figure 2.15. Structure geometry. (a) SEM image showing aluminum surface and milled aperture, (c) schematic of aperture and grating geometry (Kinzel, et al., 2010).

The sample is prepared with e-beam lithography (EBL) and focused ion beam (FIB) techniques. A 140 nm thick indium tin oxide (ITO) film is deposited on a flat fused silica substrate using e-beam evaporation. This ITO film is baked at 550 ^{0}C for 2 hours in N_2. A 50 nm thick hydrogen silsesquioxane (HSQ) is then spun on top of the ITO layer and prebaked at 120 ^{0}C for 1 minute. After that, the concentric ring grating is fabricated with EBL. The HSQ is firstly developed and post baked at 550 ^{0}C for 2 hours. The ITO layer is necessary for conductivity of substrate and allowed dissipation of charges during EBL fabrication. A 100 nm thick Al film is deposited on top of the HSQ and ITO, also using e-beam evaporation. In the end, the bowtie aperture is milled by FIB (FEI Nova 200, 30 kV

1 pA, Ga^+ ion beam). The Al film conformed to the grating structure to form the corrugation surrounding the bowtie aperture. Figure 2.15 shows the SEM image and schematic of sample structure.

The grating structure is symmetric about the central axis. All grooves are designed to have the same depth of 50 nm. The nth groove is defined by its width W_N and the distance r_N from the central axis. The width of conformed Al grating is slightly larger than the width of HSQ grating, with $W_{N,e} = W_N + 75$ nm. The bowtie aperture is milled through the center metal protrusion. This slightly lowers the enhancement provided by the grating structure because the aperture is lower in substrate side which makes it less efficient in capturing the laterally diffracted light. The advantage of fabricating aperture on the exit plane side is to place the focused near field spot to the most front of the sample, thus it interacts directly with media like photoresist. Aluminum is chosen because of its higher plasma frequency than either gold or silver.

For comparison, the structure is fabricated with different grating periodicity. While r_1 is fixed at 387.5 nm, $r_{n+1} = r_n + p$. The slot width W_n is also fixed at 200 nm, except the center post width W_0 is 100 nm. The milled bowtie aperture is kept constant at $a = b = 350$ nm, nominally. The center gap g of bowtie aperture, which is the smaller the better, decides the size of focused near field spot.

Far field transmission measurement is firstly carried out on identical bowtie apertures with and without grating structure. The sample is illuminated with a linearly polarized HeNe laser beam ($\lambda = 632.8$ nm). A CCD camera is used to capture images at the sample exit plane. An integration over the bright spot is performed to get the intensity. Each measurement is repeated on five identical structures to get the average. The enhancement

is normalized to transmission through the single bowtie aperture without grating structure (Figure 2.16). The experiment results show that adding the grating structure enhances the far field transmission by a factor of ~7.

To further exam the enhancement in the focused near field spot, aperture type near field optical microscope measurement is performed. For this measurement, a probe with 100 nm diameter aperture is used. Figure 2.16 (d) shows the near field enhancement is about 15 times compared to bowtie aperture without grating structure.
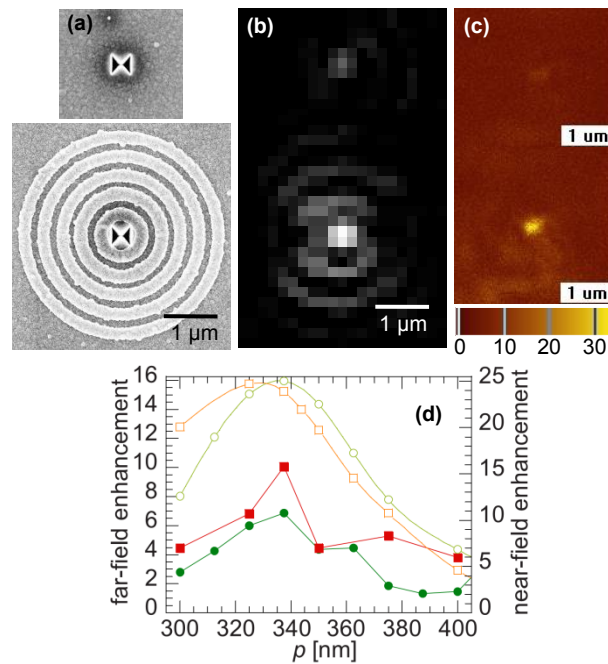
Figure 2.16. Experimental results for bowtie aperture without and with grating. (a) SEM images (b) far-field images, (c) NSOM images and (d) experiment and simulation results of enhancement (Kinzel, et al., 2010).

To understand the physics behind these phenomena, frequency domain finite element method (FEM) simulation is carried out using Ansoft HFSS commercial software (Kinzel, et al., 2010). Figure 2.16 (d) shows the enhancement calculated from simulation for both near field and far field. It also indicates there is a discrepancy of about 2 times, which

could be a result of imperfection in the fabricated structure. Figure 2.17 shows the calculated electric field intensity distribution of bowtie aperture with grating structure. The inset image shows the result of a similar simulation for a single bowtie aperture without grating structure. There's a standing wave formed by reflection from Al film in the inset image. While, for the sample with grating structure, the standing wave is disturbed, and light is concentrated toward the center aperture. From the view of conventional optics, this disturbance could be understood as interference formed by diffraction of grating structure. This means the fundamental enhancement mechanism could be a grating phenomenon, which is confirmed by simulating the metal film as perfect electric conductor (PEC) (Garcia-Vidal, et al., 2003), opposing to be plasmonic. However, by making the film out of real metal, surface waves especially localized surface plasmon (LSP) resonances also contribute to the enhancement. Thus the transmission enhancement is a combined effort of dominant grating diffraction and non-negligible SPP.
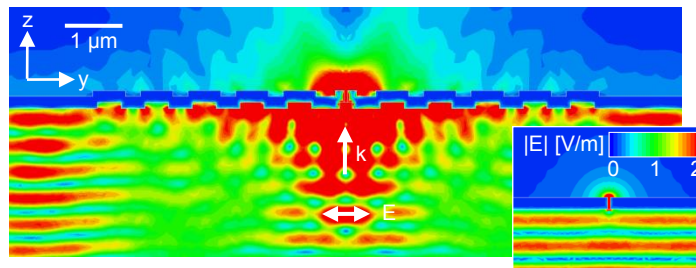
Figure 2.17. Simulations of transmission from the grating and aperture. Plotting electric field on yz plane. The inset shows the electric field for the bowtie aperture. Both images are saturated at 2 V/m (Kinzel, et al., 2010).

2.5 <u>Conclusion</u>

In this chapter, the theory for aperture type near field scanning optical microscope is explained. The three dimensional optical near field distribution from a bowtie aperture is characterized with a home built NSOM system. The experiment results demonstrate the near field nature of bowtie focused light spot, which is its high localization and rapid decay away from the sample surface. The sensitivity of bowtie aperture to the polarization of illumination light is also explored. When laser light is polarized in x direction, a single focused spot is obtained, with a FWHM of 157 nm, which is limited by the size of NSOM probe. When laser light is polarized in y direction, multiple spots are formed. The spot sizes are considerably larger than the one from x polarization. These measurements are consistent with theoretical prediction about the near field distribution of the bowtie aperture from simulation work. A concentric grating structure is added to a single bowtie aperture to further enhance transmission efficiency. While far field measurement is carried out with a regular CCD imaging system, the near field measurement is performed on the same home built NSOM system. Both results show a few times increase in transmission. From the relevant simulation, the enhancement mechanism is understood as the combined effort of grating diffraction and SPP.

CHAPTER 3. S-NSOM THEORY AND MEASUREMENT TECHNIQUES

While the invention of aperture NSOM greatly improves the optical resolution, the cut off effect sets a limit to its implementation. When the aperture diameter is below $\lambda/2$, the light propagation becomes evanescent (Genet and Ebbesen, 2007). Since the excitation EM field cannot be increased arbitrarily due to the low damage threshold of metal coating (~10 mW), the achievable resolution is limited (Hecht, et al., 2000). For visible wavelengths, working with a very small aperture (< 50 nm) is usually impossible. To overcome this wavelength dependent resolution limit, the alternative NSOM principle was explored. The enhanced field in the vicinity of a small particle is used as an optical nano source, instead of the light transmitted through a small aperture. When a sample is presented, the near field interaction between probe and sample will carry information about the sample, and be measured in the far field. This is the so called apertureless NSOM (ANSOM) or scattering NSOM (s-NSOM).

3.1 Field Confinement and Enhancement

The implementation of s-NSOM is also based on AFM technology. An illumination light is focused onto the apex of an AFM tip. The strongly localized field formed in its vicinity is used to probe the optical property of a sample. When doing AFM scans, an optical map

will be simultaneously acquired while collecting topographic information of the sample. The key aspect of s-NSOM is the highly confined and enhanced field near the apex of AFM tip.

It has been shown that the field confinement, which decides the lateral resolution, is only determined by the radius R of the tip curvature (Bohn, et al., 2001). Meanwhile, the field enhancement plays an essential role in amplifying the scattered signal from the tip. The enhancement generally comes from a few origins: The lightning rod effect, the optical antenna effect, and the localized surface plasmon resonance, etc.

3.1.1   Lightning Rod Effect

Lightning rod effect refers to the phenomena of fields concentrating at regions of high curvature, resulting from the electromagnetic boundary conditions. It is purely a shape effect, thus does not have any wavelength dependence. A simple illustration of this effect is to consider a dielectric sphere resident in a static electric field. Assuming the diameter of the sphere is much smaller than the wavelength, a quasi-static approximation could be made. By applying Maxwell's equation at the boundary of sphere, the electric field distribution inside and outside the sphere could be solved analytically, which is available in most electrodynamics textbooks (Jackson, 1999),

$$\boldsymbol{E_{out}}(r,\theta) = E_0 cos\theta \left(1 + 2 \cdot \frac{\epsilon/\epsilon_0 - 1}{\epsilon/\epsilon_0 + 2} \cdot \frac{a^3}{r^3}\right) \cdot \hat{\boldsymbol{r}}$$

$$+ E_0 sin\theta \left(-1 + \frac{\epsilon/\epsilon_0 - 1}{\epsilon/\epsilon_0 + 2} \cdot \frac{a^3}{r^3}\right) \cdot \hat{\boldsymbol{\theta}}$$

(3.1)

$$\boldsymbol{E_{in}}(r,\theta) = E_0 \frac{3}{\epsilon/\epsilon_0 + 2}\left(cos\theta \cdot \hat{\boldsymbol{r}} - sin\theta \cdot \hat{\boldsymbol{\theta}}\right), \tag{3.2}$$

where a is the radius of the sphere, $\boldsymbol{E_0}$ is the applied uniform field, ϵ is the permittivity of sphere, while ϵ_0 is the permittivity of ambient medium. The final results show that the field inside the dielectric sphere is uniform and in the same direction of the applied field, while the field outside the sphere is a superposition of the applied field and the field of an electric dipole $\boldsymbol{P} = \frac{3(\epsilon - \epsilon_0)}{\epsilon/\epsilon_0 + 2}\boldsymbol{E_0}$·. As a result of the superposition of outside fields, there will be field enhancement near the sphere surface in the direction of polarization. To further show the effect of shape curvature, the sphere can be elongated into a spheroid, which has been theoretically studied by many researchers (Calander and Willander, 2002; Jersch, et al., 1998). This prolate spheroid resides in a uniform external electric field E_0, polarized along the major axis. With the electrostatic approximation, the field distribution can be analytically calculated. The electric field E_{loc} at the bottom tip of the spheroid is (Ermushev, et al., 1993)

$$E_{loc} = \frac{\varepsilon E_0}{1 + (\varepsilon - 1) \cdot A}, \tag{3.3}$$

where $A = 1 - \xi Q_1'(\xi)/Q_1(\xi)$ and $\xi = a/(a^2 - b^2)^{1/2}$, a is the semi-major axis, b is the semi-minor axis $(a, b \ll \lambda)$. Q_1 and Q_1' are the Legendre function of the second kind and its derivative. From above equations, the field enhancement, which is characterized by E_{loc}/E_0, is determined by two factors, the dielectric function of the spheroid and the ellipsoid depolarization factor A. It is noticed that A is only a geometrical factor, decided by the axis ratio a/b of the spheroid. When the ratio a/b goes up, meaning a higher curvature at ends of spheroid, the factor A tends to be smaller and the field enhancement

will be higher. This confirms that the lightning rod effect contributes to the field enhancement.

3.1.2   Optical Antenna Effect

Analogous to antenna for radio or microwave frequency, the optical antenna enables the transformation between propagating electromagnetic waves and localized fields. While the length of a simple radio antenna is optimized to achieve high efficiency, the same cannot be done for optical antenna at visible frequencies, simply because there is no good conductor for light in this frequency range. Many efforts have been spent to investigate the optical antenna formed by the NSOM tip apex. Using the prolate spheroid as an approximation of NSOM tip, the optical antenna effect in field enhancement of a sharp tip was evaluated based on electrodynamics calculation (Wokaun, 1985; Calander and Willander, 2002).As a result, a contribution from global antenna effect to the enhancement of field near tip apex was concluded, which depends on the spheroid's axis ratio, wavelength of illumination, direction of incident optical excitation and polarization. etc (Calander and Willander, 2002). The lightning rod effect is also mentioned in their result, which it's recognized as a local effect, because it only affects the region of high curvature.

3.1.3   Localized Surface Plasmon Resonance

For some metal tips working with visible wavelengths, the major field enhancement factor could be plasmon resonance. Different than antenna effect, plasmon resonance results from a collective oscillation of electrons. This can be seen from the spheroid

model in section 3.1.1. For a fixed factor A, Equation (3.3) shows the field enhancement will diverge with certain dielectric function ε. This means the stimulated oscillation of electrons has little damping, leading to the excitation of local surface plasmon. While the plasmon resonance greatly enhances the field near tip apex, it should also be noticed that, the resonance depends strongly on the shape of the tip and the tip-sample interaction, which complicates the interpretation of experiment results.

3.2   Theoretical Models for Tip Sample Interaction

The field confinement and enhancement near tip apex assure s-NSOM's ability to achieve high resolution and reasonable signal level. Further than that, the image formation process still needs to be understood to draw conclusions from the measured results. While many numerical simulations have been carried out, an analytical model will help to understand the contrast mechanism and the origin of signals. Since the complex shape of s-NSOM probe makes it impossible to obtain an analytical result, the problem has to be simplified. Considering the conical or pyramidal shape of s-NSOM probe and the nature of near field interaction, the interacting tip apex may be modeled by its similarities like a sphere or spheroid. The probe shaft has less effect on near field interaction and is usually neglected to simplify the problem. With these considerations, a commonly used dipole model and a revised description of the tip-sample interaction are introduced in this section.

3.2.1   Dipole Model of Tip-Sample Interaction

The dipole model for s-NSOM tip-sample interaction comes from an early work of surface enhanced spectroscopy (Aravind and Metiu, 1983). When the tip is much smaller than the wavelength, the optical interaction between tip and sample could be solved analytically. Based on the proposed solution, the tip response under illumination of different polarized light sources was calculated (Knoll and Keilmann, 2000). In their calculation, the s-NSOM probe is represented by a polarizable sphere with a radius a. The sample is a half space plane with a complex dielectric constant ε. It could be either dielectric or metallic. The sphere is at a distance of $z = r - a$ above the sample surface. The applied electric field could be either parallel to the axis of probe shaft or perpendicular to it (Figure 3.1).
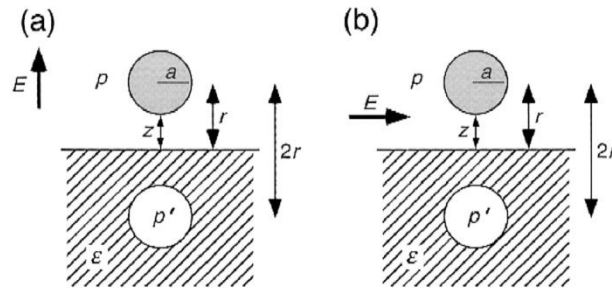
Figure 3.1. Dipole model for tip sample interaction with the applied electric field in (a) parallel or (b) perpendicular arrangement (Knoll and Keilmann, 2000).

When the electric field is applied in parallel direction, the sphere will be polarized in the same direction as the electric field. The dipole moment and the electric field distribution of the tip dipole can be calculated as (Knoll and Keilmann, 2000)

$$p = \alpha E \tag{3.4}$$

$$E_{dipole}(r) = \frac{p}{2\pi r^3},$$

(3.5)

where $\alpha = 4\pi a^3 (\varepsilon_p - 1)/(\varepsilon_p + 2)$ describes the polarizability of a dielectric sphere with a complex dielectric constant ε_p, residence in vacuum (or air) and subjecting to a uniform electric field E. The field distribution of this tip dipole will induce surface charges in the sample, which can be described by an image dipole. The dipole moment of this image dipole is $p' = \beta p$, where $\beta = (\varepsilon_s - 1)/(\varepsilon_s + 1)$ is the "reflection coefficient", with ε_s is the dielectric constant of the sample. The image dipole locates at a distance $2r$ from the probe dipole. The field distribution E' of this image dipole also interacts with the tip dipole, however, only the first reflection is considered here. By neglecting the phase difference between two dipoles, the actual tip dipole moment can be calculated as (Knoll and Keilmann, 2000)

$$p = \alpha E + \alpha E' = \alpha E + \frac{\alpha \beta p}{2\pi (2r)^3}$$

(3.6)

$$p = \frac{\alpha(1 + \beta)}{1 - \frac{\alpha \beta}{16\pi r^3}} E.$$

(3.7)

Thus the effective polarizability for the tip-sample coupled system will be

$$\alpha_{eff,\parallel} = \frac{E}{p} = \frac{\alpha}{1 - \frac{\alpha \beta}{16\pi r^3}}.$$

(3.8)

For the situation of applied electric field in the perpendicular direction, the effective polarizability of tip sample coupled system is calculated to be

$$\alpha_{eff,\perp} = \frac{\alpha(1 - \beta)}{1 - \frac{\alpha \beta}{32\pi r^3}}.$$

(3.9)

This simplified dipole model has its importance in several aspects. In s-NSOM, the excitation laser induced oscillating dipole moment will radiate electromagnetic waves into space, forming an approximately spherical wave front. The field strength detected at the far field thus relates directly to the near field dipole moment, and is proportional to the effective polarizability. As a result, the contrast of optical image can be interpreted as the difference in effective polarizability according to this model.

With this consideration, Equation (3.8) can be used to estimate the near field interaction between tip and sample. An example is calculated for the case of a gold tip over a gold planar surface. The wavelength of excitation laser is 633 nm, and the dielectric constant for gold at this wavelength is $\varepsilon = -11.8 + 1.24i$. Assuming a tip radius of 10 nm, the relation of field strength (magnitude of effective polarizability) versus gap distance between the polarizable sphere and sample surface is shown in Figure 3.2, which can be considered as an approach curve from the AFM point of view. This approach curve shows a huge increase when the tip is very close to the surface, in the range of about tip radius. For larger tip sample distance, the magnitude decays to a small value and remains nearly constant. This nonlinear distance dependence justifies the commonly used modulation technique in s-NSOM, which is oscillating tip sinusoidally with amplitude comparable to tip radius. This nonlinearity in the curve indicates the near field signal will be available at high harmonics of the tip oscillation frequency Ω (Figure 3.3), while the near constant background contains a much weaker response at these frequencies. With a lock-in amplifier, signals at higher harmonic frequencies $n\Omega$ (n>1) can be collected, resulting a detection of the near field information, with the background being suppressed (Knoll and Keilmann, 2000).

The dipole model analytically describes the near field interaction, providing some useful guidance for experimental observations. It qualitatively predicts the nonlinear relation with tip sample gap size, the contrast mechanism of optical signals, and a resonance effect. However, with ignoring the long AFM probe shaft, the large background scattering presented in real measurement has been overlooked. When the gap between tip and sample becomes very small, the charge distribution in the sphere needs to be taken into consideration. Besides, it is shown that the dipole model fails to predict the correct spectral position of resonance, and the contrast predicted is hardly quantitative (Cvitkovic, et al., 2007).
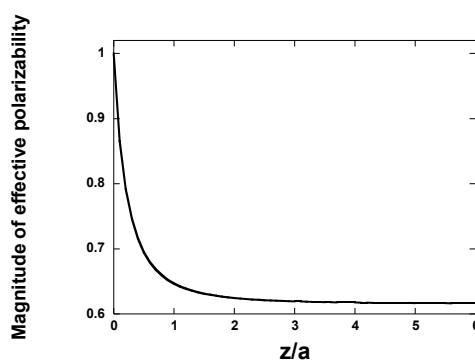
Figure 3.2. Theoretical calculation of approach curve of Au sphere over Au substrate, based on Equation (3.9).
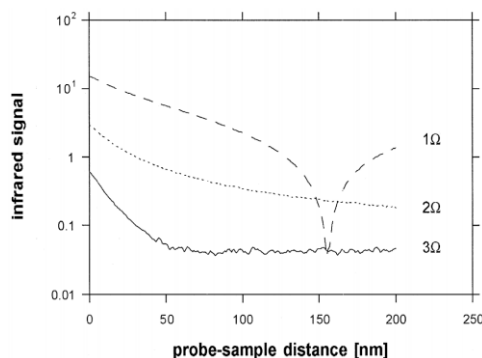
Figure 3.3. Experimental approve curves of infrared signal on Si sample, at tip oscillation frequency Ω, 2Ω and 3Ω harmonics (Knoll and Keilmann, 2000).

3.2.2   Monopole Model of Tip Sample Interaction

The discrepancies between the dipole model and experiment results have motivated further consideration of the dipole model. A monopole model to overcome some of the limitations was proposed and justified with experiments in the infrared wavelength (Cvitkovic, Ocelic, and Hillenbrand, 2007). In the proposed monopole model, the s-NSOM probe is represented by an isolated spheroid, which is still analytically solvable. The monopole model is quite similar to the point dipole model. It first considers the field distribution of spheroid inside a uniform electric field. Then, with the presence of a planar sample, the near field interaction between tip and sample is included. By using equivalence charges, the near field interaction is described by a few point charges locating inside the spheroid. In the end, it is concluded that a few parameters are enough to quantitatively predict the near field interaction. These parameters can either be obtained experimentally or fitted from experimental data and subsequently used for all data. The derivation of this monopole model is included below (Cvitkovic, Ocelic, and Hillenbrand, 2007).

The s-NSOM probe is modeled with a spheroid with length below $\lambda/4$, to neglect the dephasing effects of reducing the enhancement magnitude (Martin, Hamann, and Wickramasinghe, 2001). Assuming it is a perfect conducting spheroid, in electrostatic case, the field outside the spheroid will be a superposition of applied field E_0 and field generated by the spheroid. It is too complex to give an analytical solution for the near field interaction. To simplify the near field distribution of a spheroid, three possible approximations were proposed. As shown in Figure 3.4, E_s (dashed line) shows the exact solution of field distribution. E_{cd} is the near field distribution of a point dipole at the

center of the spheroid. E_m is the near field distribution of a monopole at the center of spheroid apex. In the end, E_{pd} is the near field distribution of a dipole located at the center of spheroid apex. By observing the curves, the field of monopole shows a close agreement with the exact solution. Thus, the near field of spheroid apex can be approximated by a monopole (Cvitkovic, Ocelic, and Hillenbrand, 2007).
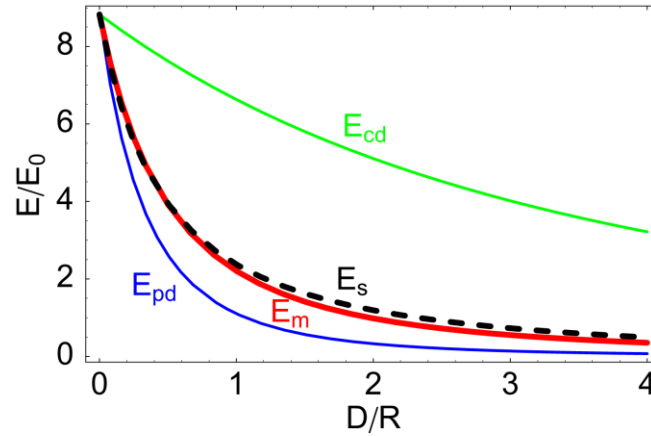
Figure 3.4 Electric field distribution of spheroid along major axis. The exact solution E_s (dashed line) and its three approximations E_{cd}, E_m, E_{pd} (Cvitkovic, Ocelic, and Hillenbrand, 2007).

Assuming the monopole charge is Q_0, similar to the dipole model, the charges on sample surface can be represented by a mirror charge $Q_0' = -\beta Q_0$, where β is the reflection factor defined before. This mirror charge will further polarize the spheroid. For simplification, this effect is studied by only considering a point charge Q_e locating outside spheroid. If the spheroid is grounded, the induced charge on the spheroid will be (Cvitkovic, Ocelic, and Hillenbrand 2007)

$$Q_t = -Q_e \frac{ln\frac{L-F+D}{L+F+D}}{ln\frac{L+F}{L-F}}. \tag{3.4}$$

For a grounded, perfect conduction spheroid, the Q_t can be equivalent by a straight line charge distribution between two spheroid foci. The expression for this line charge distribution is (Cvitkovic, Ocelic, and Hillenbrand, 2007)

$$q_i(z) = -\frac{Q_e\Theta(F^2 - z^2)}{2F}\sum_{n=0}^{\infty}(2n+1)\frac{Q_n\left(\frac{L+D}{F}\right)P_n\left(\frac{L}{F}\right)}{Q_n\left(\frac{L}{F}\right)}P_n\left(\frac{L}{F}\right), \tag{3.5}$$

the Θ is unit step function, Q_n is the nth Legendre functions of second kind, and P_n is the Legendre polynomials.
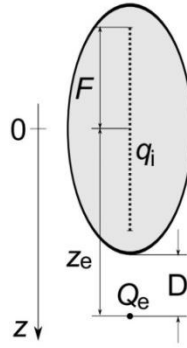
Figure 3.5 The induced charges for a grounded spheroid in presence of an external charge Q_e equivalent to a line charge distribution (Cvitkovic, Ocelic, and Hillenbrand, 2007).

Again, for simplicity, the line charge distribution can be replaced by an effective point charge Q_i. Since the line charge density has it maximum near spheroid focus, and it is the spheroid apex mostly involved in the near field interaction, the effective charge Q_i is assumed at the focus $z = F = R/2$ ($R \ll L$). The value of Q_i is considered to be equal to the total charges along the line between $z = L$ and $z = L - (R + D)$ (Cvitkovic, Ocelic, and Hillenbrand, 2007).

$$Q_i = gQ_t = \int_{L-(R+D)}^{L} q_i(z)dz \tag{3.6}$$

The fraction g represents how many charges of the total induced charges should be taken into account for the effective charge. By varying the parameter R/L, it shows that g is generally about 0.7 ± 0.1. This is the case for a grounded perfect conducting spheroid. For an isolated spheroid, the negative charges cannot flow out of the spheroid. The negative charges will be assumed to be uniformly distributed along the z direction of the spheroid, thus for a slice of thickness Δz, the contained charges are $\Delta Q = -Q_t \Delta z / (2L)$. Since the charge distribution changes, the fraction g has to be modified (Cvitkovic, Ocelic, and Hillenbrand, 2007).

$$Q_0 = g'Q_t = \left(g - \frac{R+D}{2L}\right)Q_t \tag{3.7}$$

With above consideration, for an isolated spheroid above a planar sample, illuminated by an external field E_0, the near field interaction induced charges Q_i should include two major components: the charges $Q_{i,0}$ induced by mirror charge Q_0' and the charges $Q_{i,1}$ induced by mirror charge Q_i' of Q_i, as shown below (Cvitkovic, Ocelic, and Hillenbrand, 2007).
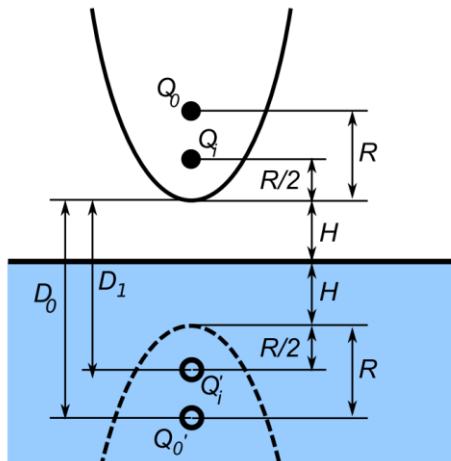
Figure 3.6 Charges involved in the tip sample near field interaction, including their positions (Cvitkovic, Ocelic, and Hillenbrand, 2007).

$$Q_i = Q_{i,0} + Q_{i,1} \tag{3.8}$$

$$Q_{i,0} = f_0 Q_0' = -\left(g - \frac{R+H}{L}\right) \frac{\ln\frac{4L}{4H+3R}}{\ln\frac{4L}{H}} Q_0' \tag{3.9}$$

$$Q_{i,1} = f_1 Q_1' = -\left(g - \frac{3R+4H}{4L}\right) \frac{\ln\frac{2L}{2H+R}}{\ln\frac{4L}{H}} Q_i' \tag{3.10}$$

From above equations, a "near field contrast factor" can be defined (Cvitkovic, Ocelic, and Hillenbrand, 2007),

$$\eta = \frac{Q_i}{Q_0} = \frac{\beta\left(g - \frac{R+H}{L}\right)\ln\frac{4L}{4H+3R}}{\ln\frac{4L}{H} - \beta\left(g - \frac{3R+4H}{4L}\right)\ln\frac{2L}{2H+R}}. \tag{3.17}$$

The effective dipole moment can be considered as two parts. The first part is dipole moment $p_0 = 2Q_0 L$ due to external illumination field. The second part is dipole moment p_i resulting from near field interaction. The value of $p_i = Q_i L = \eta Q_0 L$ can be derived easily, considering its negative charge $-Q_i$ locating at the spheroid center to preserve the equipotential of the spheroid. The value of the effective dipole moment is $p_{eff} = p_0 + p_i$. By definition, the effective polarizability is (Cvitkovic, Ocelic, and Hillenbrand, 2007)

$$\alpha_{eff} = \frac{p_{eff}}{E_0} = R^2 L \frac{\frac{2L}{R} + \ln\frac{R}{4eL}}{\ln\frac{4L}{e^2}}$$

$$\cdot \left(2 + \frac{\beta\left(g - \frac{R+H}{L}\right)\ln\frac{4L}{4H+3R}}{\ln\frac{4L}{H} - \beta\left(g - \frac{3R+4H}{4L}\right)\ln\frac{2L}{2H+R}}\right). \tag{3.18}$$

Finally taking into account the reflection of the illumination field from sample surface, the scattered field can be described as (Cvitkovic, Ocelic, and Hillenbrand, 2007)

$$E_{sca} \propto \left(1 + r_p\right)^2 \alpha_{eff} E_{inc}, \tag{3.19}$$

where r_p is the Fresnel reflection coefficient for p polarized light.

Cvitkovic further compared the monopole model quantitively with s-NSOM results at infrared wavelength (Cvitkovic, Ocelic, and Hillenbrand, 2007). An approach curve on gold surface and a spectral response of SiC sample were collected and compared with the predictions from different models. Great agreement has been achieved with the monopole model, as shown in Figure 3.7. The monopole model provides more insights in the understanding of the tip-sample interaction. It shows that the shape of the tip and its shaft also play an important role in the detected signal.
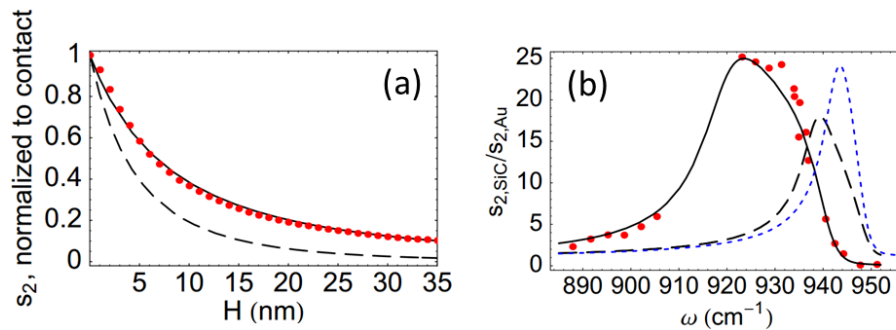
Figure 3.7 Experiment results (dots) compare with prediction from monopole model (full line) and dipole model (dashed line). (a) Approach curve on gold surface. (b) Near field spectra of SiC crystal (Cvitkovic, et al., 2007).

3.3   Near Field Signal Detection Techniques

Along with all the advantages of s-NSOM, there's a major difficulty in detecting the pure near field signal. It is the large elastic scattering background from the reflections of probe shaft and sample surface. This background provides no information on the near field interaction; however, it dominates the radiation reaching the detector. Considerable effects have been devoted to suppressing this undesired background in the development

of s-NSOM. Modulating the tip sample gap and demodulation at higher harmonics have eliminated background to a certain extent. However, this method alone is insufficient to suppress background, especially in the visible range (Gucciardi, et al., 2008). Different interferometric detection schemes have been proposed to extract the pure near field interaction, known as homodyne method, heterodyne method, and pseudo-heterodyne method. In the following sections, the fundamental mechanisms of these techniques have been explained and compared, with a focus on the pseudo-heterodyne detection, which is applied to the work in this thesis. The mathematical derivations below is mostly adapted from (Ocelic, Huber, and Hillenbrand, 2006; Ocelic, 2007), which is the first s-NSOM implementation of the pseudo-heterodyne method.

3.3.1   Noninterferometric Detection

The total scattered field E_S in s-NSOM can be expressed as $E_S = E_N + E_B$, where E_N represents the near field scattering, E_B represents the background scattering. With an illumination field of E_0, the tip dithering at a frequency of Ω will modulate the scattered fields periodically. Thus the fields can be written in the form of Fourier series (Ocelic, Huber, and Hillenbrand, 2006),

$$E_N(t) = \sum_{n=-\infty}^{\infty} e^{in\Omega t} E_{N,n} = E_0 \sum_{n=-\infty}^{\infty} e^{in\Omega t} \sigma_{N,n} \tag{3.20}$$

$$E_B(t) = \sum_{n=-\infty}^{\infty} e^{in\Omega t} E_{B,n} = E_0 \sum_{n=-\infty}^{\infty} e^{in\Omega t} \sigma_{B,n}, \tag{3.21}$$

with the scattering coefficient $\sigma_{N,n} = E_{N,n}/E_0$ and $\sigma_{B,n} = E_{B,n}/E_0$. The output of the detector is usually a voltage proportional to the current generated by the light radiation.

Assuming the electric field at te detector is E_D, the voltage output is a measure of light intensity $I \propto |E_D|^2$. For noninterferometric measurement, the field E_D equals to the total scattered field E_S as

$$E_D = E_N + E_B = E_S = E_0 \sum_{n=-\infty}^{\infty} e^{in\Omega t}(\sigma_{N,n} + \sigma_{B,n}). \qquad (3.22)$$

The output voltage is proportional to light intensity, $u \propto |E_D|^2$. As the same result of the tip modulation, the output voltage can be expanded in Fourier series (Ocelic, Huber, and Hillenbrand, 2006),

$$u = \sum_{n=-\infty}^{\infty} e^{in\Omega t}u_n = k \left| \sum_{m=-\infty}^{\infty} e^{im\Omega t}(\sigma_{N,m} + \sigma_{B,m}) \right|^2. \qquad (3.23)$$

where k is a proportional constant. From the above equation, the expansion coefficient of detector response will be $(l = m - n)$ (Ocelic, Huber, and Hillenbrand, 2006)

$$u_n = k \sum_{m=-\infty}^{\infty} (\sigma_{N,m}\sigma_{N,l}^* + \sigma_{N,m}\sigma_{B,l}^* + \sigma_{B,m}\sigma_{B,l}^* + \sigma_{B,m}\sigma_{N,l}^*). \qquad (3.24)$$

The effective polarizability could be written as a complex number, $\sigma_{N,n} = s_n e^{i\varphi_n}$ and $\sigma_{B,n} = b_n e^{i\psi_n}$. Besides, the background term $\sigma_{B,0}$ is much larger than any other terms in Equation (3.24), all other terms can be neglected as an approximation, leading to

$$u_n = 2kb_0[b_n cos(\psi_n - \psi_0) + s_n cos(\varphi_n - \psi_0)]. \qquad (3.211)$$

With higher harmonic demodulation, the background term b_n is much smaller than the near field term s_n, thus the following conclusion is obtained (Ocelic, Huber, and Hillenbrand, 2006):

$$u_n = 2kb_0 s_n cos(\varphi_n - \psi_0). \qquad (3.26)$$

From the above equation, the limitation of the non-interferometric detection is obvious. The background term b_0 is always included in the demodulated signal, no matter how high the demodulation order is. This confirms that the pure near field interaction cannot be extracted with high harmonic demodulation alone.

3.3.2   Homodyne Detection

The homodyne detection is fundamentally the same with non-interferometric detection. An external reference $E_R = E_0 r_R e^{i\psi_R}$ is applied by the reflection from a stationary mirror. The interferences happen between the near field scattering, the background scattering and the reference beam. Following the same derivation method in section 3.3.1, considering the reference beam is a constant term, the coefficient now is

$$u_n = 2k s_n [b_0 \cos(\varphi_n - \psi_0) + r_R \cos(\varphi_n - \psi_R)]. \tag{3.27}$$

With a much stronger reference beam, the back scattering induced term can be neglected, reducing to (Ocelic, Huber, and Hillenbrand, 2006)

$$u_n = 2k s_n r_R \cos(\varphi_n - \psi_R). \tag{3.28}$$
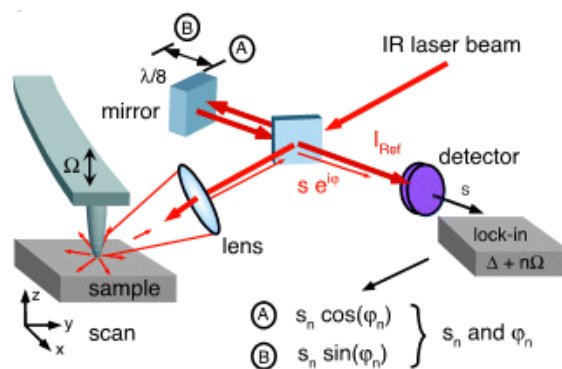
Figure 3.8. A common homodyne detection configuration (Taubner, et al., 2003).

For homodyne detection, a repeat measurement is usually conducted with a change in position of $\lambda/8$ of the reference mirror. This leads to a change of 90 degrees in the phase of the reference beam, producing a second result (Taubner, Hillenbrand, and Keilmann, 2003)

$$w_n = 2ks_nr_R\sin(\varphi_n - \psi_R). \tag{3.29}$$

Combining Equation (3.28) and (3.29), the near field amplitude and phase can be obtained. The idea of homodyne detection is quite straight forward. By replacing the unknown background scattering with a controllable reference beam, the affection of background artifacts can be reduced. This implementation relies on the approximation of background scattering is negligible to the reference. This puts some requirement on the illumination laser power. The reference mirror also needs to be shifted between two stationary positions, which results some inaccuracy in the results.

3.3.3   Heterodyne Detection

A standard configuration for heterodyne detection is shown in Figure 3.9 (Taubner, Hillenbrand, and Keilmann, 2003). The excitation laser goes through an acousto-optic modulator (AOM). A second beam with frequency shifted by Δ will come out the AOM at a deviated angle. Δ is usually 100 MHz for a typical AOM. The second beam $E_R = E_0r_Re^{i\Delta t+i\psi_T}$ will be used as reference to interfere with the modulated near field signal. By demodulating detector output at $\Delta \pm n\Omega$, the signal can only come from interference from reference wave and near field scattering (Taubner, Hillenbrand, and Keilmann, 2003).

$$u = k \left| \sum_{m=-\infty}^{\infty} e^{im\Omega t} \sigma_{N,m} + r_R e^{i\Delta t + i\psi_T} \right|^2 \tag{3.30}$$

$$u_{\Delta+n\Omega} = k s_n r_R e^{i(\psi_T + \varphi_n)}, \tag{3.31}$$

where ψ_T is phase delay between dithering tip and its driving signal. By demodulation at a sideband, the heterodyne method can achieve the highest background suppression among all other methods, producing the most reliable near field images. However, there're some practical limits in implementation of the heterodyne detection. Firstly, the derivation beam at a small angle limits the compactness of the setup. The range of AOM also limits spectra measurements of tip enhanced phenomena. For infrared measurement, the use of a visible guiding light will also be impossible.
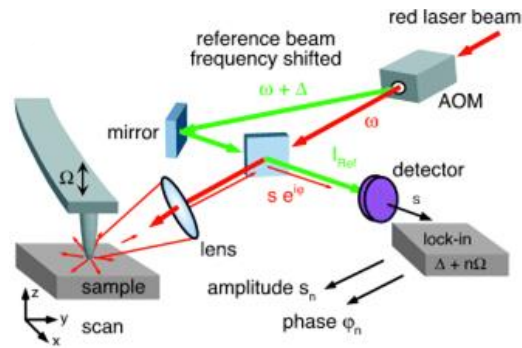
Figure 3.9. A common configuration for heterodyne detection (Taubner, et al., 2003).

3.3.4 Pseudo-heterodyne Detection

The pseudo-heterodyne detection method was proposed as an alternative to the heterodyne one, avoiding the mentioned practical difficulties (Ocelic, Huber, and Hillenbrand, 2006). A standard configuration of this method is shown in Figure 3.10. This setup is essentially a Michelson interferometer. The basic idea is to modulating the

phase of reference wave to interfere with near field scattering, instead of using a reference light of different frequency. A similar derivation is shown below to interpret the process of extracting pure near field signal (Ocelic, Huber, and Hillenbrand, 2006).

The incident beam E_0, after being split at the beamsplitter, is reflected by a mirror to interfere with tip scattered light, serving as a reference beam. The mirror is oscillating sinusoidally, resulting an additional component $\gamma \cos(Mt)$ to the phase of incident beam. In the equation, γ is the maximum possible phase change, is also called the phase modulation amplitude or modulation depth, and M is the reference wave phase modulation frequency. Thus the phase modulated reference wave can be described as (Ocelic, Huber, and Hillenbrand, 2006)

$$E_R = E_0 \rho e^{i\gamma \cos(Mt)}, \tag{3.32}$$

where $\rho = r_R e^{i\psi_R}$ is the reflection coefficient for reference wave, γ is phase modulation amplitude or the modulation depth, M is the reference wave phase modulation frequency, and ψ_R represents the optical path difference between reference and signal. From the knowledge of Jacobi-Anger expansion $e^{iz \cos(\theta)} = \sum_{n=-\infty}^{\infty} i^n J_n(z) e^{in\theta}$. The Fourier series expansion of the reference is

$$E_R = E_0 \sum_{m=-\infty}^{\infty} e^{imMt} \rho_m, \tag{3.33}$$

and the coefficient ρ_m in the expansion is

$$\rho_m = r_R J_m(\gamma) e^{i\Psi_R + \frac{im\pi}{2}}, \tag{3.34}$$

where J_m is the Bessel function of first kind, mth order. Considering the total scattering field $E_S = E_0 \sum_{n=-\infty}^{\infty} e^{in\Omega t} \sigma_{S,n}$, it interferes with the phase modulated reference wave. The voltage output on the detector will be

$$u = k|E_S + E_R|^2 = k \left| \sum_{n=-\infty}^{\infty} e^{in\Omega t} \sigma_{S,n} + \sum_{m=-\infty}^{\infty} e^{imMt} \rho_m \right|^2. \tag{3.35}$$

The detector output will be demodulated by lock-in amplifier at frequency of $f_{n,m} = n\Omega + mM$ ($n > 0, m \neq 0$). The amplitude of detector output at frequency $f_{n,m}$ will be

$$u_{n,m} = k\left(\sigma_{S,n}\rho_m^* + \sigma_{S,n}^*\rho_m\right). \tag{3.36}$$

Substituting ρ_m from Equation (3.34) and writing $\sigma_{S,n}$ as $\sigma_{S,n} = s_{S,n} e^{i\varphi_{S,n}}$, the following result is obtained (Ocelic, Huber, and Hillenbrand, 2006):

$$u_{n,m} = 2k s_{S,n} r_R J_m(\gamma) \cos\left(\varphi_{S,n} - \psi_R - \frac{m\pi}{2}\right). \tag{3.37}$$

Due to the existence of $\frac{m\pi}{2}$ term in Equation (3.37), the sideband of $n\Omega$ will be proportional to either the cosine part of the scattering coefficient $\sigma_{S,n}$ for even m, or the sine part for odd m, like

$$u_{n,m} = \begin{cases} 2k s_{S,n} r_R J_m(\gamma) \cos\left(\varphi_{S,n} - \psi_R\right), & m \text{ is even} \\ 2k s_{S,n} r_R J_m(\gamma) \sin\left(\varphi_{S,n} - \psi_R\right), & m \text{ is odd} \end{cases}. \tag{3.38}$$

As a result, a combination of signals at two adjacent sidebands will be able to give the complex scattering coefficient (Ocelic, Huber, and Hillenbrand, 2006)

$$\sigma_{S,n} = s_{S,n} e^{i\varphi_{S,n}} = k_0 \left[\frac{u_{n,j}}{J_j(\gamma)} + i\frac{u_{n,l}}{J_l(\gamma)} \right], \tag{3.39}$$

with $k_0 = \exp(i\psi_R) / 2k r_R$, j and l are even and odd integer respectively. For $j=1$ and $l=2$, with a suitable modulation depth $\gamma = 2.63$, the Bessel functions $J_1(\gamma)$ and $J_2(\gamma)$ equal to

each other. Thus, the scattering coefficient can be further simplified to (Ocelic, Huber, and Hillenbrand, 2006)

$$\sigma_{S,n} = \frac{k_0}{J_1(\gamma)}\left[u_{n,j} + iu_{n,l}\right] \tag{3.40}$$

$$\Delta l = \frac{1}{2}\frac{\gamma\lambda}{2\pi}. \tag{3.41}$$

The proportional constant in Equation (3.40) is not critical for contrast measurement. With the modulation depth $\gamma = 2.63$, the reference mirror is vibrating with an amplitude Δl (Equation (3.41), round travel of reference arm). Using the high harmonic technique, the background scattering term $\sigma_{B,n}$ can be neglected, thus $\sigma_{S,n} = \sigma_{N,n} + \sigma_{B,n} \approx \sigma_{N,n} = s_n e^{i\varphi_n}$. In this case, the near field amplitude s_n and phase φ_n can be directly calculated from the two measured sidebands, shown in Equation (3.38), where K is just a proportional constant (Ocelic, Huber, and Hillenbrand, 2006).

$$s_n = K\sqrt{u_{n,j}{}^2 + u_{n,l}{}^2} \tag{3.42}$$

$$\varphi_n = Arg(u_{n,j} + iu_{n,l}) \tag{3.43}$$
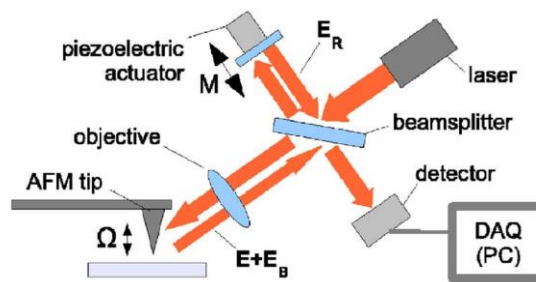
Figure 3.10. A standard configuration for pseudo-heterodyne detection (Ocelic, et al., 2006).

3.4   <u>Conclusion</u>

In conclusion, the working principle of s-NSOM is introduced. The determining factors of resolution in s-NSOM are discussed. The derivation of analytical models describing the optical near field interaction between tip and sample is presented. It is shown although the models have limits in describing measurement results quantitatively, they predict the near field behaviors very well. After that, the issue of background noises in implementing apertureless NSOM is addressed. Different detection schemes are presented and their operations are validated by detailed mathematical derivation. Among several proposed detection techniques, the heterodyne and pseudo-heterodyne detection schemes provide the ability to measure both the near field amplitude and phase simultaneously, while pseudo-heterodyne method provides more flexibility in the experimental setup and possible applications of spectral measurement.

CHAPTER 4. INSTRUMENTATION OF S-NSOM

The theoretical foundation presented in previous chapter provides a solid base for the implementation of s-NSOM. The dipole and monopole model shows the need for tip sample distance modulation and high harmonic demodulation. The heterodyne or pseudo-heterodyne methods provide the final solution to discriminate pure near field signal from the overwhelming background. In this chapter, a scattering type NSOM instrument based on pseudo-heterodyne scheme is built for the visible wavelength range. The characteristics of the built s-NSOM and some experiment results are shown in the following sections.

4.1   The Mechanical Setup

The pseudo-heterodyne scheme is applied in this work. An added benefit of pseudo-heterodyne setup is that noninterferomectric or homodyne measurement can be conducted with minimum modification. The s-NSOM setup is based on a commercial atomic force microscope (CombiScope, AIST-NT). The main advantage of this AFM, besides providing all standard operation modes, is that it can easily integrate optical components. To be exact, this AFM provides simultaneously optical access with objectives from side and bottom. This enables us to employ s-NSOM with either the back scattering mode or the transmission mode. Another advantage is its use of 1300 nm laser for light lever

feedback. This avoids any unnecessary excitation of sample and possible interference with measured signal.

The excitation source is a frequency stabilized 633 nm Helium-Neon Laser. The stable source facilitates the interference between back scattered light and reference beam and minimizes the instability of interference pattern. This setup is essentially a Michelson interferometer or its variation the Twyman-Green interferometer, with the optical path illuminating tip being the measurement arm, and the other optical path being the reference arm. To form a uniform bright or dark interference, the light paths must overlap very well with each other. This overlapping requirement raises an issue of some reflection light returning back to the laser cavity, disturbing the stability of the laser source. To prevent this, an optical isolator is mounted right after the laser exit. The laser beam is then expanded and collimated with a Keplerian type beam expander. The beam expander expands the diameter of the laser beam by a factor of 5, forming a 5 mm diameter collimated beam. This diameter matches with objective rear entrance, utilizing the best focus ability of the objective. To provide the flexibility of exciting the tip with different polarization, a half waveplate is placed after the beam expander. After that, the laser beam is split at a cube beamsplitter. One beam goes to the measurement arm (excitation beam), while the other beam is used as reference. The excitation beam goes through a periscope and is then directed into vertical plane, being able to illuminate the tip from side. A super long working distance objective with 0.42 numerical aperture (NA) is used to focus the collimation beam onto the tip apex. This objective is mounted on a three-axis piezo scanner, which is used for fine alignment of the focused laser spot. Three manual translation stages are used to support the piezo scanner, providing coarse

alignment. The back scattered radiation is collected and collimated by the same objective. In the measurement arm, there is also a flip pellicle beamsplitter, which is used to direct light to the CCD camera for imaging purpose. The reference beam usually goes through a ¼ waveplate and is reflected by a mirror mounted on piezo actuator. The ¼ waveplate combining with a polarizer placed in front of detector provides the ability of selective detection of different electric field components. That is the polarization direction of reference beam at detector position should be consistent with direction of desired electric field component, generally the E_z component. The polarizer in front of detector helps to filter out other field components. The piezo actuator where reference mirror is mounted oscillates sinusoidally, thus modulates the phase of reference beam, enabling the pseudo-heterodyne scheme.
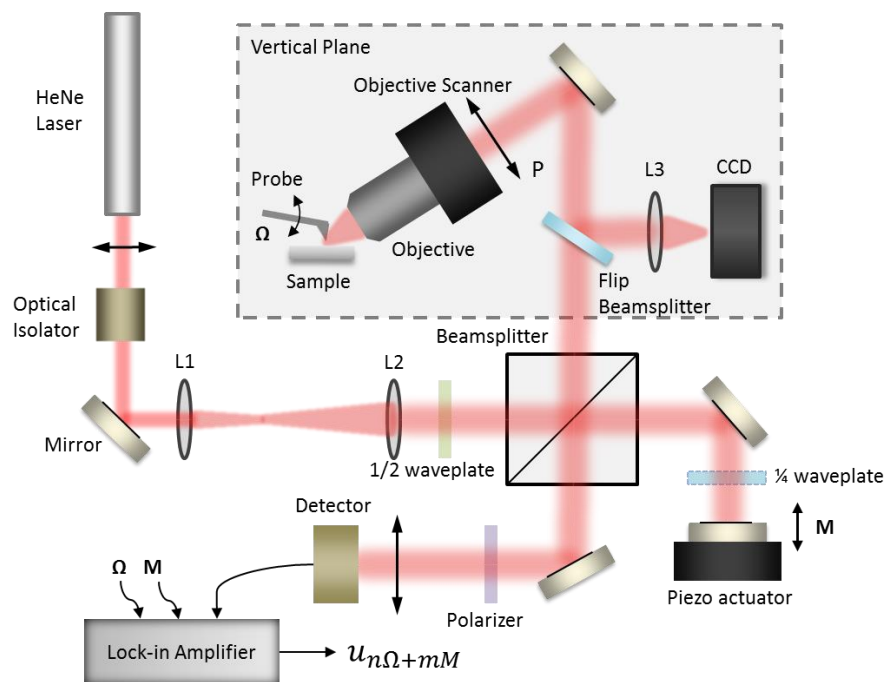
Figure 4.1. Schematic of s-NSOM configuration. A *p* polarization scenario is illustrated, where the direction of illumination polarization is along tip shaft. The ¼ waveplate is not necessary in this case.

The returning back scattered radiation and reference beam meet again at the cube beamsplitter and interfere with each other. The resulting interference is then detected by a photodiode detector. The electric signal from the photodiode detector is then fed to a lock-in amplifier. By using the probe oscillation frequency Ω and the mirror shifting frequency M as reference signals for lock-in amplifier, signals at sidebands of tip oscillation frequency harmonics can be collected. Then pure near field amplitude and phase information can be determined with the help of theoretical knowledge in Chapter 3.
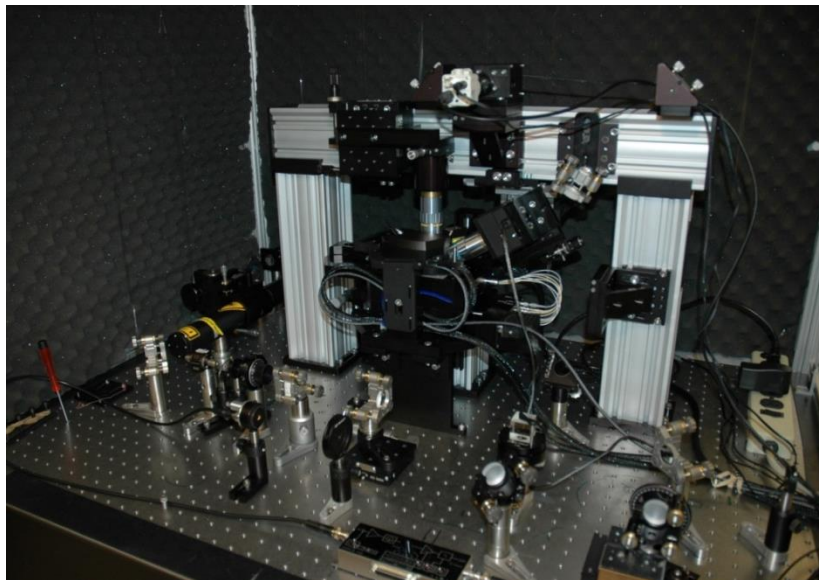
Figure 4.2. A photo showing the overview of the s-NSOM setup.

4.2   Optical Alignment

To succeed in s-NSOM measurement, the key is to achieve best optical alignment. This includes two main aspects. One is to align the interferometer to achieve uniformly bright or dark patterns and maintain its stability. The other one is to position the focused laser spot at the very apex of the tip.

The first important step is the alignment of the interferometer. Achieving zero phase difference at a cross section to generate uniformly bright or dark patterns is very difficult. It relies on many factors, such as stability of mechanical setup and laser source, beam collimation, optical path difference, environmental factors, etc. Because the light scattered back from the tip is weak and not uniform, a mirror is added to the measurement arm for this alignment. The objective is removed temporarily and the mirror is mounted at the same location. By adjusting two mirrors in the measurement arm, the collimated beam can be aligned to be vertical to the mirror and at the center of the mirror. At the same time the returning beam will interfere with the reference beam, forming uniform pattern. The interference contrast can be measured by an optical power meter. Pressing the small optical breadboard will cause the interference pattern varying from total bright to total dark. A contrast measurement better than 15 is usually necessary for the experiment. After that the objective can be mounted back.
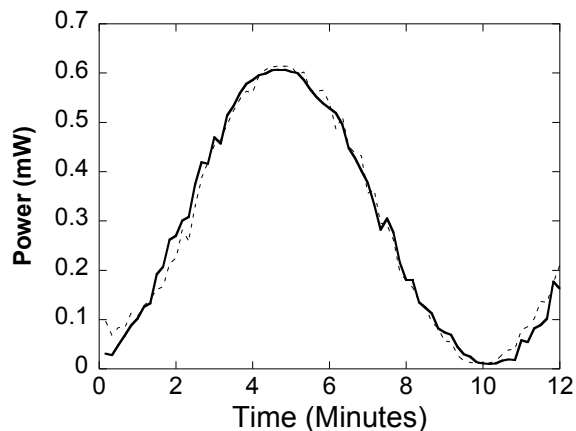
Figure 4.3. The drifting of interference pattern as time passes. Solid and dashed curves show results measured at different time.

Generally the mapping process will take about 20 minutes for this AFM. Thus it is important to have some idea about the stability of interferometer. With the objective replaced by a mirror, the test is an overall estimation of the Michelson interferometer, with many of optical components in its paths. An example result is shown in Figure 4.3. The result shows that the time for the interference pattern changing to totally dark to totally bright is about 5 minutes. Although the stability is not quite satisfying, this slowing varying drifting is considered to be acceptable for the s-NSOM measurement.

By positioning the focused spot precisely at tip apex, the field near tip apex has the best confinement and enhancement. The peak energy intensity will locate in the region of tip sample interaction, leading to a fundamental increase in the signal to noise ratio. The back scattered radiation can be assumed to be a spherical wave. So only when the tip apex is at the focus spot, the back scattered radiation from near field interaction can be collected and collimated to interfere with a reference beam.
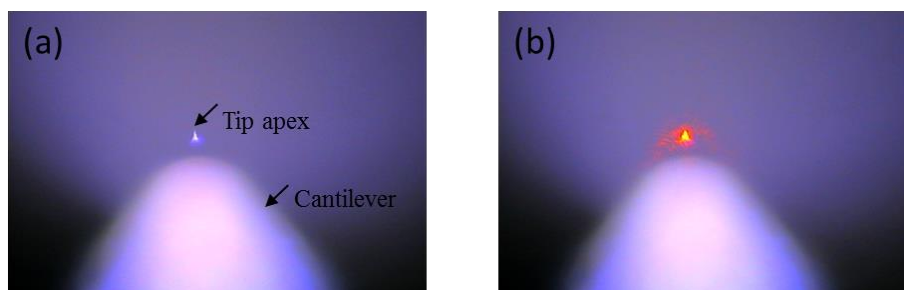
Figure 4.4. Photo images from CCD camera, showing side view of probe tip without (a) and with excitation laser focused onto it (b).

To focus the laser to tip apex, the first thing is to be clear about the movements of tip and sample during approach and scanning. The AFM used here does approach in two steps. Firstly, with the sample fully extended, the whole AFM head including the AFM probe approaches the sample through motor movement. After the probe gets in touch of the

sample, the motor will stop and hold its position. Then the piezo stage supporting sample will respond to finish the approach process, which is called the landing process by the AFM software. Thus, during the process, both the tip and sample change their positions, the final alignment must be done after the approach process finished.
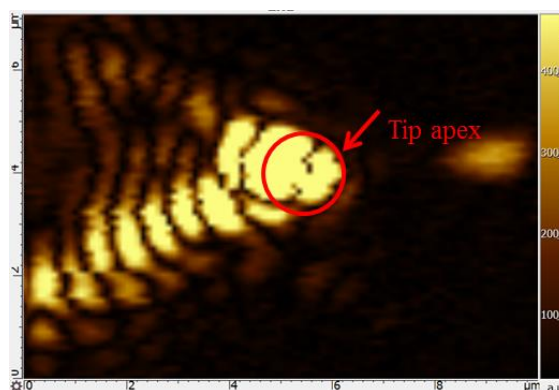
Figure 4.5. An example of the objective scan result. Left side of the image is tip base, right side is tip apex.

Coarse alignment is conducted with the help of the CCD camera. The first step is to land the tip onto the sample to estimate the location laser should be focused to. Then the tip can be retracted to avoid damage and provide more space for coarse alignment. The excitation laser is focused to the marked position on the sample with the help of a 3-axis manual stage. The tip is again approached to the sample by motor. A sample retraction can be done to make sure there's enough separation between tip and sample. The laser spot should be very close to the tip now. By observing the CCD camera image, the laser spot can be adjusted to the tip apex through the movements of the same 3-axis stage and two additional motors controlling the X and Y positions of the AFM head (Figure 4.4). After the laser spot is aligned to tip apex, the landing process can be conducted. The feedback loop will engage to maintain the tip sample distance. For the fine alignment, the objective scanner will be used to move objective to different locations. A map of

variation in scattered intensity will be formed, and the location of tip apex can be determined from this map, as shown in Figure 4.5.

4.3   S-NSOM Measurement of Circular Aperture Array

With this s-NSOM setup, the optical near field distribution of a circular aperture array is investigated. The sample measured is a 75 nm Au film on a microscope slide. The gold film is coated with thermal evaporator. Focused ion beam technology is used to mill the circular aperture array. The diameter of the circular aperture is about 300 nm and the period is 730 nm. Figure 4.6 (a) is the SEM image of the sample showing the edge of the circular aperture array region. The AFM tapping mode operation is applied for the measurement. The probe used is a commercial probe from Nanosensors (probe type ARROW-NCPt). The probe is coated with platinum iridium5 on both sides. The nominal radius of this tip is 25 nm. (Figure 4.6 (b)).

After the process of optical alignment and locating the interested scan area, approach curves are firstly measured. There are generally three different signals interested for approach curves: the tip oscillation amplitude, the phase between tip oscillation and its driving voltage signal, and the optical near field signal. The approach amplitude curve provides a calibration of the real tip oscillation amplitude, which is necessary because the setting in AFM can only give a reference value. The amplitude curve can also help to investigate the affection on signal strength of different oscillation amplitude. The phase curve provides information about the tip working regime (attractive or repulsive). This can be used to determine the gap size between tip and sample, thus helps to understand the near field interaction and evaluate the convolution effects between topographical

signal and optical signal. The optical approach curve is the easiest way to check if near field signal is detected, by observing the exponential decay relation and the signal decay length. In this setup, however, the AFM software is not able to process the measured sidebands to extract pure near field signal in real time. For this practical reason, the optical approach curve is usually measured in homodyne scheme, while some pseudo-heterodyne signals can also be used to show the trend.
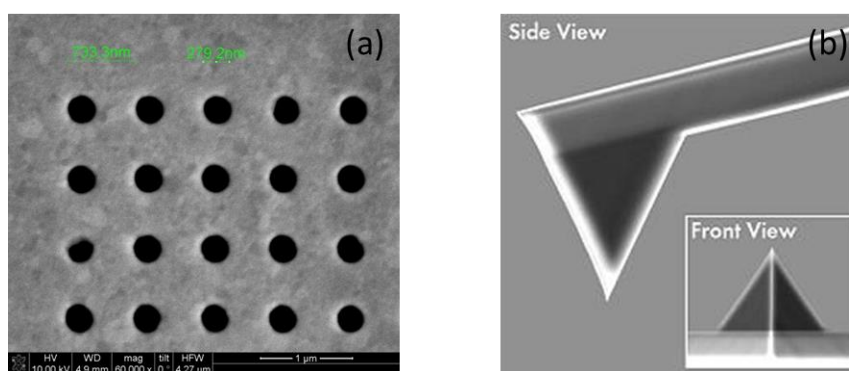
Figure 4.6. SEM images of sample and probe. (a) the edge of circular aperture array region, (b) the ARROW-NCPt AFM probe, with nominal force constant of 42 N/m and resonance frequency of 285 kHz (http://www.nanoandmore.com).

For the measurement, the amplitude and phase approach curves are first obtained to evaluate the measurement conditions. Figure 4.7 shows the measured curves. As the change in oscillation amplitude is equal to the movement of the sample in z direction, the free oscillation amplitude is estimated to be 38 nm while the scanning amplitude is 35 nm. The phase curve shows the phase lag is larger than 90 degrees at the setpoint, which means the tip is working in attractive regime. The knowledge of AFM working conditions will help to understand the results in later near field measurements.
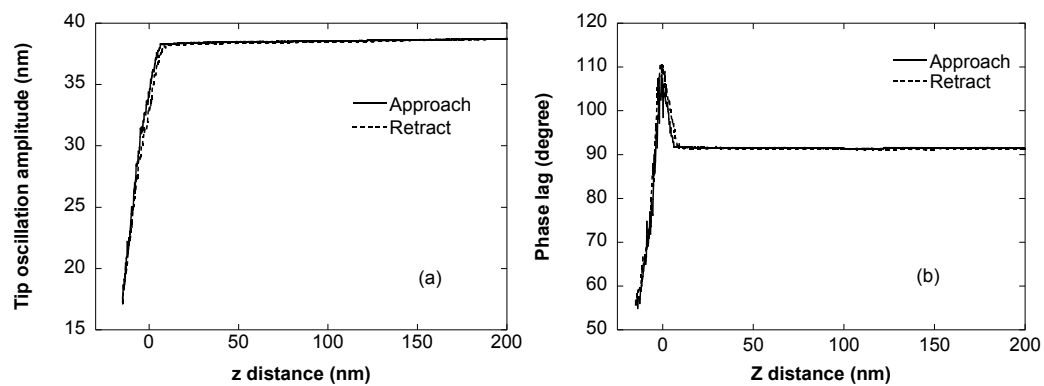
Figure 4.7. The amplitude approach curve (a) and the phase approach curve (b) of the s-NSOM measurement.
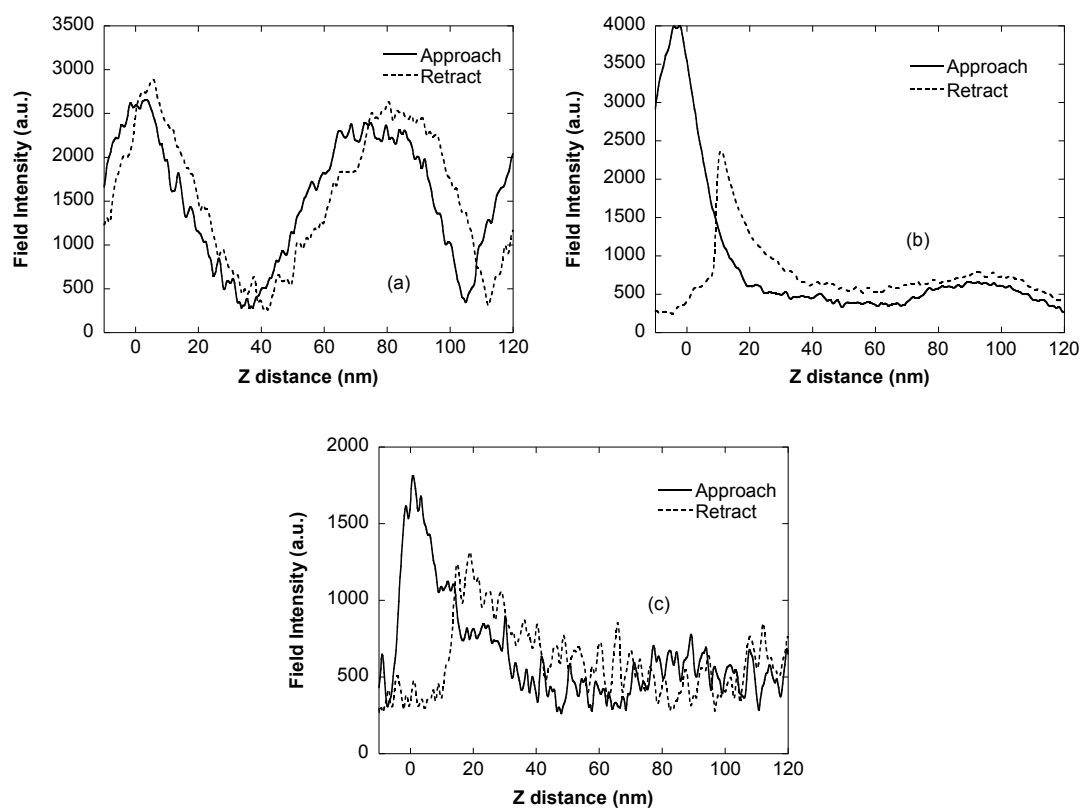
Figure 4.8. Optical approach curves collected with (a) non-reference detection, (b) homodyne detection, and (c) pseudo-heterodyne detection.
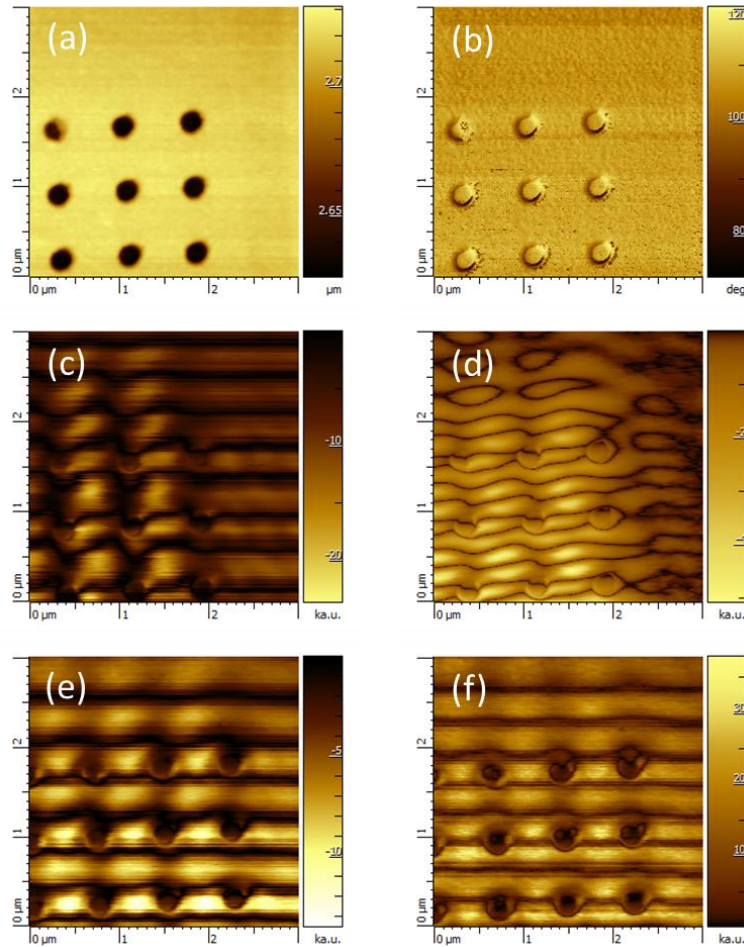
Figure 4.9. The s-NSOM images of the circular aperture array. (a) AFM topography image of the aperture array. (b) AFM phase image. (c) Optical result obtained without reference beam. (d) Optical image obtained by homodyne detection at 2Ω. Optical image obtained by pseudo-heterodyne detection at 2Ω+2M (e) and at 3Ω+1M (f).

To evaluate the optical alignment and confirm the existence of near field signals, the measurement of optical approach curves is carried out. As a benefit of this setup, different detection schemes can be applied without changing any alignment conditions. Thus, for comparison purpose, the optical approach curves are obtained for non-reference measurement, homodyne measurement and pseudo-heterodyne measurement. In this measurement, the tip oscillation frequency is represented by Ω, the reference mirror shifting frequency in pseudo-heterodyne detection is M. The signals are collected at the

third harmonic 3Ω. For pseudo-heterodyne, it's the first sideband of third harmonic 3Ω+1M. These approach curves not only confirm the near field signals can be detected, but also show the successful suppression of background by adding a reference beam.

With the knowledge of AFM working conditions and the presence of near field signal, the near field distribution of the circular aperture array sample is measured. For the pseudo-heterodyne detection, the shifting frequency M of reference is set to 150 Hz due to the low resonance frequency of the piezo actuator. The modulation depth is determined to be 132.5 nm using the modulation depth formula Equation (3.41). The polarization of excitation laser is along the tip shaft direction for higher enhancement of near field signal. For comparison purpose, the signals are collected with different detection schemes.

Figure 4.9 (a) and (b) show the simultaneously measured topography signal and phase signal. Figure 4.9 (c) shows the result of measurement without reference beam. Although this image shows some contrast near apertures, however the near field signal is overwhelmed by backgrounds resulting from reflection between tip and sample. With homodyne measurement Figure 4.9 (d), the background interference is suppressed a little bit, however, the near field signal is still much weaker than backgrounds. Figure 4.9 (e) and (f) show the results for pseudo-heterodyne measurement. (e) is demodulated at 2Ω+2M while (f) is demodulated at 3Ω+1M. Both of them show better suppression of background noise than other measurement methods. It's also noticed that only in (f) that the strength of near field is comparable to the background. This indicates for visible wavelength s-NSOM, the signal should be demodulated at least at the third harmonic. It's also quite obvious that even demodulated at sideband of 3ʳᵈ harmonic, figure (f) still includes a quite strong interference background. This slow varying background is

believed to come from the instability of the interferometer. Besides, the excitation laser is focused to a small spot size, which may not be able to excite a strong field. With this consideration, a new structure is designed for the following section.

4.4   S-NSOM Measurement of Single Slit

To confirm the obtained optical signal is not a result of topographical effect. Another measurement is conducted on a single slit sample. The sample is a 60 nm thick gold film coated on a piece of glass substrate, prepared with an E-beam evaporator (CHA Industries). Single nanoslit of 200 nm wide are milled by FIB.
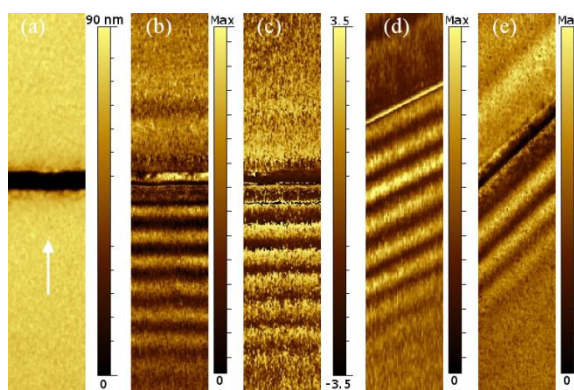
Figure 4.10. The s-NSOM images of a single slit, (a) topography image of the slit, (b) optical amplitude result, (c) optical phase result, (d) optical amplitude result when nanoslit is orientated at 26°, and (e) optical amplitude result when nanoslit is orientated at 45°. The image size is 1um by 5um.

The pseudo-heterodyne measurement is conducted for this sample, using platinum coated commercial AFM tips (ARROW-NCPt, NanoWorld) (Li, et al., 2014). Signals at the 1st and 2nd sidebands of the second harmonic are acquired to decouple the amplitude and phase information of optical near fields, based on the theories described in Chapter 3. The experiment results are shown in Figure 4.10. Figure 4.10 (a) shows the topography of the nanoslit structure. The white arrow in the figure shows the direction of the incoming

excitation beam. Figure 4.10 (b) and (c) gives the decoupled amplitude and phase information of the optical near field. To understand the formation of the fringes, the distributions of optical near fields with nanoslit at different orientation angles relative to the incident beam have also been recorded ((d) and (e)). The optical images in Figure 4.10 show consistent results of different fringe patterns on the both the sides of the nanoslits: fringe patterns appear on the lower side, while no fringes or slow variations appear on the upper side of the slit. All fringes are parallel to the nanoslit. It's also noticed that the envelope of the phase fringes is $\pi/2$ ahead of the envelope of amplitude.

To interpret the observed interference fringes, an analytical model has been proposed and numerical simulations have been conducted. It's known that nanostructures on metal surfaces could excite surface plasmon polariton (SPP) under laser excitation (Philippe, Lalanne, and Hugonin, 2006). Simple structures such as nanoslit can also have very high efficiency in SPP generation, especially at an oblique angle (Lalanne, et al., 2006). This is usually the case for reflection type s-NSOM setup with a collection objective from side. Being aware of this phenomenon, the fringes could be a result of interference between the SPP launched at the nanoslit and the in-plane component of the incident wave. The *p*-polarized light will launch SPPs on both sides of the slit. The SPPs propagate away from the nanoslit on both sides. The in-plane wave vector of incident light interferes with the SPPs and fringes are formed on both sides. This type of laser-SPP interaction can be described by an analytical model (Zhang, et al., 2011; Wang, et al., 2009). Due to the different propagation directions of the SPPs, the interference periods on two sides of the nanoslit will be different, which can be described as:

$$\Lambda^- = \lambda_o \lambda_{SP}/(\lambda_o + \lambda_{SP} \cdot \sin(\theta)\cos(\varphi)) \qquad (4.1)$$

$$\Lambda^+ = \lambda_o \lambda_{SP}/(\lambda_o - \lambda_{SP} \cdot \sin(\theta)\cos(\varphi)), \qquad (4.2)$$

where λ_o in this case is 633 nm of the incident He-Ne laser, λ_{SP} is the wavelength of SPP, θ is the angle of incidence with respect to the sample surface normal, and φ is the angle between the incident plane and normal direction of nanoslit. The permittivity of the used gold film is obtained by an ellipsometer to be -10.789+1.902i at 633 nm. θ is fixed at 58° in the setup. With these values, the periods Λ^- and Λ^+ are found from Equation (4.1) and Equation (4.2) to be 334 nm and 3.1 µm, respectively, in the case that the orientation of nanoslit is perpendicular to the plane of laser incidence ($\varphi = 0^o$). These equations also indicate that the period of interference fringes will increase as the orientation angle φ increases. However the fringes will still be parallel to the orientation of nanoslit. For example, when $\varphi = 26^o$, the periods Λ^- and Λ^+ will be 349 nm and 2.2 µm respectively; and when $\varphi = 45^o$, the periods Λ^- and Λ^+ will be 383 nm and 1.4 um respectively. Note the spacings of fringes are identical for out of plane and in plane incident fields.
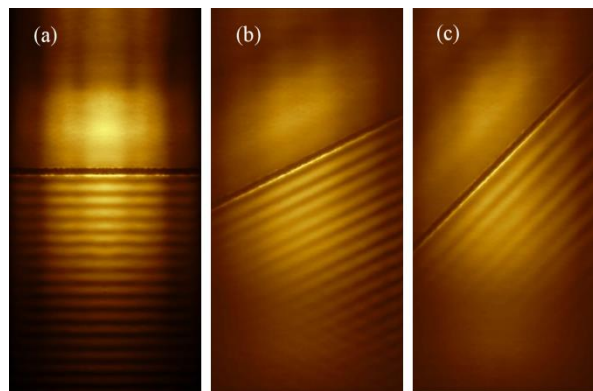
Figure 4.11. Numerical simulation of nanoslit under illumination of Gaussian beam. The slit angle varies as (a) 0°, (b) 26°, (c) 45°. The size of image is 5 µm by 10 µm.

Numerical simulation has been carried out using a commercial frequency domain finite-element method software (HFSS, Ansoft LLC) (Li, et al., 2014). For simplicity, NSOM tip is not included in the simulation. A *p*-polarized Gaussian beam with a beam waist of ω_o=2 μm, focusing at the center of the nanoslit, is used to excite the interaction. The simulation result of the transverse electric field component E_z is shown in Figure 4.11. The simulation shows consistent results with the experiment measurement presented in Figure 4.10. Different patterns form on both sides of the nanoslit, and the fringes always follow the orientation of the nanoslit. For different orientations, the periods of fringes on the lower sides are different, that is 333 nm, 359 nm, and 408 nm for angles of 0°, 26°, 45°.

The same analytical model can also be used to explain the measured phase information. Following same methodology, the total field as the superposition of the incident field, its reflection, and the SPP launched by the nanoslit could be expressed as follows for a TM mode plane wave incidence,

$$E = E_o \exp[j(\omega t - k_o \cdot r)]. \tag{4.3}$$

The Ez field for *x*<0 can be expressed as,

$$E_z^-(x, z) = E_o \sin(\theta) \exp(-jk_\parallel x) \, [\exp(jk_\perp z)$$
$$+ r\exp(-jk_\perp z)] + A\exp(jk_{SP}x) \exp(-\gamma z), \tag{4.4}$$

$k_\parallel = k_o\sin(\theta)$, $k_\perp = k_o\cos(\theta)$, *r* is the Fresnel reflection coefficient, $\gamma = (k2sp - k2o)^{1/2}$, and $x = 0$ is at the center of the nanoslit. A is the relative amplitude of SPP compared to the amplitude of the incident wave. Its value is determined to be 0.1-1i through matching both the interference contrast and the position of the peaks of the measured amplitude (Figure 4.12 (a)). In Figure 4.12 (b), the plot of the calculated amplitude and phase of E_z

at $z=0$ is presented. The plot shows that the periodicity of the near field phase (red curve) is the same as the periodicity of the near field amplitude (black curve). The phase envelope shows a lead of $\sim \pi/2$ relative to the amplitude envelope. These results are consistent with the measurement shown in Figure 4.10 (b) and (c). The numerical simulation conducted using HFSS also provides information between amplitude and phase, as shown in Figure 4.12 (c).
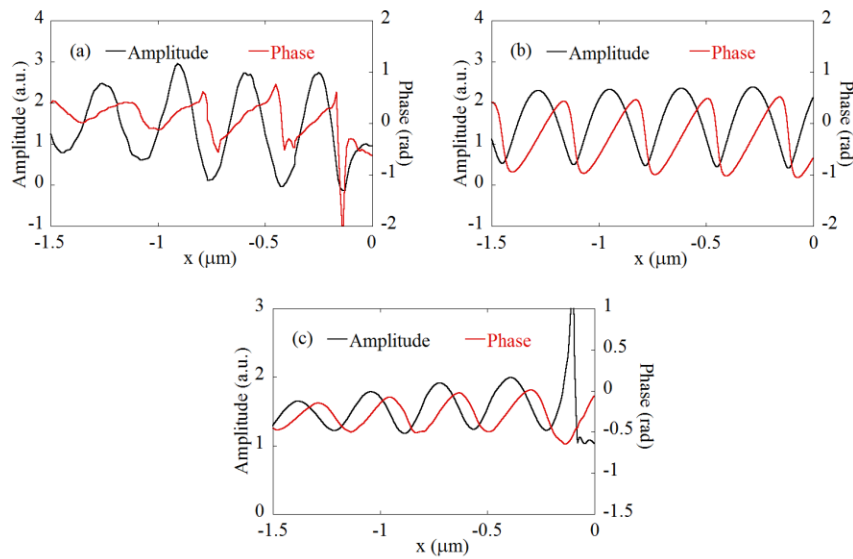
Figure 4.12. (a) Profiles of measured amplitude and phase. (b) Calculated amplitude and phase from Equation (4.4). (c) Amplitude and phase from numerical simulation.

The experiment results in general agree with the calculations from analytical model and numerical simulation. The differences could result from a few factors. For example, a plane wave illumination with a uniform wave front is assumed in the analytical model, while a focused Gaussian beam is used for the experiment, which results wavevectors in different directions. Also, the focusing position of the laser on sample is changing relative to the position of slit since the sample is scanned with a stationary tip for the scanning process. Besides, the existence of s-NSOM tip also affects the formation of interference pattern.

The analytical model predicts that fringes should exist on both sides of the nanoslit with different periodicities, while in s-NSOM measurements predominant fringes appear only on one side of the nanoslit. As discussed earlier, the main reason is, during the measurement, the sample is scanning while the focused laser position is fixed at the static tip. As a result of the limited laser focal spot size, the slower fringe periods on the upper side of the nanoslit in Figure 4.11 cannot be observed in experiment.

In the analytical model and the numerical simulation, only the SPP generated by the nanoslit is included. However, the s-NSOM tip could provide field enhancement and thus launch SPP as well (Krug II, Sánchez, and Xie, 2002). For example, under infrared laser irradiation, interference patterns have been observed in a graphene sample (Fei, et al., 2012), which was explained as interference between the SPP launched by s-NSOM tip and the reflection of SPP from graphene boundary. In the measurement conducted here, the fringe periods vary at different orientations of the slit and totally different fringes at two sides of the slit indicate that the formation of these fringes is not a result of the interference between tip-launched SPP and slit-reflected SPP, otherwise the period of these fringes should be independent of the nanoslit orientation, and fringes with the same periodicity would appear on the two sides of nanoslit.

A different experiment is also carried out under different focusing conditions to further verify that the interference pattern is resulted from the SPP launched at the nanoslit. The focused laser spot is positioned at different location relative to the tip as shown in Figure 4.13 (a) at a separation of 0.5 μm. In the scanning process of s-NSOM, the sample moves relative to the tip to form the image. Thus the relative position between the focal spot and the tip does not change during the process. At three different locations 1, 2, and 3 shown

in Figure 4.13 (a), the corresponding s-NSOM image is obtained and shown in Figure 4.13 (c), (d), and (e), respectively. Figure 4.13 (b) is obtained by scanning the tip scattered signal with an objective scanner by blocking the reference light. The position of the probe cantilever is represented with a red dashed line in the image. The optical alignment can also be verified with this map. The center position 2 is determined from the same image. By manipulating the focal position of the laser, the NSOM images show a strong dependency relation on the positions. When the focal position is to the left of the s-NSOM tip apex, the interference fringes are strongest. On the other hand, the fringes are weakest when the focal position is at 3. This is additional evidence that the SPP formed by the slit produces these fringes rather than the tip excited SPP.
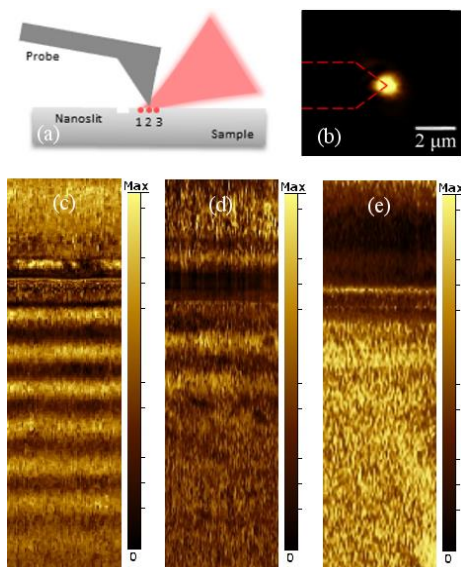
Figure 4.13. (a) Illustration of the tip-sample region with focused laser applied (separation between 1, 2, 3 is about 500 nm); (b) Imaging the position of focal spot by tip scattered light; (c) optical image when laser focused at point 1; (d) optical image when laser at point 2; (d) s-NSOM image when laser focused at point 3. Image size of (c) (d) (e) is 1 μm by 3.5 μm.

4.5   Conclusion

In conclusion, a reflection type s-NSOM setup implementing pseudo-heterodyne detection scheme is built. The building blocks of this s-NSOM are introduced in details. The optical alignment procedures are addressed with emphasis on achieving uniform interference pattern. With this s-NSOM setup, the near field distribution of a circular aperture array sample is investigated. Different detection schemes are applied for this investigation. The comparison of the obtained results shows the effectiveness of pseudo-heterodyne method in the background suppression. In the end, the experimental measurement of a single nanoslit is performed to confirm the measured optical signal is not a result of topographical effect. The mechanism of fringes formation in the nanoslit result is also explored with an analytical model and simulation.

CHAPTER 5. TRANSMISSION TYPE S-NSOM AND MAPPING OF PLASMONIC NANOSTRUCTURES

For many types of plasmonic nanostructures, especially for structures like nanoapertures, it is their transmission properties intriguing the research interest. As the reflection type s-NSOM can only excite the structure from a side illumination, a transmission type s-NSOM will be necessary for this type of measurement. For a transmission type s-NSOM, the main difference is that the sample will be illuminated from the bottom. The electromagnetic field distribution on top of the sample surface will be collected in the same way as using a side mounted objective. In this chapter, a transmission type s-NSOM is constructed based on the reflection type s-NSOM described previously. With this transmission s-NSOM, the optical near field of light transmitting through a bowtie aperture is investigated.

5.1   Transmission S-NSOM Setup

The transmission s-NSOM is built using the same hardware as in the reflection s-NSOM. The optical path is designed that the switch between the two modes requires minimum effort. The AFM sits on top of a large aluminum plate of one inch thick, to improve the stability of the AFM system and the interferometer. The collection and detection optics are also placed on top of the plate to reduce the optical path and have a stable support. The height of laser exit is lower than the aluminum plate. The excitation laser passes

through the optical isolator and beam expander and reaches the first beamsplitter beneath the thick plate. This beamsplitter has an 80:20 splitter ratio, to increase the laser power for excitation and avoid saturating the detector with a too strong reference light. The excitation laser then goes through a Nikon objective to focus to the bottom side of the sample (10X, 0.3NA or 50X, 0.55NA). The objective is mounted on an objective scanner (OS001-R, AIST-NT Inc.), which is used for fine alignment of the focused laser to the NSOM tip. On top of the sample surface, the light scattered by the tip will be collected by a side-mounted objective, same as the one used in reflection mode. Meanwhile, the reference light is also directed to the top of aluminum plate. The scattered light and reference light meet at a second beamsplitter to form interference and detected by an
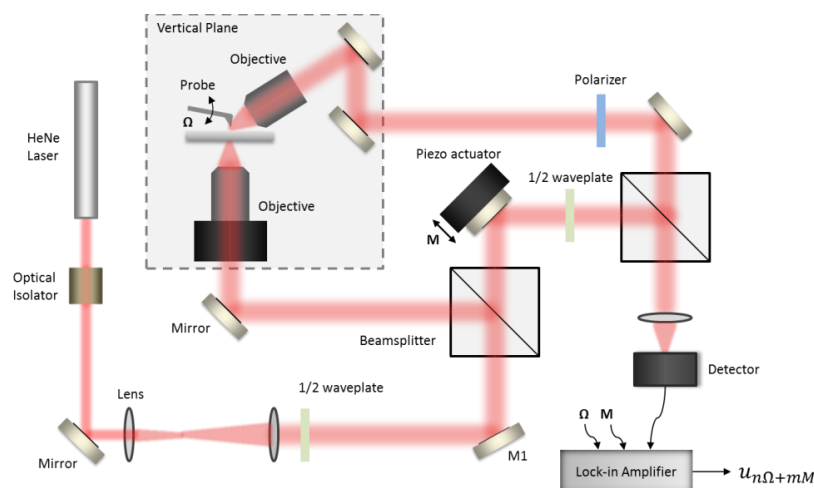
Figure 5.1. Schematic of the transmission type s-NSOM.

APD detector. This second beamsplitter also has a non-equal splitting ratio of 90:10, to favorably transmit the scattered light from the tip. The detector signal then goes through the lock-in amplifier and AFM controller for mapping purpose. To modulate the phase of reference light, a piezo actuator is applied in the middle of the reference light path. Since the reference path is no longer a round trip as in reflection mode, to achieve the same

modulation depth, the travel range of the actuator needs to be doubled. A schematic of the transmission s-NSOM is shown below in Figure 5.1.

While the alignment procedure is fundamentally similar to the procedure for reflection s-NSOM, there're a few additional steps due to the use of two objectives. Firstly, standard AFM operation is conducted and AFM tip is landed onto the sample surface. Then the sample is retracted, while the tip is maintaining its position. The position of the bottom objective is adjusted so that it focuses near the tip. Then the mirror M1 on a translation stage (Figure 5.2) is moved out of the light path, so that the laser light scattered by the tip
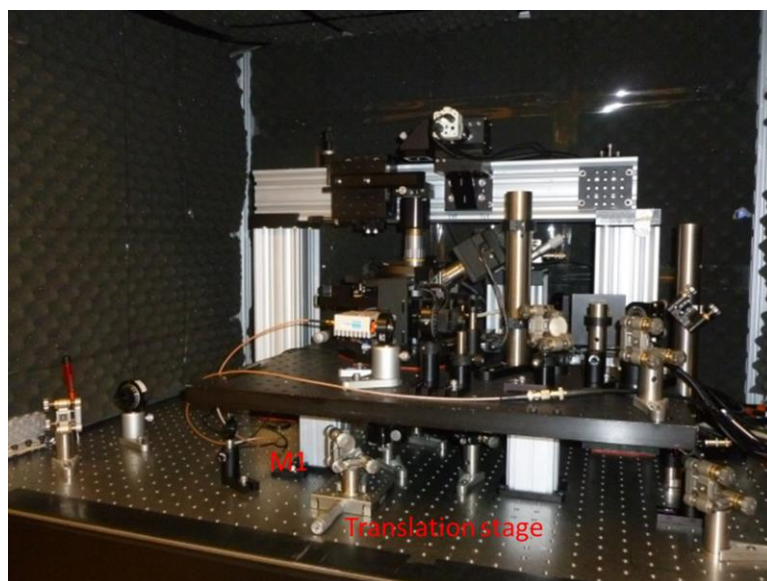
Figure 5.2. Photo of the transmission s-NSOM setup.

can be directed to the side mounted objective as in reflection mode. The scattered laser light goes through the side-viewing camera and is focused by the objective. Adjust the position of side objective so that the probe tip is at the center of the field of view and in focus. This can be done by a few iteration steps. Firstly, align the laser beam to normal incidence and pass through the center of objective mount with the objective removed.

Then, with the objective mounted, adjust the position of the objective by manual position stages to focus the laser at the apex of the probe tip. Repeat the steps till the laser pass through the center of objective and focus nicely at tip apex. After that, the mirror M1 can be moved back to its previous position. Through a transparent region of the sample, the laser can be focused directly to the AFM tip. The light scattered from the tip is visible through the side mounted objective. The camera from the side shows the image of the tip and the focused light (Figure 5.3 (a)). The manual stages for the bottom objective are used to align the position of focused spot, so that it is right at the tip. This alignment can be confirmed by imaging of the scattered light by scanning the bottom objective. The scattered intensity is proportional to the local field near the tip apex. It's also noticed that,
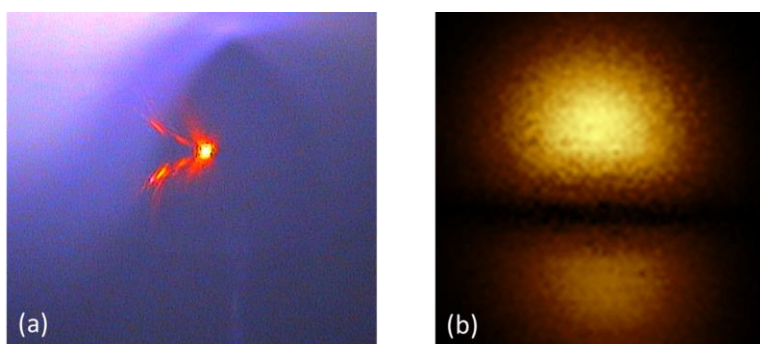
Figure 5.3. (a) An image of the laser focused at tip apex by the video camera. (b) An example of mapped scattered intensity, with a scan size of 8 μm by 8 μm

for small oscillation amplitude, the first harmonic signal of lock-in amplifier is proportional to the derivative of the signal (Bouhelier, Beversluis, and Novotny, 2003). By mapping the scattered light intensity, the position of laser spot relative to the tip apex and the spot size can be characterized. An example of the mapped scattered intensity is shown in Figure 5.3 (b).

Then the reference light is aligned so that it follows the same optical path and interferes with the scattered light. The interfered light is then directed and focused to the APD detector. Theoretically the bottom laser doesn't need to be focused to the tip as long as the collection is centered at the tip-sample interaction region. However, for small structure and very local field confinement, the excitation condition requires the laser to be near the structure, thus near the probing tip. Focusing the laser at the tip also makes the alignment much easier. Besides, it is always possible to move the laser away from the tip if it is going to be a concern.

5.2   Transmission S-NSOM Measurement – Interferometry and Harmonics

The transmission type s-NSOM is firstly tested by measuring the optical near field of a bowtie aperture on a gold film. With interferometric method applied, it's expected to be able to characterize both the amplitude and phase information of the optical near field near the bowtie aperture. Meanwhile, for measuring an aperture in an opaque film with transmission type s-NSOM, since the excitation laser is attenuated by the film, the background is expected to be small. Thus, experiment results without using reference light are also obtained for comparison. Because of the complex interaction between the tip and sample, the interferometric detection and the high harmonic demodulation, the experimental s-NSOM results don't always reflect the true optical near fields. Here the true optical near fields mean the expected theoretical or numerical calculated field distribution from the measured device itself. To gain insight into the mechanism of the near-field interaction and understand the influence of experimental parameters, the measurements have also been conducted for several different harmonics.
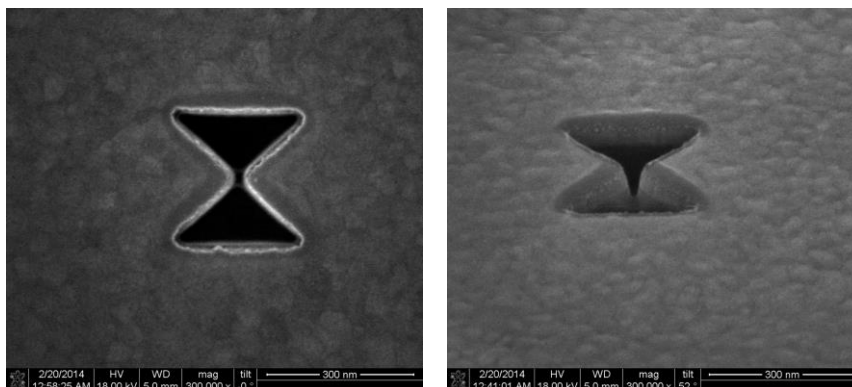
Figure 5.4. SEM images of bowtie aperture viewing (a) from top and (b) from side.
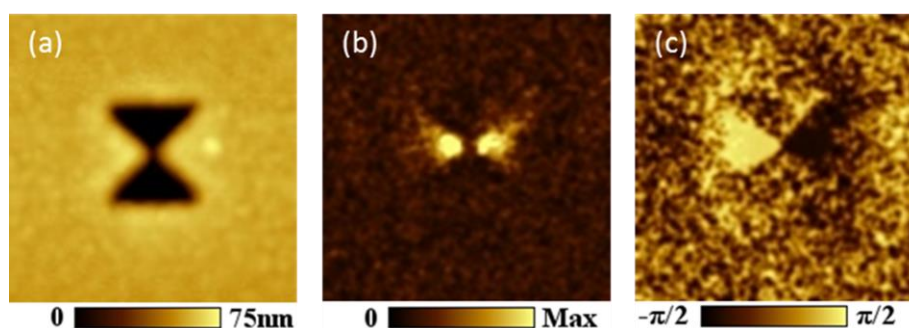
Figure 5.5. The topography (a), amplitude (b) and phase (c) results of transmission s-NSOM measurement of a single bowtie aperture, scan size 800 nm by 800 nm (160 by 160 pixels).

The sample is fabricated on a 60 nm thick gold film coated on a glass substrate with an E-beam evaporator (CHA Industries). The bowtie apertures are milled using focused ion beam with 10 pA current (FEI Nova 200 dual-beam FIB). 1 pA current is also tried but shows no obvious improvement and it heavily relies on the beam alignment condition. The designed dimension is an outline of 250 nm with a gap size around 20 nm. The SEM images of the fabricated bowtie are shown in Figure 5.4. While FIB is able to fabricate structures with a resolution of about 10 nm, it's noticed from the SEM images that there are still a few defects in the milled bowtie aperture. The outline looks rough and has small dots around, likely resulted from redeposition process. More critically, the cross

section of the bowtie gap has two segments of tapered sidewalls, as marked in Figure 5.4 (b). These tapers have strong affection of the performance of a bowtie aperture, which will be addressed later.

S-NSOM imaging of the optical near field near the bowtie aperture is performed with an excitation source of 633 nm HeNe laser using a commercial Silicon tip (Arrow NCR, NanoWorld AG). The probe has a nominal tip radius of 10 nm, with a force constant of 42 N/m and resonant frequency at 285 kHz. A scanning amplitude of 16 nm is used. The bowtie aperture is illuminated from below, with the polarization of incident light across the bowtie gap, as marked in Figure 5.5 (a). The pseudo-heterodyne method is applied for background suppression. The optical signals are measured at the third harmonic. At the fourth harmonic, the signal is usually buried in noises and not able to be distinguished from the background. Figure 5.5 (a) shows the topography of measured bowtie aperture. Due to the characteristic of the elongated tip in s-NSOM, the tip responses mostly to the out of plane component E_z of the near field, while the in plane component E_x is only weakly scattered and hardly detected (Olmon, et al., 2010; Schnell, et al., 2009). Thus the polarizer has been applied to only selectively detect the E_z field, and a mirror and a half waveplate are used to adjust and rotate the reference light to maximize the interference signal from lock-in amplifier. The optical amplitude and phase information of the E_z field are shown in Figure 5.5 (b) and (c). The expected E_z field distribution has localization and enhancement near the bowtie gap. There will also be a π phase jump near the gap. The experiment results show a good agreement with the expected field distribution. Pt-coated tips can yield similar results as of silicon tips. It is noticed that with Pt-coated tip, the AFM's ability to follow the surface topography is affected stronger than with Si tip.

This could be a result of stronger laser heating. Since Si tip can already give good SNR at the third harmonic, only Si tip is used for interferometric measurement in this work.
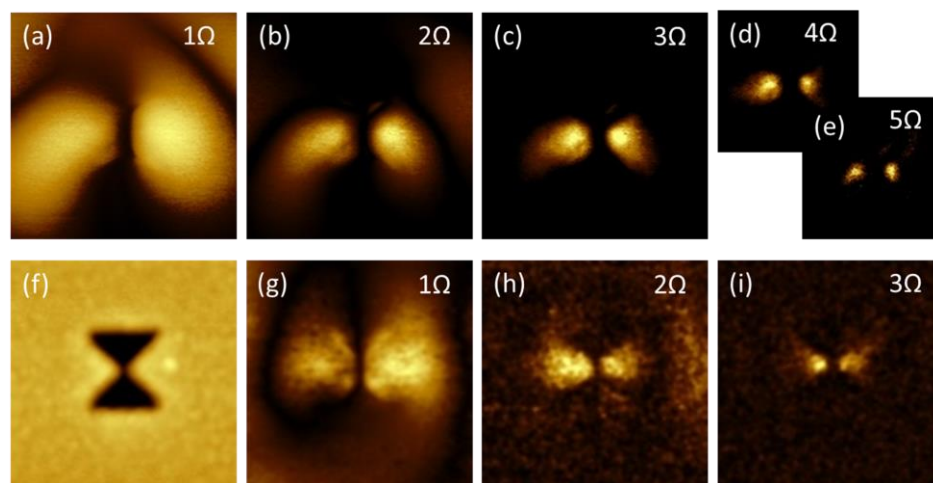
Figure 5.6. The 1st to 5th harmonic s-NSOM results of bowtie aperture without interference reference (a-e), the topography image and the 1st to 3rd harmonics results with interference (g-i). Scan size is 500 nm by 500 nm for (d) and (e), and 800 nm by 800 nm for the rest.

In Chapter 3, the different techniques for suppressing background noises have been introduced, such as high harmonic demodulation and interferometric measurement. Due to the configuration of transmission s-NSOM, the background is greatly reduced for measurement of aperture type nanostructures. So it's a natural question to ask, is an interferometric measurement still necessary? Here the results of using the transmission s-NSOM measuring the bowtie aperture both with and without interferometric method are presented in Figure 5.6. In addition, the results for signal demodulated at different harmonics are also included.

Figure 5.6 shows the topography of the bowtie aperture, and optical signals obtained at different harmonics without and with applying interferometric measurement. The results are presented for up to 5Ω for non-interferometric measurement and up to 3Ω for

interferometric measurement. In all the optical images, there're two hot spots near the gap of the bowtie aperture, which is consistent with the expected E_z field distribution as discussed before. For both types of measurements, a clear trend is observed. As the demodulation order increases, the measured FWHM of the spot size reduces and is closer to the true optical near field (Figure 5.7 (c), addressed later). The FWHMs for the measurements are obtained by drawing a line cross section through the two hot spots. The sizes are from 300 nm at 1Ω to 60 nm at 5Ω for non-interferometric measurement, and from 260 nm at 1Ω to 80 nm at 3Ω for interferometric measurement (Figure 5.7 (c)). For both types of measurement, the increase in harmonic order greatly helps to eliminate the undesired background. For the same harmonic order, interferometric measurement results in a smaller spot size with cleaner background. It's also observed that signal can be obtained at as high as 5th harmonic for non-interferometric measurement, while only 3rd harmonic signal can be obtained for interferometric measurement at this moment. In the non-interferometric measurements, there're asymmetric tails, especially at low harmonics. This could because of the relative position of the probe and the side-mounted collection objective. As a result, the background scattering is more strongly modulated for the lower part than the upper part of the images.

Simulation work has been done regarding interpretation of the measured signals (Zhou et al. 2014). Figure 5.7 (a) shows the simulated near field distribution. The dimensions of the bowtie aperture for the simulation are measured directly from the SEM images, including the tapering at edges (Figure 5.4). The tapered gap degrades the field enhancement and localization. For example, at a plane of 8 nm above the aperture exit, the peak enhancement factor is 0.8 for E_z while it is 2.34 if there is no taper. As a result,

we're only able to map the E_z field. Figure 5.7 (b) shows the line profiles at 8 nm above the aperture (only half of the dimension is plotted due to symmetry). The FWHM of the spot size for E_z field is about 59 nm. The height of 8 nm is chosen to better match the experimental data. In actual experiment, due to the finite tip size and probe oscillation, the signal does not origin from a single point (or a single height). Thus an equivalent height is used for comparison purpose. Another more complicated simulation is also carried out to include the influence of tip oscillation and the demodulation process by a lock-in amplifier (Zhou et al. 2014). This simulation model includes the tip with a conical shape. The far field signal is calculated from the radiated fields over a surface by applying the Green theorem. The tip is assumed to be oscillating at a frequency of Ω, to modulate the tip sample separation. As a result, the collected far field radiation signal is also periodic. The demodulated signal at the n-th harmonic from the lock-in can be calculated from the Fourier transform (Fikri, et al., 2004; Zhou, et al., 2014):

$$E_n \propto \int_0^T S(t)e^{-in\Omega t}dt \propto \int_0^{\frac{T}{2}} S(t) \cos(n\Omega t)\, dt, \tag{5.1}$$

where $S(t)$ is the time-dependent far field signal, T is the period of tip oscillation. Figure 5.7 (d) shows the simulation model. Figure 5.7 (e) shows the calculated signal at different harmonic orders, with the black curve denoting the local field calculated from a bowtie aperture only. With increase in the harmonic order, the spot size approaches the calculated local field. The same methodology and Equation (5.1) can also apply to the field predicted by the dipole model shown in Figure 3.2. The harmonic demodulation results of the dipole field are shown in Figure 5.7 (f). The same trend is observed, higher harmonic can reveal a smaller or sharper field change. It is also noticed that the

demodulated signal is quite different from the black curve predicted by the dipole model. The result from dipole model can be understood as the scattered field picked up by the detector. There is a strong background even when the tip is quite far away from the sample surface. The demodulation process effectively removes the background and leads to a faster decay rate near the sample surface.
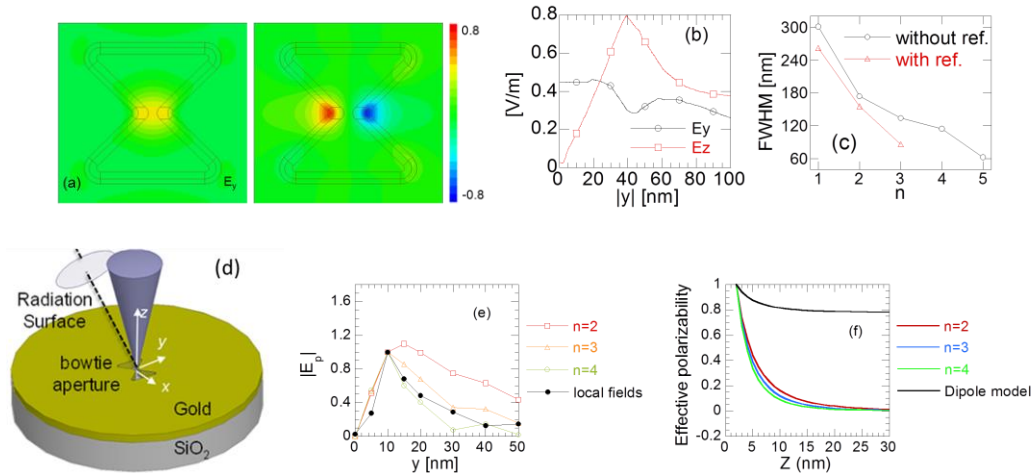
Figure 5.7. (a) Simulated near field distribution for the fabricated bowtie aperture (400 nm × 400 nm), (b) Line profiles of electric fields across the gap, (c) FWHMs for s-NSOM measurements, (d) the model for FEM simulation, and (e) simulated signal at different harmonics (Zhou, et al., 2014). (f) Harmonic signal for the field predicted by dipole model.

5.3   Three Dimensional Near Field Mapping of Bowtie Aperture

Optical antennas have drawn great research attention because of their abilities to efficiently increase the light-matter interaction, enhance and confine the electromagnetic fields on the nanometer scale. These capabilities have led to a wide range of applications, such as surface enhanced Raman spectroscopy (Campion and Kambhampati, 1998), high resolution optical lithography (Uppuluri, et al., 2010), plasmonic optical tweezer

(Roxworthy, et al., 2012), nanophotonic devices (Yu, et al., 2007), and high resolution optical spectroscopy (Ichimura, et al., 2004). For a desired functionality, the design of an optical antenna is usually determined through numerical simulation of the electromagnetic fields. While this process could qualitatively define the response of an optical antenna, the performance of the antenna also heavily relies on the fabrication techniques and the operation conditions of the device. For optical antennas, the nanometric dimensions, especially for features like gaps and sharp structures, are critical to the characteristics of the antennas' optical response. Their fabrication is usually hindered by the achievable resolution limited by current techniques (Lérondel, Kostcheev, and Plain, 2012). Thus an experimental investigation of the optical near field distribution can provide valuable information on the validation of the design and evaluation of the performance.

There have been quite a lot of efforts dedicated to visualizing the optical near field distribution of optical antennas, especially by applying the near-field scanning optical microscopy method (NSOM). For example, with aperture type NSOM, the optical near field distribution of bowtie aperture antenna has been mapped in both two and three dimensions (Jin and Xu, 2006; Guo, et al., 2010) for visible wavelength. With scattering type NSOM (s-NSOM), optical near field amplitude and phase images have been obtained for several different antenna structures working in the long wavelength infrared range, such as rod, disk, and triangle antenna (Martin, et al., 2010; Rang, et al., 2008). Most of the previous researches were conducted in two-dimensional plane mapping or one-dimensional line scanning, especially for the case of s-NSOM. In this work, a three-dimensional mapping of the optical near field amplitude and phase with s-NSOM is

conducted. With the applied method, it's possible to construct the full three-dimensional distribution of the optical near fields. This has the potential to provide a full characterization of the complex vector fields around the antenna, and thus a direct evaluation of the functionality and performance of the antenna.

This capability is demonstrated by measuring the optical near field of the bowtie aperture antenna, the same type of nanostructure as discussed in previous chapters. Bowtie aperture has a characteristic E_z field distribution with two localized hot-spot across the gap and a π phase shift between the spots. This makes it an ideal structure for validating this method. Comparing to the previous three-dimensional measurement with aperture NSOM, there are several valuable advantages of conducting this measurement with s-NSOM. For the previous measurement (Guo, et al., 2010), it is not possible to access the near field distribution within 50 nm from the sample surface, due to the snap-in action of the tip when it's close to the surface. This neglects the most critical information of the optical near fields, as the signature of optical near field is its fast decay within the range of tens of nanometers. Also with constant height scanning mode, the feedback is off during the scanning process, having no control of tip-sample distance. The spacing between sequentially acquired height images is 25 nm, which is insufficient to capture the fast changing optical near field. In the last measurement (Guo, et al., 2010), only the intensity is measured. For a three-dimensional optical field, the amplitude and phase of different vector components are also necessary to understand the complex field. In this work, only the three-dimensional amplitude and phase of E_z field are mapped, due to the fact that the commonly used commercial tips in s-NSOM are most responsive to the out of plane component (Martin, et al., 2009). A recent simulation work considering a silicon

tip reveals that the response of tip to E_x field is only one tenth of that to the E_z field (Zhou, et al., 2014). However, with a special designed tip, it's possible to response to both the in plane component and the out of plane component, providing a full characterization of the vector near fields (Olmon, et al., 2010).
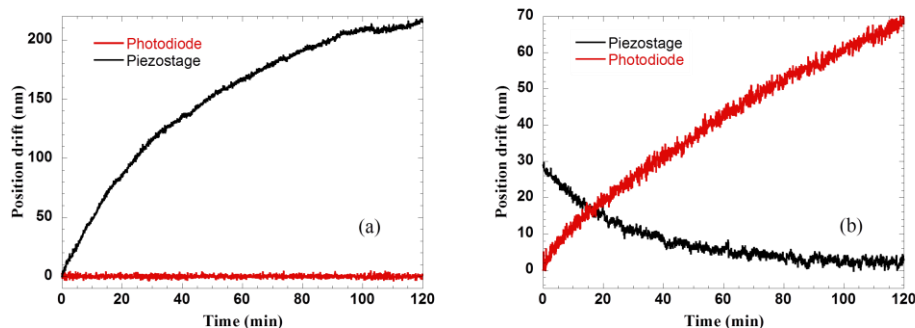
Figure 5.8. Measurements of AFM stability with feedback on (a) and off (b).

NSOM systems are usually equipped with the functions of the two-dimensional plane scanning and one-dimensional force-distance curve measurement, as in most scanning probe microscopy (SPM) systems. To obtain the information in the third dimension, intuitively, one can add either one additional dimension to the plane scanning function or two additional dimensions to the curve function. To be specific, by repeating XY plane scan at different heights, or by repeating the curve measurements over different positions in the XY plane, the three-dimensional information can then be constructed. With today's SPM technology, collecting information in a volume set is still a time consuming task. One s-NSOM image in two dimensions usually takes about 20 minutes to finish. Thus the stability of the system needs to be taken into consideration. For the first method mentioned, when tip moves a certain distance away from the sample surface, the mechanism maintaining the constant tip-sample separation will stop functioning. This

results in uncertainty in the measurement, especially in the Z direction. For the second method, a curve measurement within the range of tens of nanometers can be done in a very short time, like less than one second, thus minimizing the drifting in Z direction.
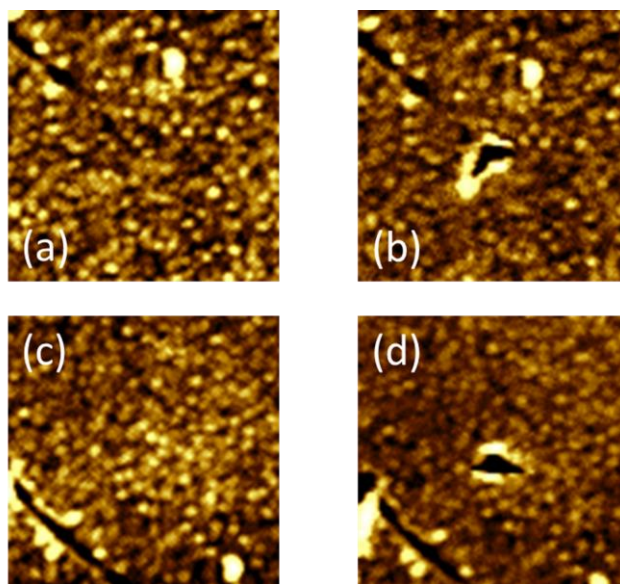
Figure 5.9. Topography measurements of AFM stability in lateral direction. Topography (b) is acquired 2 hours after (a) with feedback on. Topography (d) is acquired 2 hours after (c) with feedback off. The image size is 1 um by 1 um.

To evaluate the stability of the AFM system used here, the change in the system signals with feedback on or off during a time period of 2 hours is measured. The measurement is done in contact mode, with the same probe used for s-NSOM measurement. The probe has a nominal radius of 10 nm and a nominal force constant of 42 N/m. The sample used is also the same sample for s-NSOM, the Au film on a glass substrate. The left figure in Figure 5.8 shows the result for the case when AFM feedback is enabled. The red curve is the normal force signal from the feedback photodiode of AFM and is very flat during the two hour period. This indicates the feedback loop did a good job on maintaining the tip-sample interaction. The black curve is the signal from the position sensor of the sample

piezo stage. It indicates the position shift of the piezo stage to maintain the feedback, which is about 200 nm. The right figure shows the position drifting when the feedback loop is disabled. The piezo stage shows a drift of 30 nm, while the photodiode shows a drift of 70 nm of cantilever position. Considering the drifting direction, that is about 100 nm changes in relative position. The difference in the two measurements could possibly come from many factors, for example, different environmental conditions, system warm-up time, feedback electronics, etc. Even so, this provides a good estimation of the potential drift that may present in constant height measurements without feedback. This suggests the point curves method should be used to achieve better vertical resolution. To get a full evaluation of the stability, the drift in the horizontal plane is also investigated, as shown in Figure 5.9. These AFM topography scans are obtained right before and after the 2-hours collection of Z-drifting data. Figure 5.9 (b) is obtained after 2-hours measurement of Z-drifting with feedback on following Fig 5.9 (a). The drifting between (a) and (b) is about 30 nm in lateral direction. Figure 5.9 (d) is obtained after 2-hours measurement of Z-drifting with feedback off following Figure 5.9 (c). The drifting is about 50 nm, which is larger than in the feedback on case. It's also noticed from Figure 5.9 (b) and (d) that the tip scratched the sample surface after sitting on top of the stationary sample surface for 2 hours. This should due to the very stiff probe (42 N/m) used and the large force (>60 nN) applied. In s-NSOM measurement, the acquisition time is usually less than one hour. The tapping mode operation also applies much smaller force. These should help to reduce the drift in lateral direction. In practice, the lateral drifting has not been an issue yet.

With these in consideration, the three-dimensional measurement is conducted by performing approach curves at each XY position. The collected data are like a bundle of wires, from which volumetric information can be retrieved. For each curve, signal from several selected channels can be recorded simultaneously, such as optical signals from two sidebands from the lock-in amplifier when applying pseudo-heterodyne method, the oscillation magnitude and the movement of piezo stage. The position in the XY plane, together with other operating conditions will also be stored with each curve file. A simple topography image can be obtained prior to this process, which will be used to link each curve to the absolute distance from the sample surface. The final data represent the optical near field at each voxel inside the measured volume. The data can be easily processed by the numeric computation software MATLAB (MathWorks Inc.).
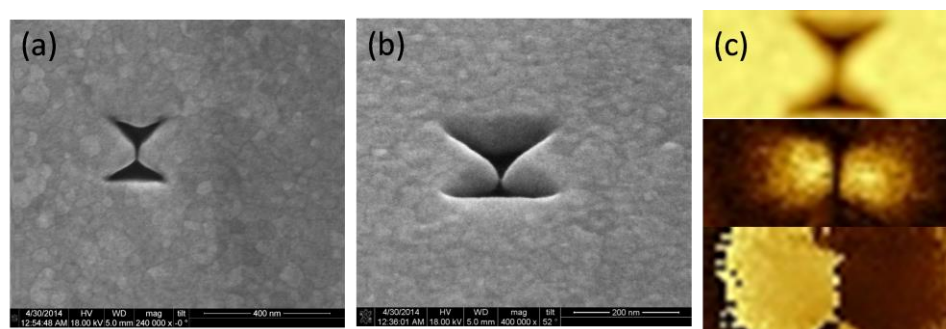
Figure 5.10. SEM images of fabricated bowtie aperture: (a) top view, (b) side view at 52o, (c) Two-dimensional result of topography, amplitude and phase (top to down, image size is 500 nm by 200 nm).

Because of the curvatures in the previous sample, a new sample is fabricated on a 60 nm thick gold film coated on a glass substrate with an E-beam evaporator (CHA Industries). This new sample is also fabricated with focused ion beam (FEI Nova 200 dual-beam FIB). However, a stream file is used to control the beam for patterning, while scripts are used for the previous sample. The designed dimension is an outline of 150 nm with a gap size

around 20 nm. The SEM images of the fabricated bowtie are shown in Figure 5.10. The cross section of the bowtie gap still has the tapered sidewalls. Although the different methods produce slightly different outlines, the edge curvature condition is not improved. The measurement is conducted with the home-made transmission types-NSOM system, as described in earlier sections. A 633 nm HeNe laser is used as the excitation source. The measurement is performed with a commercial silicon tip (Arrow NCR, NanoWorld AG). The bowtie aperture is illuminated from below, with the polarization of incident light across the bowtie gap. The pseudo-heterodyne method is applied for background suppression. The optical signals are measured at the third harmonic. A common two-dimensional scan is performed prior to the three-dimensional mapping. The optical amplitude and phase information are simultaneously obtained together with the topography, similar as the work done previously. As expected, the characteristic E_z field distribution of the bowtie aperture is obtained (middle figure in Figure 5.10 (c)). This result is equivalent to the case with a fixed position in the Z direction. Thus, it can help to decide the scan range for the three-dimensional imaging. It also helps to evaluate the signal quality before taking massive volume data.

The lateral scan range is determined to be 500 nm by 300 nm from the 2D image. The scanning resolution in XY plane is 50 pixels by 30 pixels. At each XY location, for example, the white spot (x_i, y_i) in Figure 5.11 (a), the sample piezo stage is swept in Z direction from 100 nm to -5 nm to acquire data at different heights. During the sweep, at each height Z, for example the Z_1 position in Figure 5.11 (a), signals from several different channels are simultaneously collected, such as the signal at different sidebands of modulation frequency and the tip oscillation amplitude, producing multiple curves at

the location of (x_i, y_i). Figure 5.11 (b) can be seen as an example as two curves obtained at (x_i, y_i). The tip is oscillating during the whole process, as represented by the blue dashed waves in Figure 5.11. The data collected at each height Z is a result of the tip oscillation. For each curve, 105 points are obtained during the sweep process, which defines the spatial resolution for data collection in Z direction. The zero of Z axis in the curves is automatically determined by the AFM control software (AIST, AIST-NT Inc., version 3.5.57ex1), which is about the location of the setpoint in the tapping mode amplitude approach curve. At each XY location, the curves are obtained by the same one sweep of the piezo stage. This ensures no spatial drifts between measured sidebands and also reduces the data collection time. In the end, a volumetric data set is created from the mapping process, which is essentially a multi-dimensional matrix. The optical amplitude and phase at each voxel can be calculated with the data at the same location in the curves. With the MATLAB software, surface plots at arbitrary locations and orientations can be obtained, which can be used to illustrate the three-dimensional optical near field distribution.

During the measurement, each curve is stored with the zero of Z axis defined relative to its own curve, as default in the AFM control software. Thus the curves need to be shifted to link to the real topographical heights. Besides, the s-NSOM tip is oscillating during the acquiring process. The Z position in the curve is a nominal position of the oscillating tip. A typical amplitude approaching curve is shown in Figure 5.11 (b), together with a mean normal deflection curve obtained at the same time. The typical behavior of an oscillating tip approaching surface is that its free oscillation amplitude, 29 nm in this case, will be damped as the tip approaches close to the surface and eventually stop oscillation as

indicated by the left flat region of the amplitude curve. The mean normal deflection curve shows the mean deflection of the cantilever is negligible until the tip oscillation amplitude is below 3 nm, which is already greatly damped.
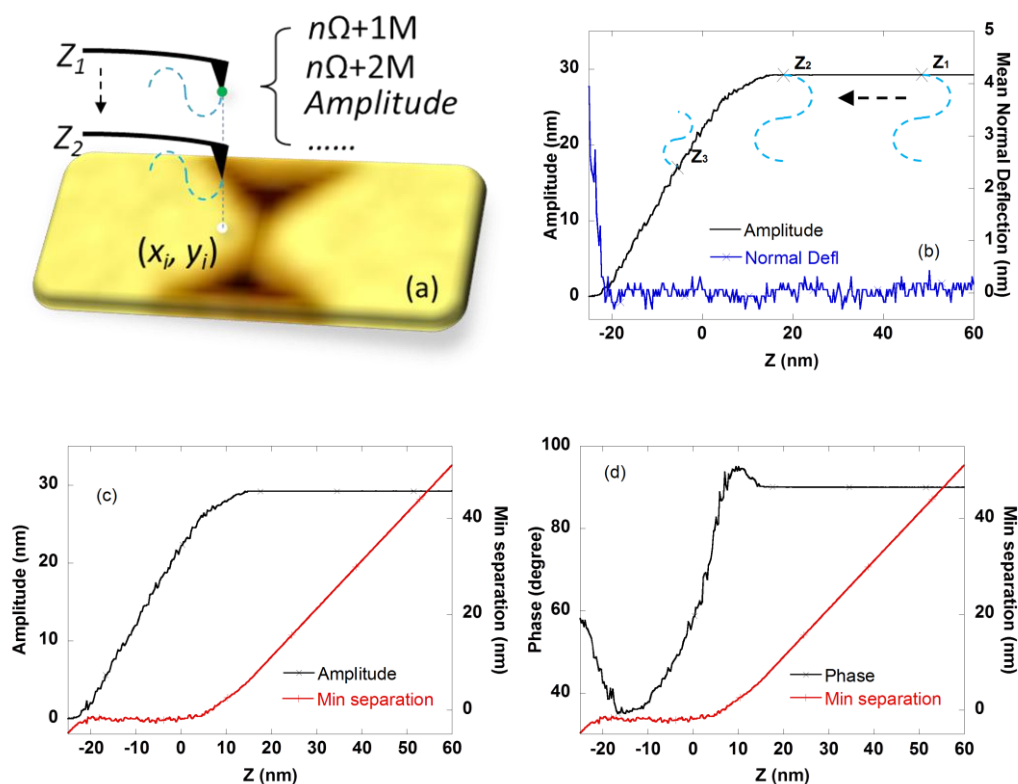
Figure 5.11. An illustration of the 3-D mapping process (a), the amplitude and mean normal deflection curves (b), amplitude (c) and phase (d) with the minimum separation curves.

In this work, to investigate the origin of the signal in the detection of optical near field, the concept of minimum tip-sample separation is used, which means the lowest position of the tip during its oscillation cycle. The Z axis in each curve is converted to the minimum tip-sample separation with the help of amplitude and phase approach curves, as shown in Figure 5.11 (c) and (d). The phase curve shows the tip is initially in the attractive region, then moves to the repulsive region as the tip approaches further to the

surface. When the tip just enters the repulsive region, where the phase lag quickly drops to below 90 degrees, the tip-sample separation is defined as zero at this location. With this definition, using the difference between the piezo movement and the change in tip oscillation amplitude, the Z axis can be converted into minimum tip-sample separations. Because the mean deflection of cantilever only starts to change when the amplitude is really small, it is neglected in the calculation. It is also outside the data collection range. With these considerations, the collected data has been processed with MATLAB, and is presented in Figure 5.12 and 5.13.

Figure 5.12 (a) and (b) shows the plots of the E_z amplitude and phase in XZ plane near the bowtie aperture gap. The field distribution is overlapped with the cross section profile of the measured topography by the height relation described above. Figure 5.12 (a) clearly shows the optical amplitude distribution in the space right above the sample surface. The E_z fields concentrate near the gap edges of the bowtie aperture. The hot spots tightly bound to the sample surface and decay very fast to the background. Due to the existence of the curvatures near the aperture gap, the enhanced fields are concentrated near the gap but also spreading following the curvatures, thus extending their sizes. In the phase image (Figure 5.12 (b)), the characteristic 180^0 phase shift is clearly revealed. Here also need to point out that Figure 5.12 is a qualitative expression of the position relation between measured signal and sample surface. In the figures, each measured optical signal is directly assigned to the lowest position of the tip oscillation cycle. In fact, this signal results from the full oscillation cycle, its effective height relative to the sample surface needs to be further investigated.
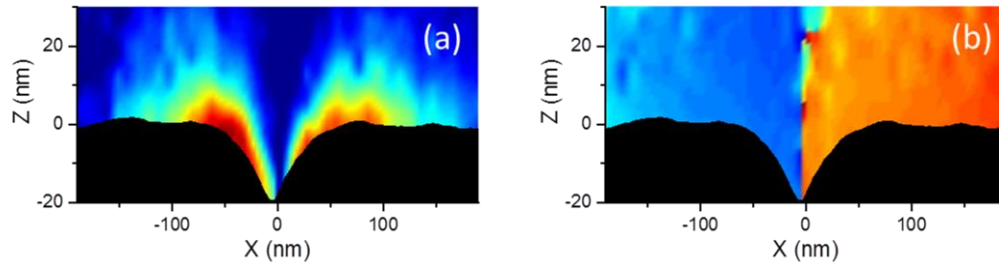
Figure 5.12. Overlapped image of sample surface and measured optical amplitude (a) and phase (b) in XZ plane across the gap of the bowtie aperture.
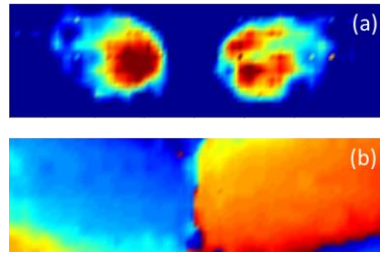
Figure 5.13. The reconstructed optical amplitude (a) and phase (b) in XY plane at -2 nm in Z direction (400 nm by 100 nm).

To get a better idea of the measured optical fields, the optical amplitude and phase at different plane have been constructed from the volume data set, shown in Figure 5.13. Figure 5.13 (a) and (b) are the amplitude and phase distribution in XY plane, which are obtained at a cross section of $Z = 0$ nm. The image sizes in (a) and (b) are cropped to be 300 nm by 200 nm. In the figures, the two separate hot spots of the E_z field are clearly identified. In between the hot spots is the minimal field corresponding to the gap of the bowtie aperture. The 180° phase difference between the hot spots is also detected in the experiment results. In Figure 5.13 (b), the hot spots are quite apart from each other with a distance of more than 100 nm. This is also observed in Figure 5.12 (a). It is clear that this separation is due to the edge curvatures in the fabricated bowtie aperture. It is worthy to

point out that the XY plane image is obtained in a horizontal plane at a fixed Z position, which is not following the topography of the sample surface.

Numerical simulation has been performed with the commercial FEM software (HFSS, Ansoft LLC). Besides the designed dimensions, the simulation model is also detailed with the critical curvatures obtained through the topography and SEM images. The bowtie profile dimension at the bottom is around 155 nm. By adding curvatures, the profile dimension at the top surface is around 220 nm. For the tapered aperture gap, the dimensions are 9 nm at bottom, 35 nm in the middle and 105 nm at the top. A top view of the modeled structure is shown in Figure 5.14 (a). In Figure 5.14 (b), the E_z field in XY plane on top of the gold film is plotted. Because of the curvatures, the hot spots are about 100 nm away from each other, reducing the confinement provided by a bowtie aperture. The tapered gap also degrades the field enhancement. This simulation result also quantitatively confirms the experiment results, as shown in Figure 5.13 (a). The distribution of the E_z field across the aperture gap in XZ plane is presented in Figure 5.14 (c) and (d). In this figure, a highly enhanced field locates near the bottom gap. As it propagates, the field decays fast and the stronger field spreads along the surfaces of the tapered edges. The enhancement of the field on the top surface is greatly degraded, due to the curvature and the widened gap on the top. Comparing with the measurement in Figure 5.13 (a), the strongest field at the bottom of the gap is not obtained, mainly due to the larger size of the tip radius which prevents it from reaching that region. Besides, the FIB often mills into the glass substrate during the fabrication process, which could also reduce the enhancement at the bottom gap. While on the tapered edges, the experiment is able to detect the bounded fields.
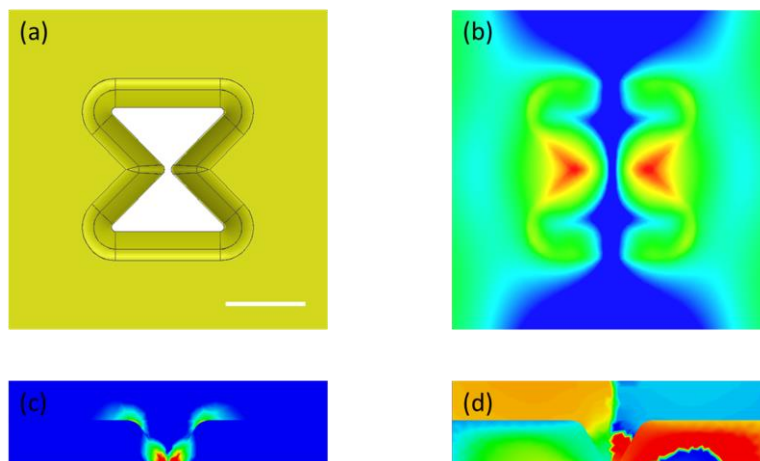
Figure 5.14. (a) The structure used for simulation. (b)Simulated Ez field in XY plane. Simulated amplitude (c) and phase (d) of Ez field in XZ plane across the gap. Scale bar is 100 nm.
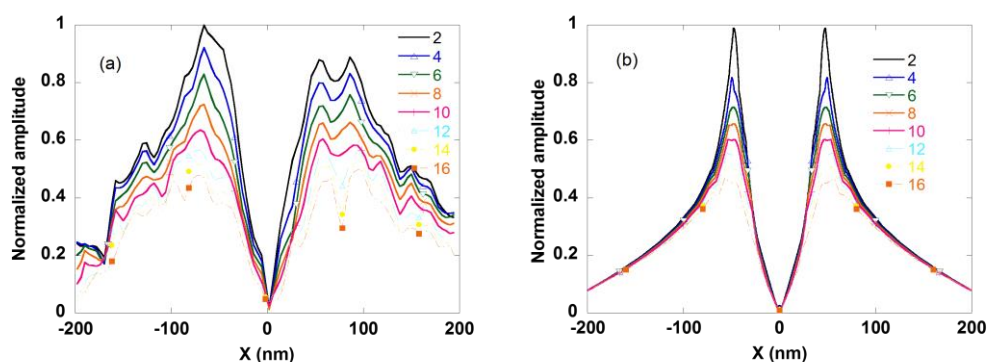
Figure 5.15. (a) Experiment and (b) simulation line profiles of the optical field across aperture gap.

As pointed out earlier, the previous presentation of the measured optical field simply considers the lowest position of the oscillating tip as its nominal height. This is not necessarily an effective height of the measured optical field in the vertical dimension. To better understand the effective height of the field, several line profiles across the aperture gap at different heights in XZ plane are plotted and compared with the simulation. In Figure 5.15, the profiles at Z equal to 2 nm to 10 nm are plotted.

In the simulation, the FWHM gets larger as the height increases, from 38 nm at Z_s=2 nm to 70 nm at Z_s=10 nm. In the experiment, the profiles are very noisy and difficult to determine FWHMs. A rough estimation is around 60 nm and doesn't change much as in the simulation. . This could be due to the finite size of the tip, the detectable signal level and the demodulation harmonics. The very fast decay of the field also makes it difficult to quantitatively characterize in the Z direction. The measured field is represented by its minimum tip-sample separation. As the separation increase, the field quickly becomes undetectable. Because of this, although it is inconclusive to get an effective height in this case, a tentative conclusion is that the effective height is in the bottom region of the tip oscillation range.

5.4   Three Dimensional Near Field Mapping of Au Grating

The near field of bowtie aperture is strongly confined to the sample surface and decays very fast. That means it is not a good example for studying the field distribution in the Z direction. Also, because of the limitation in the fabrication of a good bowtie aperture using the technology of focused ion beam, a new sample of Au grating is fabricated with the electron beam lithography (EBL) and a lift-off process. The new process is used to achieve a better vertical profile with a simpler structure. The Au grating is fabricated on a glass substrate. For the EBL, poly(ethyl methacrylate) (PMMA) and a Leica VB6 are used. Since the glass substrate is non-conductive, AquaSave 53za (Mitsubishi Rayon) is spin coated on the PMMA-coated sample, to avoid the charging effect during the EBL process. After the pattern is created, the sample is treated with O_2 plasma for 30 seconds to remove PMMA residues in the patterned region. Subsequently, 3 nm of titanium and

30 nm of gold are deposited using an electron beam evaporator. After that, the final lift-off process is done in acetone.
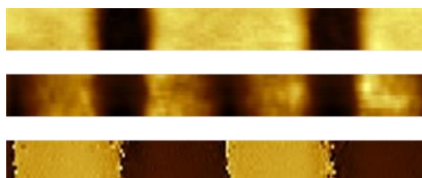
Figure 5.16. Topography of the Au grating and the optical amplitude and phase distribution (top to bottom, size is 1000 nm by 100 nm).
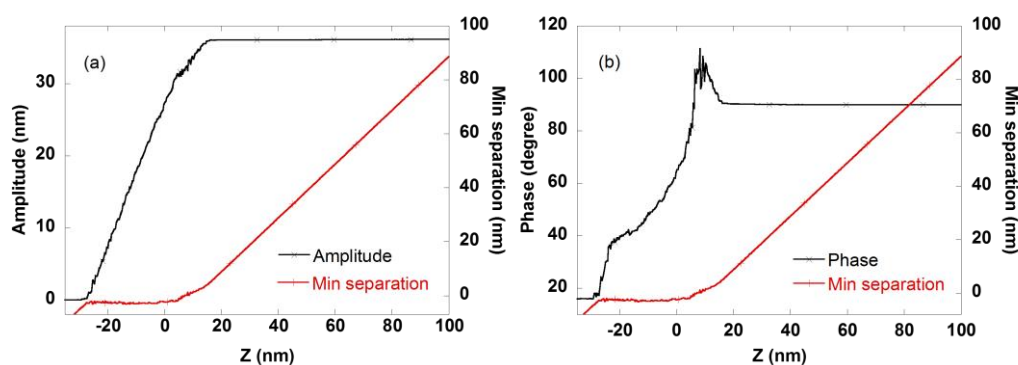
Figure 5.17. The amplitude (a) and phase (b) with minimum separation curves.

The experiment is conducted with the same setup and using the similar procedures as described in the measurement of the bowtie aperture. The same type of Si tip is used. The pattern scanned is designed to be 500 nm in period with a 200 nm opening. Before taking the volume data, a general 2-D scan in XY plane is performed. The topography along with the amplitude and phase distribution of the E_z field are obtained and shown in Figure 5.16. The volumetric data are then collected at each XY location, by sweeping the piezo stage in the Z direction. From the collected data, the optical amplitude and phase at each voxel can be calculated with MATLAB. In the end, surface plots at arbitrary locations and orientations can be generated to illustrate the three-dimensional optical field

distribution. Because of the symmetry within the structure, the amount of data that needs to be collected is greatly reduced. Especially in the direction along the slots, only a few points are necessary. This greatly reduces the measurement time to a few minutes, which equivalently increases the stability.

The scanning amplitude for the 2-D measurement is 33 nm, while the free amplitude is 41 nm, as shown in Figure 5.17. For each curve, the sweep is performed from 75 nm to -25 nm. After processing with MATLAB, the XZ plane plots of the optical amplitude and phase are shown in Figure 5.18. The optical images are overlapped with the sample surface (black region) obtained by AFM topography, with the optical heights linked to the lowest position of the tip oscillation cycle.
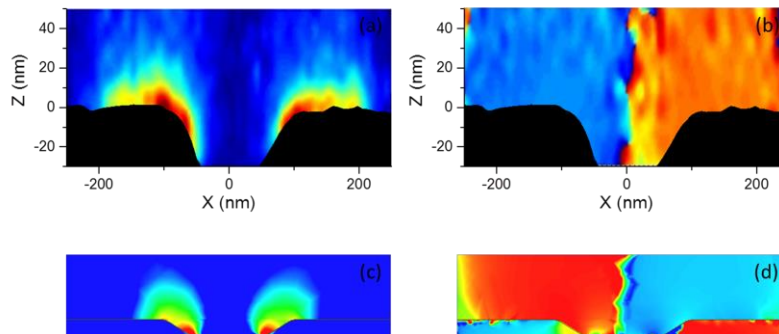
Figure 5.18. The measured amplitude (a) and phase (b) distribution in XZ plane and the simulated amplitude (a) and phase (b) in the same plane. The dimension in both (c) and (d) is 500 nm by 130 nm.

The experiment results in Figure 5.18 (a) and (b) show the E_z field in the space above the sample surface. Similar as the case of the bowtie aperture, the enhanced field locates near the edges of the gap. The field decays within a distance of tens of nanometers away from the surface, exhibiting a clear signature of the near field. In Figure 5.18 (b), the phase image shows a clear π shift in phase between the two hot spots. Comparing to the case of

bowtie aperture, the enhanced field extends further into space on top of the sample surface. Numerical simulation has also been conducted with HFSS and is shown in Figure 5.18 (c) and (d). The simulation model also includes the curvatures in the vertical walls to provide a more accurate result. The gap is 80 nm wide at the bottom and 190 nm wide on the top. The strongest field points located at the bottom where the gap is narrowest. The field at the top near the gap is greatly degraded due to the curvature. The simulated phase also shows the π shift between the two regions above the gap. The experiment result qualitatively agrees with the simulation. The disappeared hot spots near the bottom of the gap in the measurement are likely because that the tip is unable to follow the vertical walls to the bottom.

To further understand the measurement results, the cross sections of the field at different heights in XZ plane are plotted in Figure 5.19 (a), along with the simulation result (Figure 5.19 (b)). In the plots, the FWHMs of the simulation profiles increase from 94 nm at 2 nm to 113 nm at 16 nm, in which a clear increasing trend is observed. While for the measured profiles, all the FWHMs are around 145 nm, in which the trend is obscured. This is also easy to tell from Figure 5.18 (a) and (c).

Besides the cross section in the horizontal direction, another plot in the vertical direction is shown in Figure 5.19 (c). The vertical plot is obtained by plotting a line through the peaks in the horizontal cross sections in (a) and (b). The experiment data only covers a range of up to 40 nm in Z direction. In the vertical direction plot, the trend of experiment data roughly matches the decay rate of the simulation result. In both of the curves, the peak decays to a half within a few tens of nanometers. This indicates that the measured signal comes from the region very close to the surface. Since the tip is oscillating at an

amplitude of about 40 nm, the effective height of the so-NSOM measurement should be near the lowest position within its oscillation cycle.
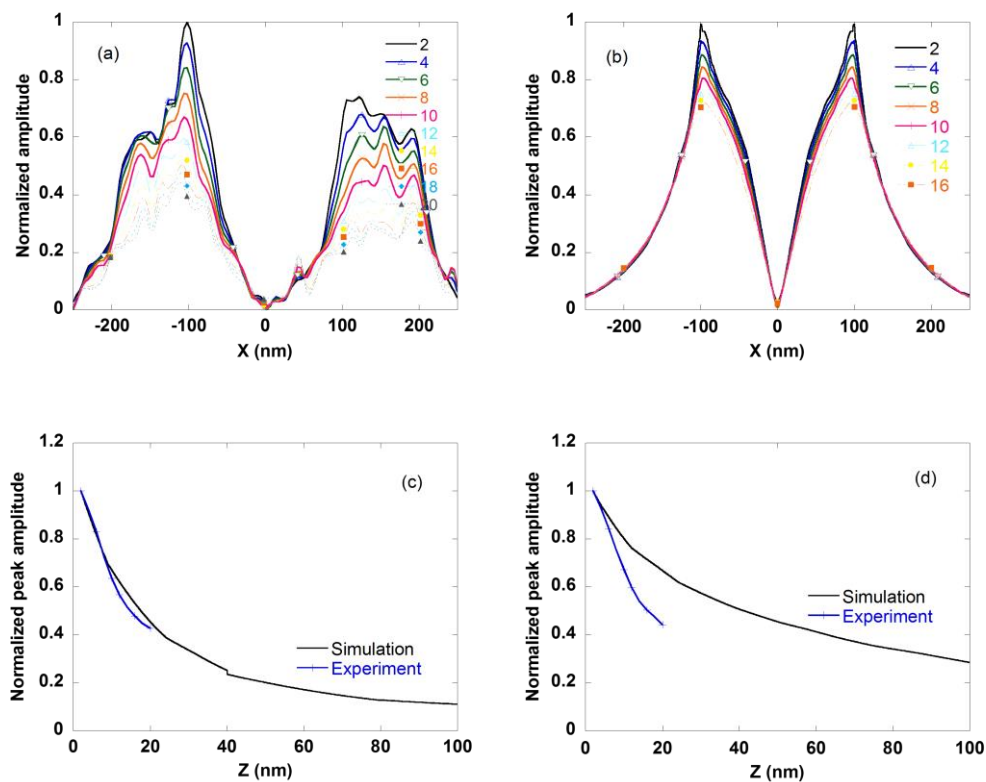
Figure 5.19. The cross sections of measured amplitude (a) and the simulate amplitude (b) in horizontal direction, and a cross section of amplitude in the vertical direction of the bowtie (c) and the grating (d).

Overall, the experiment results are in reasonable agreement with numerical simulations. In the lateral direction (XY plane), the experiment obtains slightly larger FWHMs than the simulation results. Because of the highly simplified conditions, such as no inclusion of the tip, no modulation process involved, surface curvatures are not exact, etc., the simulation result is not necessarily the exact field distribution,. However, the unsatisfied results could also come from a few experimental conditions. The scan step size in the lateral direction is 10 nm. Combining the 10 nm radius tip, it has already set a resolution

limit. As mentioned earlier, the order of harmonics used for demodulation also greatly impacts the suppression of background, which could help to resolve a smaller spot size. Lastly the curvature in the fabricated structure can lead to very different optical response than expected, which is confirmed by both the experiment and simulation. For the vertical Z direction, much higher resolution has been obtained. The field variation in less than 10 nm range has been obtained. The reason for achieving a resolution exceeding the limit of tip size is due to the strong dipole interaction between tip and sample in the vertical direction, which has also been reported in other works (Oshikane, et al., 2007). In the end, the three dimensional mapping provides a better understanding of the optical fields in the space near the structures. The mapping result also reveals useful information about the factors that affect the performance of the designed structure. Besides, it also shows the different resolution limits between the lateral and vertical directions, which could help to improve the understanding of the s-NSOM technique and explore potential applications.

CHAPTER 6. CONCLUSIONS AND FUTURE WORK

6.1   Summary and Conclusions

In this work, the near field optical measurement technique of NSOM has been studied. With the two home-built NSOM setups – aperture NSOM and scattering (apertureless) NSOM, the optical near fields of different plasmonic structures are investigated.

The NSOM technique has been applied to the investigation of the optical properties of nanostructures at a resolution below the diffraction limit. It utilizes the high spatial resolution of scanning probe microscopy (SPM) and the optical antenna property of a sharp tip, to characterize the nanoscale optical phenomena. The physics behind both the aperture NSOM and the scattering NSOM is explained. The implementation of both systems has been discussed, with a focus on the optical contrast mechanism and the suppression of the background noise, especially in the case of the scattering NSOM.

The bowtie ridge aperture is known for its ability of field confinement and enhancement. To understand the local field distribution near the aperture exit, a three-dimensional measurement of its near field distribution is conducted with both types of NSOM. The experiment results confirm the fast decay nature of optical near fields. It also proves the strong polarization dependence of the bowtie aperture. Besides a single aperture, concentric grating structures are also added to further increase the transmission efficiency

of bowtie aperture. The NSOM results demonstrate this enhancement and show an increase of 15 times in the near field transmitted energy.

To overcome the resolution limit and the low efficiency of aperture type NSOM, the alternative scattering NSOM is implemented. For scattering NSOM, the resolution is basically only limited by the radius of the tip apex. The main obstacle of s-NSOM, which is the overwhelming background noise, is tackled with interferometry detection method. In this work, the pseudo-heterodyne interferometry method is implemented. With the home-built s-NSOM setup, the optical responses of several different plasmonic structures have been studied. The examination of a sample with circular aperture arrays shows that the interferometric pseudo-heterodyne method is indeed effective in suppressing the background noise. The s-NSOM has also been used to investigate the interferometric pattern observed during the measurement of a single nanoslit. The formation mechanism of the observed fringe pattern has been studied. In the end, a revisit of the 3-D optical field distribution of the bowtie aperture has been performed, with a focus on the E_z field. For s-NSOM measurements, both the amplitude and phase information can be obtained, enabling vector analysis of different field components.

6.2 <u>Future Work</u>

The scattering type NSOM shows a great potential in optical imaging with very high spatial resolution. The tip sample coupling effect can be used to explore the physics behind many nanoscale phenomena. Based on what has been accomplished, the present work can be expanded in the following directions.

On the instrumental side, to better understand the origin of the signal, it is worthy to investigate the relation of the signals at different sidebands. This will also provide some guidance in the optical alignment of the s-NSOM system. It has been observed that the oscillation amplitude also has a strong influence on the obtained signal level. An investigation on this aspect will help in the understanding of the contrast mechanism. On the hardware, adding a real time processing module will greatly facilitate the whole operation and provide insight into the modulation process.

The s-NSOM has the potential for mapping the vector fields in the visible wavelengths. Some preliminary results have been obtained. The Pt-coated tip can have enough response from the lateral field, thus it can be used to map the in-plane field component. Another option is to design more efficient tip to detect both the in-plane and out-of-plane fields. It is also useful to characterize the tip response for different vector fields. This could also be challenging because any misalignment could lead to very different signal strength, thus affect the obtained tip response ratio.

Another future work is regarding the sample fabrication. As shown in the experimental results and numerical simulations, the corners and edge curvatures will greatly influence the performance of the designed structures. One easy solution is to use some more advanced fabrication tools, for example, replacing the Gallium ion beam with a Helium ion beam, which will push the fabrication resolution to below 10 nm. However, it is still a very expensive tool and not widely available yet. Another solution could be developing some novel fabrication procedures to reduce the influence of curvatures. One concept is to use a sacrificial layer to protect the demanded structure when using the Gallium ion beam. This has been tried for a few times, but there is still difficult to completely remove

the sacrificial layer. Another way to work around could be keeping the sacrificial layer, which requires the sacrificial material to be transparent (not affect the device performance) and at the bottom of the metallic film. Then the aperture can be milled from the bottom. In this way, the narrowest gap will be on the top of the surface, producing the strongest enhancement at the exit plane of fabricated structures for potential applications.

LIST OF REFERENCES

LIST OF REFERENCES

Aravind, P.K. and Metiu, H. (1983), "The effects of the interaction between resonances in the electromagnetic response of a sphere-plane structure; applications to surface enhanced spectroscopy", Surface Science, Vol. 124 No. 2–3, pp. 506–528.

Bethe, H.A. (1944), "Theory of diffraction by small holes", Physical Review, Vol. 66 No. 7-8, pp. 163–182.

Betzig, E., Trautman, J.K., Harris, T.D., Weiner, J.S. and Kostelak, R.L. (1991), "Breaking the diffraction barrier: optical microscopy on a nanometric scale", Science, Vol. 251 No. 5000, pp. 1468–1470.

Bohn, J.L., Nesbitt, D.J. and Gallagher, A. (2001), "Field enhancement in apertureless near-field scanning optical microscopy", Journal of the Optical Society of America A, Vol. 18 No. 12, pp. 2998–3006.

Bouhelier, A., Beversluis, M.R. and Novotny, L. (2003), "Near-field scattering of longitudinal fields", Applied Physics Letters, Vol. 82 No. 25, pp. 4596–4598.

Bouwkamp, C.J. (1950), "On Bethe's theory of diffraction by small holes", Philips Res. Rep, Vol. 5 No. 5, pp. 321–332.

Calander, N. and Willander, M. (2002), "Theory of surface-plasmon resonance optical-field enhancement at prolate spheroids", Journal of Applied Physics, Vol. 92 No. 9, pp. 4878–4884.

Campion, A. and Kambhampati, P. (1998), "Surface-enhanced Raman scattering", Chem. Soc. Rev., Vol. 27 No. 4, pp. 241–250.

Costa-Fernández, J.M., Depasse, F. and Girard, C. (1992), "Superresolution of near-field optical microscopy defined from properties of confined electromagnetic waves", Applied Optics, Vol. 31 No. 16, pp. 3036–3045.

Courjon, D., Sarayeddine, K. and Spajer, M. (1989), "Scanning tunneling optical microscopy", Optics Communications, Vol. 71 No. 1-2, pp. 23–28.

Cvitkovic, A., Ocelic, N. and Hillenbrand, R. (2007), "Analytical model for quantitative prediction of material contrasts in scattering-type near-field optical microscopy", Optics Express, Vol. 15 No. 14, pp. 8550–8565.

Ermushev, A.V., Mchedlishvili, B.V., Oleĭnikov, V.A. and Petukhov, A.V. (1993), "Surface enhancement of local optical fields and the lightning-rod effect", Quantum Electronics, Vol. 23 No. 5, pp. 435–440.

Esteban, R., Vogelgesang, R., Dorfmüller, J., Dmitriev, A., Rockstuhl, C., Etrich, C. and Kern, K. (2008), "Direct Near-Field Optical Imaging of Higher Order Plasmonic Resonances", Nano Letters, Vol. 8 No. 10, pp. 3155–3159.

Fei, Z., Rodin, A.S., Andreev, G.O., Bao, W., McLeod, A.S., Wagner, M., Zhang, L.M., et al. (2012), "Gate-tuning of graphene plasmons revealed by infrared nano-imaging", Nature, Vol. 487 No. 7405, pp. 82–85.

Fikri, R., Grosges, T. and Barchiesi, D. (2004), "Apertureless scanning near-field optical microscopy: numerical modeling of the lock-in detection", Optics Communications, Vol. 232 No. 1–6, pp. 15–23.

Fischer, U.C. and Pohl, D.W. (1989), "Observation of single-particle plasmons by near-field optical microscopy", Physical Review Letters, Vol. 62 No. 4, pp. 458–461.

Fleischmann, M., Hendra, P.J. and McQuillan, A.J. (1974), "Raman spectra of pyridine adsorbed at a silver electrode", Chemical Physics Letters, Vol. 26 No. 2, pp. 163–166.

Garcia-Vidal, F.J., Lezec, H.J., Ebbesen, T.W. and Martı´n-Moreno, L. (2003), "Multiple paths to enhance optical transmission through a single subwavelength slit", Physical Review Letters, Vol. 90 No. 21, p. 213901.

Gerton, J.M., Wade, L.A., Stanciu, G.A., Ma, Z. and Quake, S.R. (2004), "Tip-enhanced fluorescence microscopy at 10 nanometer resolution", Physical Review Letters, Vol. 93 No. 18, p. 180801.

Gucciardi, P.G., Bachelier, G., Stranick, S.J. and Allegrini, M. (2008), "Background-Free Apertureless Near-Field Optical Imaging", Applied Scanning Probe Methods VIII, pp. 1–29.

Guo, R., Kinzel, E.C., Li, Y., Uppuluri, S., Raman, A. and Xu, X. (2010), "Three-dimensional mapping of optical near field of a nanoscale bowtie antenna", Optics Express., Vol. 18, Issue 5, pp. 4961-4971.

Hillenbrand, R., Knoll, B. and Keilmann, F. (2001), "Pure optical contrast in scattering-type scanning near-field microscopy", Journal of Microscopy, Vol. 202 No. 1, pp. 77–83.

Ichimura, T., Hayazawa, N., Hashimoto, M., Inouye, Y. and Kawata, S. (2004), "Tip-Enhanced Coherent Anti-Stokes Raman Scattering for Vibrational Nanoimaging", Physical Review Letters, Vol. 92 No. 22.

Jackson, J.D. (1998), Classical Electrodynamics, Wiley, New York.

Jersch, J., Demming, F., Hildenhagen, L.J. and Dickmann, K. (1998), "Field enhancement of optical radiation in the nearfield of scanning probe microscope tips", Applied Physics A, Vol. 66 No. 1, pp. 29–34.

Jin, E.X. and Xu, X. (2006), "Enhanced optical near field from a bowtie aperture", Applied Physics Letters, Vol. 88 No. 15, p. 153110.

Karrai, K. and Grober, R.D. (1995), "Piezoelectric tip-sample distance control for near field optical microscopes", Applied Physics Letters, Vol. 66 No. 14, pp. 1842–1844.

Kinzel, E.C. (2010), Ridge aperture optical antennas, Ph. D. thesis, Purdue University.

Kinzel, E.C., Srisungsitthisunti, P., Li, Y., Raman, A. and Xu, X. (2010), "Extraordinary transmission from high-gain nanoaperture antennas", Applied Physics Letters, Vol. 96, p. 211116.

Knoll, B. and Keilmann, F. (2000), "Enhanced dielectric contrast in scattering-type scanning near-field optical microscopy", Optics Communications, Vol. 182 No. 4, pp. 321–328.

Krug II, J.T., Sánchez, E.J. and Xie, X.S. (2002), "Design of near-field optical probes with optimal field enhancement by finite difference time domain electromagnetic simulation", The Journal of Chemical Physics, Vol. 116, p. 10895.

Lalanne, P. and Hugonin, J.P. (2006), "Interaction between optical nano-objects at metallo-dielectric interfaces", Nature Physics, Vol. 2 No. 8, pp. 551–556.

Lalanne, P., Hugonin, J.P. and Rodier, J.C. (2006), "Approximate model for surface-plasmon generation at slit apertures", J. Opt. Soc. Am. A, Vol. 23 No. 7, pp. 1608–1615.

Lérondel, G., Kostcheev, S. and Plain, J. (2012), "Nanofabrication for Plasmonics", in Enoch, S. and Bonod, N. (Eds.),Plasmonics, Springer Series in Optical Sciences, Springer Berlin Heidelberg, pp. 269–316.

Lewis, A., Isaacson, M., Harootunian, A. and Muray, A. (1984), "Development of a 500 spatial resolution light microscope:: I. light is efficiently transmitted through [lambda]/16 diameter apertures", Ultramicroscopy, Vol. 13 No. 3, pp. 227–231.

Lezec, H.J., Degiron, A., Devaux, E., Linke, R.A., Martin-Moreno, L., Garcia-Vidal, F.J. and Ebbesen, T.W. (2002), "Beaming light from a subwavelength aperture", Science, Vol. 297 No. 5582, pp. 820–822.

Li, Y., Zhou, N., Kinzel, E.C., Ren, X. and Xu, X. (2014), "The origin of interferometric effect involving surface plasmon polariton in scattering near-field scanning optical microscopy", Optics Express, Vol. 22 No. 3, p. 2965.

Martin, Y.C., Hamann, H.F. and Wickramasinghe, H.K. (2001), "Strength of the electric field in apertureless near-field optical microscopy", Journal of Applied Physics, Vol. 89 No. 10, pp. 5774–5778.

Massey, G.A. (1984), "Microscopy and pattern generation with scanned evanescent waves", Applied Optics, Vol. 23 No. 5, pp. 658–660.

Max Born. (1999), Principles of optics: electromagnetic theory of propagation, interference and diffraction of light, Cambridge University Press, New York.

Novotny, L. (2007), "The history of near-field optics", Progress in Optics, Vol. 50, pp. 137–184.

Novotny, L. and Hecht, B. (2006), Principles of Nano-optics, Cambridge University Press, New York.

Ocelic, N. (2007), Quantitative near-field phonon-polariton spectroscopy, Ph. D. thesis, Technical University Munich.

Ocelic, N., Huber, A. and Hillenbrand, R. (2006), "Pseudoheterodyne detection for background-free near-field spectroscopy", Applied Physics Letters, Vol. 89, p. 101124.

Oesterschulze, E., Georgiev, G., Müller-Wiegand, M., Vollkopf, A. and Rudow, O. (2001), "Transmission line probe based on a bow-tie antenna", Journal of Microscopy, Vol. 202 No. 1, pp. 39–44.

Olmon, R.L., Rang, M., Krenz, P.M., Lail, B.A., Saraf, L.V., Boreman, G.D. and Raschke, M.B. (2010), "Determination of electric-field, magnetic-field, and electric-current distributions of infrared optical antennas: a near-field optical vector network analyzer", Physical Review Letters, Vol. 105 No. 16, p. 167403.

Oshikane, Y., Kataoka, T., Okuda, M., Hara, S., Inoue, H. and Nakano, M. (2007), "Observation of nanostructure by scanning near-field optical microscope with small sphere probe", Science and Technology of Advanced Materials, Vol. 8 No. 3, pp. 181–185.

Otto, A. (1968), "A new method for exciting non-radioactive surface plasma oscillations", Phys. Stat. Sol, Vol. 26, pp. K99–K101.

Pedrotti, F.L. and Pedrotti, L.S. (1987), Introduction to Optics, Prentice Hall, New Jersey.

Pohl, D.W., Denk, W. and Lanz, M. (1984), "Optical stethoscopy: Image recording with resolution λ/20", Applied Physics Letters, Vol. 44 No. 7, pp. 651–653.

Rang, M., Jones, A.C., Zhou, F., Li, Z.Y., Wiley, B.J., Xia, Y. and Raschke, M.B. (2008), "Optical near-field mapping of plasmonic nanoprisms", Nano Letters, Vol. 8 No. 10, pp. 3357–3363.

Roberts, A. (1987), "Electromagnetic theory of diffraction by a circular aperture in a thick, perfectly conducting screen", Journal of the Optical Society of America A, Vol. 4 No. 10, pp. 1970–1983.

Roxworthy, B.J., Ko, K.D., Kumar, A., Fung, K.H., Chow, E.K.C., Liu, G.L., Fang, N.X., et al. (2012), "Application of Plasmonic Bowtie Nanoantenna Arrays for Optical Trapping, Stacking, and Sorting", Nano Letters, Vol. 12 No. 2, pp. 796–801.

Schnell, M., García-Etxarri, A., Huber, A.J., Crozier, K., Aizpurua, J. and Hillenbrand, R. (2009), "Controlling the near-field oscillations of loaded plasmonic nanoantennas", Nature Photonics, Vol. 3 No. 5, pp. 287–291.

Schnell, M., Garcia-Etxarri, A., Huber, A.J., Crozier, K.B., Borisov, A., Aizpurua, J. and Hillenbrand, R. (2010), "Amplitude- and Phase-Resolved Near-Field Mapping of Infrared Antenna Modes by Transmission-Mode Scattering-Type Near-Field Microscopy", The Journal of Physical Chemistry C, Vol. 114 No. 16, pp. 7341–7345.

Sendur, K. and Challener, W. (2003), "Near-field radiation of bow-tie antennas and apertures at optical frequencies", Journal of Microscopy, Vol. 210 No. 3, pp. 279–283.

Synge, E.H. (1928), "A suggested method for extending microscopic resolution into the ultra-microscopic region", Philosophical Magazine, Vol. 6 No. 35, pp. 356–362.

Taubner, T., Hillenbrand, R. and Keilmann, F. (2003), "Performance of visible and mid-infrared scattering-type near-field optical microscopes", Journal of Microscopy, Vol. 210 No. 3, pp. 311–314.

Uppuluri, S., Kinzel, E.C., Li, Y. and Xu, X. (2010), "Parallel optical nanolithography using nanoscale bowtie aperture array", Optics Express, Vol. 18, No. 7, pp. 7369-7375.

Wang, B., Aigouy, L., Abbe, E., Gierak, J., Hugonin, J.-P. and Lalanne, P. (2009), "Efficient generation of surface plasmon by single-nanoslit illumination under highly oblique incidence", Applied Physics Letters, Vol. 94 No. 1, pp. 011114–011114.

Wang, L. (2008), Nanolithography using nanoscale ridge apertures, Ph. D. thesis, Purdue University.

Wang, L. and Xu, X. (2007), "Spectral resonance of nanoscale bowtie apertures in visible wavelength", Applied Physics A, Vol. 89 No. 2, pp. 293–297.

William L. Barnes, Alain Dereux and Thomas W. Ebbesen. (2003), "Surface plasmon subwavelength optics", Nature, Vol. 424 No. 6950, pp. 824–830.

Wokaun, A. (1985), "Surface enhancement of optical fields", Molecular Physics, Vol. 56 No. 1, pp. 1–33.

Wurtz, G., Bachelot, R. and Royer, P. (1998), "A reflection-mode apertureless scanning near-field optical microscope developed from a commercial scanning probe microscope", Review of Scientific Instruments, Vol. 69 No. 4, pp. 1735–1743.

Yu, N., Cubukcu, E., Diehl, L., Bour, D., Corzine, S., Zhu, J., Höfler, G., et al. (2007), "Bowtie plasmonic quantum cascade laser antenna", Optics Express, Vol. 15 No. 20, pp. 13272–13281.

Zenhausern, F., Oboyle, M.P. and Wickramasinghe, H.K. (1994), "Apertureless near-field optical microscope", Applied Physics Letters, Vol. 65 No. 13, pp. 1623–1625.

Zhang, L., Kubo, A., Wang, L., Petek, H. and Seideman, T. (2011), "Imaging of surface plasmon polariton fields excited at a nanometer-scale slit", Physical Review B, Vol. 84 No. 24, p. 245442.

Zhou, N., Li, Y. and Xu, X. (2014), "Resolving near-field from high order signals of scattering near-field scanning optical microscopy", Optics Express, Vol. 22 No. 15, pp. 18715–18723.

VITA

VITA

Yan Li

Education
B. S., Mechanical Engineering, 2008, University of Science and Technology of China, Hefei, Anhui, China
Ph. D., Mechanical Engineering, 2014, Purdue University, West Lafayette, IN, USA

Research Interests
Characteristics of optical near fields
Plasmonic structures and their properties
High resolution imaging techniques

Publications
Li, Y., Zhou, N., Kinzel, and Xu, X., 2014, "Three Dimensional Mapping of Optical Near Field with Scattering Type NSOM", (In preparation).

Li, Y., Zhou, N., Kinzel, E. C., Ren, X, and Xu, X., 2014, "The origin of interferometric effect involving surface plasmon polariton in scattering near-field scanning optical microscopy", Optics Express, Vol. 21, Issue 3, pp. 2965-2972.

Zhou N., Li, Y., Xu, X., 2014, "Resolving near-field from high order signals of scattering near-field scanning optical microscopy", Optics Express, Vol. 22, Issue 15, pp. 18715-18723.

Ozcelikkale A., Li Y., Xu X., and Han B., 2013, "Effects of Freezing on Collagen Nanoscale Structure in Engineered Tissues", Proceedings of the 2013 ASME Global Congress on Nano Engineering for Medicine and Biology, Boston, MA, USA.

Uppuluri, S.M.V., Kinzel, E.C., Li, Y., and Xu, X, 2010, " Parallel optical nanolithography using nanoscale bowtie aperture array", Optics Express, Vol. 18, Issue 7, pp. 7369-7375.

Guo, R., Kinzel, E.C., Li, Y., Uppuluri, S.M.V., Raman, A., and Xu, X., 2010, " Three-dimensional mapping of optical near field of a nanoscale bowtie antenna", Optics Express., Vol. 18, Issue 5, pp. 4961-4971.

Kinzel, E.C., Srisungsitthisunti, P., Li, Y. and Xu, X, 2010, " Extraordinary transmission from high-gain nanoaperture antennas", Appl. Phys. Lett., Vol. 96, p. 211116.

Jiang W., Zhong X., Chen K., Li Y., 2009, "GA optimized SVM based mechanical equipment fault detection model", Computer Applications and Software, Vol. 26, Issue 1.